UNIVERSIDAD NACIONAL AUTÓNOMA DE MÉXICO
POSGRADO EN CIENCIAS FÍSICAS
INSTITUTO DE CIENCIAS NUCLEARES

CHARGED PION, KAON AND PROTON PRODUCTION IN PP COLLISIONS AT LHC ENERGIES MEASURED WITH ALICE

TESIS
QUE PARA OPTAR POR EL GRADO DE:
MAESTRO EN CIENCIAS FÍSICAS (FÍSICA)

PRESENTA:

RAÚL TONATIUH JIMÉNEZ BUSTAMANTE

TUTOR PRINCIPAL:
DR. GUY PAIC
INSTITUTO DE CIENCIAS NUCLEARES

MIEMBROS DEL COMITÉ TUTOR:
DR. ARTURO MENCHACA ROCHA
INSTITUTO DE FÍSICA
DR. ELEAZAR CUAUTLE FLORES
INSTITUTO DE CIENCIAS NUCLEARES

MÉXICO, D. F. ABRIL 2014

A Luz María, Raúl y a mi abuela

que les debo todo

“One does not discover new lands without consenting to lose sight of the shore for a very long time" André Gide

“Thou shalt say what thou doest, and thou shalt be able to justify it out of thine own mouth: not the mouth of thy supervisor, nor thy colleague who did the analysis last time, nor thy local statistics guru, nor thy mate down the pub” R. Barlow.

Agradecimientos

Agradezco primeramente a mi tutor Guy Paic, por la oportunidad brindada, por aceptar invertir tiempo y esfuerzo en mi formación como científico y como persona. Gracias por compartir su sabiduría y permitirme ir a CERN tantas veces, ha sido un gran honor trabajar a su lado.

Gracias a mis padres, espero que estén orgullosos de este trabajo, ya que todo es fruto de su apoyo y cariño inconmensurable. Gracias a mi abuela, a mis hermanos Ehecatl y Tlacaelel, por su apoyo, confianza y compañía.

En reconocimiento a Perla Valero. Por tu tiempo, tu cariño sincero, tu apoyo incondicional y tus consejos.

Agradezco a los miembros de mi comité tutor: Eleazar Cuautle y Arturo Menchaca Rocha por haber dedicado tiempo para la corrección y mejora de este trabajo. También agradezco a mis sinodales: Alejandro Ayala, Ernesto Belmont, Gerardo Herrera y Andrés Sandoval por haber leído cuidadosamente mi tesis, todas sus sugerencias ayudaron a mejorar la calidad de mi trabajo.

Un agradecimiento muy especial a Alejandro Ayala y a Miguel Alcubierre por el apoyo para realizar mis estancias en CERN, el aprendizaje y la experiencia que obtuve de éstas fue de gran importancia para esta tesis.

Muchas gracias a todos mis colegas de ALICE en el ICN: Luciano Díaz, Ivonne Maldonado y Enrique Patiño. Especialmente Daniel Mayani, Antonio Ortiz, y Edgar Pérez, con quienes compartí grandes momentos en CERN. Gracias a Daniel por su paciencia al explicar, a Antonio por siempre tener buenas sugerencias, una parte de este trabajo se debe a sus buenas ideas. Gracias a Edgar por compartir el arduo camino del análisis de datos en ALICE y de estudiante de maestría en el ICN.

Many thanks to Barbara Guerzoni for answer all my questions related to the Time Of Flight analysis. Thanks to my friend Alexander Kalweit for his clear answers and his very good explanations.

Gracias a mis amigos Físicos: Ricardo Ancheyta, Miguel Ángel Lopez, Edgar Pérez, Iván Toledano y Martín Zumaya, todos seguimos forjando nuestro camino en la ciencia.

Agradezco también mis tíos.

A mis amigos de toda la vida: Jorge, Rodolfo y Cinthya. Gracias por todos los momentos que hemos compartido, por su amistad y sus palabras sinceras.

Resumen

0.1 Introducción

El Modelo Estándar es el encargado de describir la composición de la materia y las fuerzas fundamentales. Este modelo incluye la interacción fuerte, débil y electromagnética dejando fuera a la gravedad. Las partículas que forman la materia son llamadas fermiones (partículas con espín semientero) y las partículas mediadoras de las interacciones son llamadas bosones (partículas con espín entero). Los fermiones se dividen en tres familias, cada una de las familias cuenta con dos leptones y dos quarks. Los leptones se caracterizan por ser afectados por la interacción débil, siendo los leptones cargados afectados también por la interacción electromagnética. Los quarks además de la carga electromagnética poseen una carga llamada carga de color por la cual interactúan fuertemente. En la naturaleza no se observan quarks libres, sino que aparecen en la forma de hadrones. Los hadrones se encuentran agrupados en *bariones* y *mesones*. Los bariones son partículas compuestas por tres quarks mientras que los mesones solamente están compuestos por un par de quark-antiquark.

Las interacciones fundamentales se producen a través del intercambio de bosones de norma. La interacción fuerte es mediada por los gluones (g) y la teoría encargada de su estudio es la Cromodinámica Cuántica (QCD). La interacción electromagnética es mediada por los fotones (γ) descrita por la Electrodinámica Cuántica (QED). La interacción débil es mediada por el intercambio de bosones W^+, W^- y Z^0 y es descrita por la *teoría electrodébil* la cual incorpora la interacción electromagnética.

Un punto importante en el modelo es que se debe añadir un bosón, conocido como el *bosón de Higgs*. El mecanismo de Higgs genera las masas para los bosones W y Z mientras que permanece sin masa para el γ. El descubrimiento del bosón de Higgs fue anunciado el 4 de julio del 2012 por los experimentos CMS y ATLAS en el Centro Europeo para la Investigación Nuclear (CERN), en Ginebra Suiza.

El Gran Colisionador de Hadrones (LHC) en CERN ha ayudado a obtener grandes resultados desde las primeras colisiones en 2009 hasta febrero del año pasado en el que entro en una etapa de mantenimiento y renovación (LS1)[1], la cual servirá para renovar y mejorar ciertos aspectos tanto del colisionador como de los experimentos inmiscuidos en estas pesquisas. El LS1 permitirá alcanzar la energía de operación para la cual fue diseñada

[1]Long Shutdown 1.

el acelerador, esto es 14 TeV en el centro de masa para colisiones protón-protón.

El experimento ALICE es uno de los cuatro detectores principales del LHC, el cual esta enfocado en el estudio del plasma de quarks y gluones formado en colisiones de iones pesados; sin embargo también se dedica al estudio de colisiones protón-protón ya que éstas, sirven como punto de partida para entender las colisiones de iones pesados. Una de las ventajas de ALICE sobre otros experimentos como ATLAS y CMS, es la identificación de partículas.

El objetivo de esta tesis es la medición del espectro de momento transverso p_{T} de piones, kaones y protones utilizando uno de los detectores encargados de la identificación de partículas en ALICE. Los resultados presentados en este trabajo se han realizado con el análisis de datos del detector de tiempo de vuelo (TOF) [2] en colisiones protón - protón a diferentes energías en el centro de masa ($\sqrt{s}$) a las que ha funcionado el LHC: 0.9, 2.76 y 7.0 TeV.

0.2 Identificación de Partículas en ALICE

ALICE emplea diferentes métodos de identificación de partículas, con diferentes detectores que realizan la identificación en diferentes regiones de momento transverso (p_{T}). El Sistema de Rastreo Interno (ITS) y la Cámara de Proyección Temporal (TPC) miden la pérdida de energía específica de las partículas (dE/dx), lo que proporciona la identificación de partículas traza por traza en el intervalo de p_{T} (0.1 $\approx$ 1.0 GeV/c). El detector de Tiempo de Vuelo (TOF) contribuye a la identificación de partículas en intervalo entre p_{T} (0.5 $\approx$ 3.0 GeV/c), mientras que que el detector de anillos Cherenkov (HMPID) permite extender la identificación de protones hasta $p_{\mathrm{T}} \approx$ 6.0 GeV/c. Las partículas de muy alto p_{T} , hasta 20 GeV/c son identificadas con un método puramente estadístico usando la subida relativista de la pérdida de energía específica en la TPC.

0.2.1 El detector de tiempo de vuelo

El detector de tiempo de vuelo, TOF, cubre la región central de pseudo-rapidez | η |<0.9 y tiene un papel fundamental en la identificación de piones, kaones y protones, en la región intermedia de momento, más específicamente en el intervalo de momento alrededor de 0.5 GeV/c (que es el límite superior para las mediciones de pérdida de energía en los detectores TPC e ITS para kaones y piones) hasta 2.5 GeV/c. El TOF se encuentra en una capa cilíndrica con un radio interno de 3.7 m y un radio externo de 4 m; la longitud del barril es de aproximadamente 7.45 m, cubre ángulos polares entre 45 y 135 grados y un ángulo azimutal de 2π.

Tiene una estructura modular con 18 sectores en ϕ, cada uno de estos sectores se divide en 5 módulos a lo largo de la dirección del haz. Los módulos contienen un total de 1638 elementos detectores conocidos como tiras de cámaras de multiplacas resistivas

[2] Siglas en inglés de Time Of Flight.

(MRPC) cubriendo un área de 160 m^2. El aspecto importante de estas cámaras es que el campo eléctrico es grande y uniforme sobre todo el volumen sensible de gas del detector. Cualquier ionización producida por una partícula cargada al atravesar el detector comenzará procesos de avalanchas los cuales eventualmente generarán señales observadas en los electrodos.

Las MRPC son una pila formada por placas resistivas y su funcionamiento es el siguiente: Una alta diferencia de potencial es aplicada a las superficies externas del conjunto de placas, cuando una partícula atraviesa, ésta ioniza el gas y el gran campo eléctrico amplifica esta ionización mediante una avalancha de electrones. Las placas resistivas detienen el crecimiento de la avalancha en cada espacio, sin embargo son transparentes a la rápida señal inducida en los electrodos por el movimiento de los electrones. El total de la señal es la suma de las señales de todos los espacios. La razón por la que hay muchos espacios es para lograr mayor eficiencia, además al espacio entre las placas se aumenta la resolución del tiempo lo cual ayuda a una buena identificación de partículas.

0.2.2 Método

El método de identificación de partículas con el TOF está basado en su función de respuesta: la medición del tiempo de vuelo (Δt) de una partícula producida en el vértice que viaja por los detectores intermedios hasta alcanzar la superficie del TOF, situado a 3.7 m del vértice de ALICE. Se utiliza un método estadístico para la identificación de partículas, ajustando el Δt_i para cada especie [3] con funciones empíricas, como función del momento transverso (p_{T}). La producción de partículas extraída de los datos y se realiza contando el número de partículas en cada bin. Este método es conocido como *despliegue* y es utilizado ya que permita extender la identificación de partículas a mas alto momento transverso.

Las partículas reconstruidas por los detectores son solo una parte del número total de partículas producidas en la colisión, esto es debido a la imposibilidad de reconstruir todas las partículas por propiedades del detector como la aceptancia, zonas muertas del detector, canales ruidosos, etc. La fracción de partículas que puede reconstruir nuestro detector con respecto al número total de partículas generadas, es denominada *eficiencia* y se puede evaluar para nuestros detectores, usando generadores de eventos como PYTHIA. La eficiencia se obtiene generando eventos con PYTHIA [4] y aplicar el mismo método de reconstrucción que el utilizado en los datos, la eficiencia es la razón de partículas reconstruidas con respecto al número de partículas generadas. Las correcciones aplicadas son llamadas eficiencias y dependen del tipo de partícula y del p_{T} .

El espectro reportado en este análisis es exclusivamente para partículas primarias, esto permite la comparación entre los datos experimentales, los generadores de eventos y los cálculos teóricos. La definición precisa de partículas primarias y secundarias utilizada, es la misma adoptada por ALICE y se enuncia a continuación:

[3] i representa piones, kaones y protones

[4] En PYTHIA se conoce el número de partículas producidas durante la colisión.

- ✧ Las **partículas primarias** son las partículas producidas en la colisión incluyendo las partículas producto de decaimientos, exceptuando las partículas provenientes de decaimientos débiles o muones.
- ✧ Una **partícula secundaria de decaimiento débil** es una partícula hija de un decaimiento débil de un hadron ligero o de un muón.
- ✧ Las **partículas secundarias del material** son todas aquellas partículas que no pertenecen a ninguna de las dos categorías anteriores.

Debido a que los generadores de eventos subestiman la contaminación de decaimientos débiles y la interacción de partículas de baja energía con el material del detector no es muy bien reproducida por éstos, la contaminación de partículas secundarias se debe extraer directamente de los datos. Esto se realiza con la clase *TFractionFitter* de ROOT. Ésta clase utiliza las predicciones para la contaminación de partículas secundarias de los generadores de eventos (utilizados como plantillas), para estimar la contribución de estas fracciones en los datos. Estas correcciones se aplican solo a piones positivos y negativos, protones y antiprotones. Para los kaones la contaminación de secundarias es despreciable.

0.3 Resultados

Los resultados de esta tesis se dividen en dos partes, la primera consiste en el método la obtención del espectro de piones, kaones y protones en colisiones pp a $\sqrt{s}$ = 0.9, 2.76 TeV y 7.0 TeV. La segunda parte consiste en un análisis basado en el generador de eventos PYTHIA 8. Utilizamos como herramienta la esfericidad transversa (S_{T}), previamente medida en ALICE [34], para clasificar los eventos de acuerdo a su estructura y estudiar la producción de piones, kaones y protones en estos diferentes tipos de eventos.

0.3.1 Identificación de partículas

Obtuve el espectro de p_{T} para piones, kaones y protones a 3 energías diferentes en el intervalo de $0.5 \leq p_{\mathrm{T}} \leq 2.5$ GeV/*c* con el el TOF. Los espectros finales se muestran en las Fig. 4.18, Fig. 5.6 y Fig. 5.6. Las razones p/π y K/π se muestran en las Fig. 5.13 donde es posible observar que dentro de los errores sistemáticos no hay dependencia en la energía en la producción de piones, kaones y protones. Además se combinaron los espectros a energía de 2.76 TeV con otros detectores para ampliar el intervalo de p_{T} de la medición. Combinando éste resultado con los espectros de piones, kaones y protones obtenidos previamente por la colaboración ALICE en [18] se calculó el factor de modificación nuclear ($\mathrm{R_{AA}}$), mostrado en la Fig. 4.23. El factor de modificación nuclear esta definido en la ec. 4.8, y es la razón del espectro de p_{T} medido en colisiones pp y el espectro de p_{T} medido en colisiones Pb-Pb, normalizado al número de colisiones binarias N_{coll}.

0.3.2 Análisis de esfericidad para partículas identificadas

El estudio de esfericidad se llevo a cabo con la misma muestra de datos, con aproximadamente 60 millones de eventos. Primeramente, se clasifican los eventos de acuerdo a su esfericidad y se dividen en 5 diferentes intervalos, en cada uno de ellos se emplea el método de identificación de partículas con el TOF explicado anteriormente en el intervalo $0.5 \leq p_{\mathrm{T}} \leq 2.5$ GeV/c para piones y protones, y en el intervalo $0.5 \leq p_{\mathrm{T}} \leq 2.0$ GeV/c para kaones. El intervalo de p_{T} de la identificación de kaones se ve reducido respecto a la muestra MB debido a que la estadística disminuye considerablemente al dividir en 5 diferentes regiones de esfericidad.

Además se realizó un analisis similar con el generador de eventos PYTHIA 8.180, esto permite comparar con los datos y extender el intervalo de p_{T} hasta 10 GeV/c. Se simularon 160 millones de colisiones MB pp a $\sqrt{s}$ = 7 TeV y se aplican los mismos cortes a nivel de eventos que los datos y a nivel de trazas se utiliza la misma ventana de rapidez (y). Primero se realiza un estudio de la producción de piones, kaones y protones en función de multiplicidad. Posteriormente, se utiliza la esfericidad para clasificar el tipo de eventos de las colisiones, permite aislar eventos con estructuras y física diferente: los eventos de alta esfericidad ($0.8 \leq S_{\mathrm{T}} \leq 1.0$) en los que encontramos una distribución isotópica de partículas y eventos con baja esfericidad $0.0 \leq S_{\mathrm{T}} \leq 0.2$ en los que encontramos jets que contienen partículas de alto momento. El efecto de la reconexión de color en los eventos con jets y eventos isotópicos también se estudia y se muestra la diferencia mediante las razones p/π. Un estudio final combina la multiplicidad y la esfericidad para mostrar que lo sensible que es la razón p/π a estas variables.

0.4 Conclusiones

El espectro de momento transverso de π^+, π^-, K^+, K^-, p y $\overline{\mathrm{p}}$ a rapidez central $\mid y \mid < 0.5$ medida con el TOF en colisiones pp a 3 diferentes energías $\sqrt{s}$ = 0.9, 2.76 y 7.0 TeV se reporta como el principal resultado de mi trabajo. Con los espectros de momento es posible calcular las razones de partículas p/π y K/π. He mostrado que ambas son independientes de la energía dentro de las incertidumbres. Las razones proveen información de utilidad en el intervalo intermedio (entre 2.0-3.0 GeV/c) de momento transverso, donde se encuentra un aumento en la razón p/π tanto en colisiones pp como en colisiones Pb$-$Pb. Esta medición provee restricciones a los modelos teóricos introducidos en los generadores Monte Carlo, los cuales fallan en la descripción de los datos. La mayor diferencia entre los datos y los generados es en la razón K/π, esto es debido a la baja producción de extrañeza presente en los generadores con respecto a los datos a energías del LHC.

La comparación de los resultados obtenidos con TOF se encuentran de acuerdo con los resultados obtenidos previamente por ALICE. El análisis a $\sqrt{s}$ = 2.76 TeV reportado aquí es parte de los resultados preliminares de ALICE. Lo importante del análisis a ésta energía, es que al combinarlo con los resultados de Pb-Pb se calcula el factor de modificación nuclear(R_{AA}). El R_{AA} en el intervalo de p_{T} menor a 3 GeV/c muestra diferencia en la supresión entre las diferentes especies de partículas, siendo las partículas más pesadas

menos suprimidas El resultado del análisis a $\sqrt{s}$ = 0.9 TeV, muestra una mejoría respecto a los resultados previamente publicados por ALICE, publicado con una estadística considerablemente menor.

El análisis de esfericidad muestra que uno debe ser cauteloso al analizar los resultado MB ya que éstos son una superposición de eventos en los que intervienen diferentes procesos. Aquí he mostrado que la producción de hadrones es diferente para eventos isotrópicos (alta esfericidad) y para eventos con jets (baja esfericidad), tanto en los datos como en PYTHIA 8.180 para colisiones pp a $\sqrt{s}$ = 7.0 TeV. La razón p/π se ve afectada en ambos casos respecto a los resultados obtenidos sin cortar en esfericidad; la razón p/π aumenta alrededor de 5% respecto al valor sin corte para eventos isotópicos mientras que aumenta 10% para eventos con jets. Además con PYTHIA se observa que el mecanismo de *reconexión de color* no tiene un rol muy importante para los eventos en los con jets.

Summary

The ALICE detector has excellent Particle Identification (PID) capabilities in the central barrel ($|\eta| < 0.9$). This allows hadron production to be measured over a wide transverse momentum (p_{T}) range, based on different detectors and techniques. The particles are identified via the specific energy loss ($\mathrm{dE/dx}$), the time of flight, the Cherenkov angle. This thesis focus in the PID using the Time Of Flight detector. The PID method for pions, kaons and protons in pp collisions is explained and the pions, kaons and protons spectra at $\sqrt{s}$ = 0.9, 2.76 and 7.0 TeV are shown in the p_{T} range (0.5 GeV/c - 2.5 GeV/c).

Event shapes provide information about the properties of hadronic final states from particle collisions. In particular, this work focus on the event shape: transverse sphericity (S_{T}). The limits values of the variable are related to very specific configuration of events. The goal of this analysis is to show an interplay between the S_{T} and the pion, kaon and proton production. The results on real data show that the p/π ratio decreases (at $p_{\mathrm{T}} \approx$ 2.0 GeV/c) in jetty events respect to MB value, while p/π ratio rises (at $p_{\mathrm{T}} \approx 2.0$ GeV/c) for isotropic events respect to MB value. Similar result was obtained using PYTHIA 8.180.

This thesis is presented in the following way: Chapter 1 contains a brief description of the Standard Model, and some magus properties of p-p collisions. Chapter 2 describes the ALICE detector, its sub-detectors and the reconstruction method. In Chapter 3 the different Particle Identification methods used in ALICE are described. In Chapter 4 all the steps to perform the particle identification via the Time Of Flight detector are described. Comparisons with other detectors results are shown and then combined to obtain one combined spectra. The combined spectra for pp collisions at $\sqrt{s}$ = 2.76 TeV and the R_{AA} for different centralities are shown. The results for other energies are presented in Chapter 5. Chapter 6 shows the measurement done in different sphericity bins using the event generate PYTHIA 8. Chapter 7 contains the conclusions.

Index

1

Theoretical framework

1.1 Standard Model

The Standard Model describes the composition of the matter and the fundamental interactions as the electromagnetic, strong and weak forces. The gravity is not part of this model and the efforts to include it into this framework have proved to be a difficult challenge. The Standard Model classifies the elementary particles in fermions [1] and bosons [2], these are listed in Fig. 1.1.

The fermions are the basic constituents of matter; they are classified in 3 families of leptons: (ν_e, e), (ν_μ, μ) and (ν_τ, τ) , and in 3 families of quarks: up (u) and down (d) the first family, charm (c) and strange (s) the second family, and top (t) and bottom (b). The three families are repetitions of the same pattern with only differences in the masses with unknown physical significance.

The bosons are the mediators of the fundamental interactions; For the electromagnetic interaction, the force carrier is the the photon (γ), for the weak interaction there are 3 different force carriers, namely W^+, W^-, and Z^0, for the strong interaction the force carriers are 8 gluons. The Higgs boson (H) is the responsible of providing mass to the particles and was discovered on 4 July 2012 at CERN by ATLAS and CMS collaborations. This discovery marks the dawn of the new era in particle physics.

[1] The fermions are particles with fractional spin
[2] The bosons are particle with integer spin

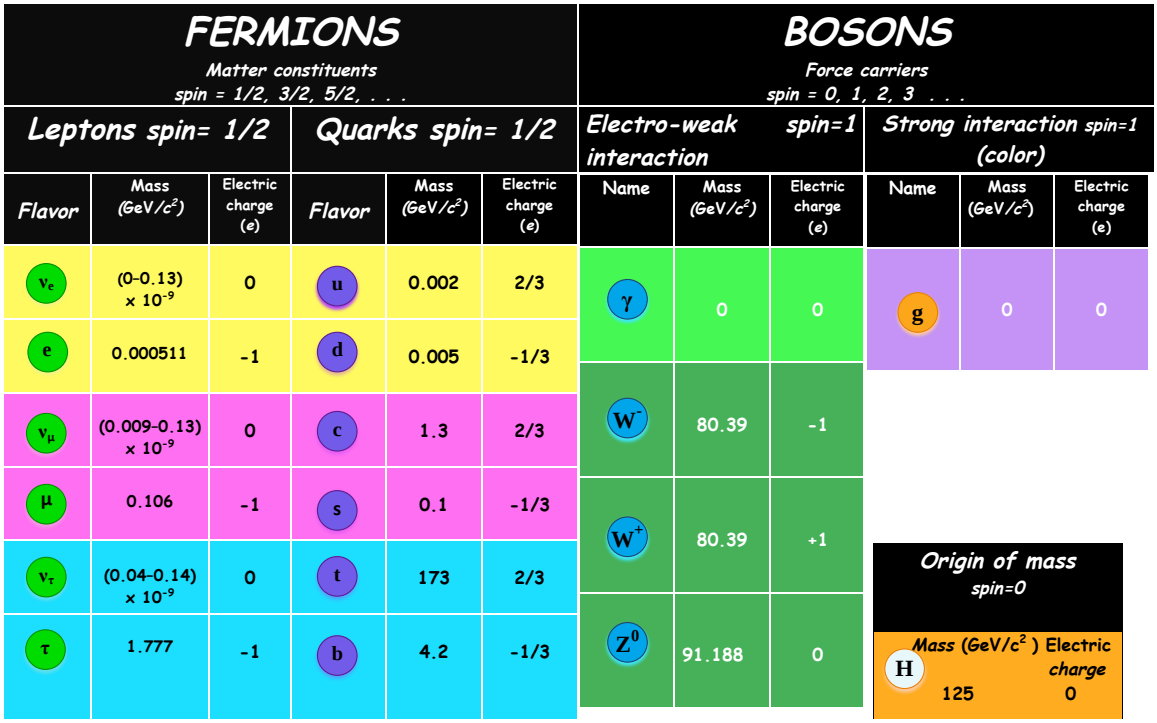

Fig. 1.1: Matter constituents and gauge bosons in the Standard Model.

1.2 Quantum Chromodynamics

Quantum Chromodynamics is the part of the Standard Model which describes the strong interaction. The quarks are fundamental objects that participates in strong interactions. Until now, free quarks have never been observed in the laboratory. This is a consequences of the dynamics of the strong interaction commonly referred as *quark confinement*. Because of the confinement their masses can not be measured, however, its mass has a value obtained from the Lagrangian of the theory. The quarks participate in strong interaction due to the *color charge*.

The first experimental hint for color existence was the discovery of the particle Δ^{++} in 1951 [1]. Since the Δ^{++} [3] is a fermion composed by 3 quarks u of the same spin and with symmetric spacial wave function. This required and additional quantum number in order to obey Pauli's principle. This was not understood till 1965 with the introduction of a new quantum number associated with the group SU(3): *the color*.

The color charge exist in 3 colors: red, blue and green, with their respective anti colors.

[3] Δ^{++} has an unusual electric charge +2, and its main decay channel is: $\Delta^{++} \rightarrow p + \pi^{+}$. The measurement "suggested a resonance peak .. interpreted to be an indication of the existence of an excited nucleon isobaric state" with total angular momentum J=$3/2$ [1]

The sum of the color charge in an hadron should be white, so that we can refer to the quark confinement as color confinement.

1.2.1 Baryons and mesons

The hadrons are particles formed by the more elementary strongly interacting particles: quarks and gluons. The hadrons can be classified due to their quark composition in two types: baryons and mesons. The **baryons** are colorless quark states composed by three quarks while the **mesons** are colorless quark-antiquark pairs. I will briefly discuss [4] some examples of mesons and baryons since this will be useful for the understanding of the results that will be presented in this work.

- **Neutral pions** π^0 ($\frac{u\bar{u}+d\bar{d}}{\sqrt{2}}$) (m = 134.97 MeV/$c^2$)

  Neutral pions can be formed with two combinations ($u\bar{u}$) and ($d\bar{d}$) with identical quantum numbers. Its lifetime is $c\tau$=7.8045 m. The π^0 main decays channels are:

$$\pi^0 \rightarrow 2\gamma, 98.823\%$$
$$\pi^0 \rightarrow \gamma e^+ + e^-, 1.174\%$$

- **Charged pions** π^+ **(**$u\bar{d}$**) and** π^- **(**$d\bar{u}$**)** (m = 139.57 MeV/c^2)

  Charged pions are observed directly in charged-particle-tracking detectors since their mass differ significantly from the heavier $K^{\pm}$ and p/$\bar{p}$. The $\pi^{\pm}$ has a $c\tau$=7.8045 m and the main decay channel is:

$$\pi^+ \rightarrow \mu^+ + \nu_\mu, 99.987\%$$

- **Neutral kaons** K^0_S **and** K^0_L **(**$s\bar{d}$**) and (**$d\bar{s}$**)** (m = 497.7 MeV/c^2)

  These are both ortoghonal combinations of the two neutral states. The S and the L are due to their lifetime. The short live kaon K^0_S has a $c\tau$=2.676 cm while the long live kaon K^0_L has $c\tau$=1551 cm.

- **Charged kaons** K^+ **(**$u\bar{s}$**) and** K^- **(**$s\bar{u}$**)** (m = 493.68 MeV/c^2)

  Charged kaons are also observed directly in charged-particle-tracking detectors. The $K^{\pm}$ has a $c\tau$=3.71m and the main decays channels are:

$$K^+ \rightarrow \mu^+ + \nu_\mu, 63.55\%$$
$$K^+ \rightarrow \pi^+ + \pi^0, 20.66\%$$
$$K^+ \rightarrow \pi^+ + \pi^+ + \pi^-, 5.59\%$$

[4] All the information presented in this section, concerning the mass, the decays, lifetime, etc... can be consulted in [2].

● **Phi meson** ϕ **(**$s\bar{s}$**)** (m = 1019.4 MeV/c^2)

Thee phi meson is a state with pure strange-quark content are identified by their main decay channels:

$$\phi \rightarrow K^+ + K^-, 48.9\%$$

The measurement of ϕ meson is of great importance for the strangeness production. In pp collisions, ss^- pair production was found to be significantly suppressed in comparison to uu^- and dd^- pair. [3]. It is a neutral meson with $c\tau$=45 fm.

● **Proton** p **(**uud**) and antiproton** $\bar{p}$ **(**$\bar{u}\bar{u}\bar{d}$**)** (m = 938.27 MeV/c^2)

Proton is a stable particle that has not been observed to break down spontaneously to other particles.

● **Lambda** Λ **(**uds**)** (m = 1.116 GeV/c^2)

Is a neutral particle with $c\tau$=7.891 cm. The dominant Λ weak decays are:

$$\Lambda \rightarrow p + \pi^-, 63.9\%$$
$$\Lambda \rightarrow n + \pi^0, 35.8\%$$

The first decay has an important characteristic: The decays tracks are easily identified due their topology. ("V" structure) The second one is not so easy to detect because of the neutral particles final state.

1.3 Inelastic pp collisions

The hadron-hadron collisions can be classified in 4: Elastic processes (EL) and 3 different categories of Inelastic processes: Non Diffractive (ND), Single Diffractive (SD) and Double Diffractive (DD) based on the results of the products in the $\eta - \phi$ space. The total collision cross-section for hadron-hadron collisions in terms of the center of mass energy, (s), can be written as [4]:

$$\sigma_{total}(s) = \sigma_{elas}(s) + \sigma_{SD}(s) + \sigma_{DD}(s) + \sigma_{ND}(s) \tag{1.1}$$

The Fig. 1.2 shows a sketch of the event categories present in hadron-hadron collisions in the $\eta - \phi$ space. In elastic events there are no new particles produced by the collision. In the single diffractive and double diffractive there are new particles produced, but a clear dip is present between them in the central region. Finally in the non diffractive events the new particles are produced mainly in the central region.

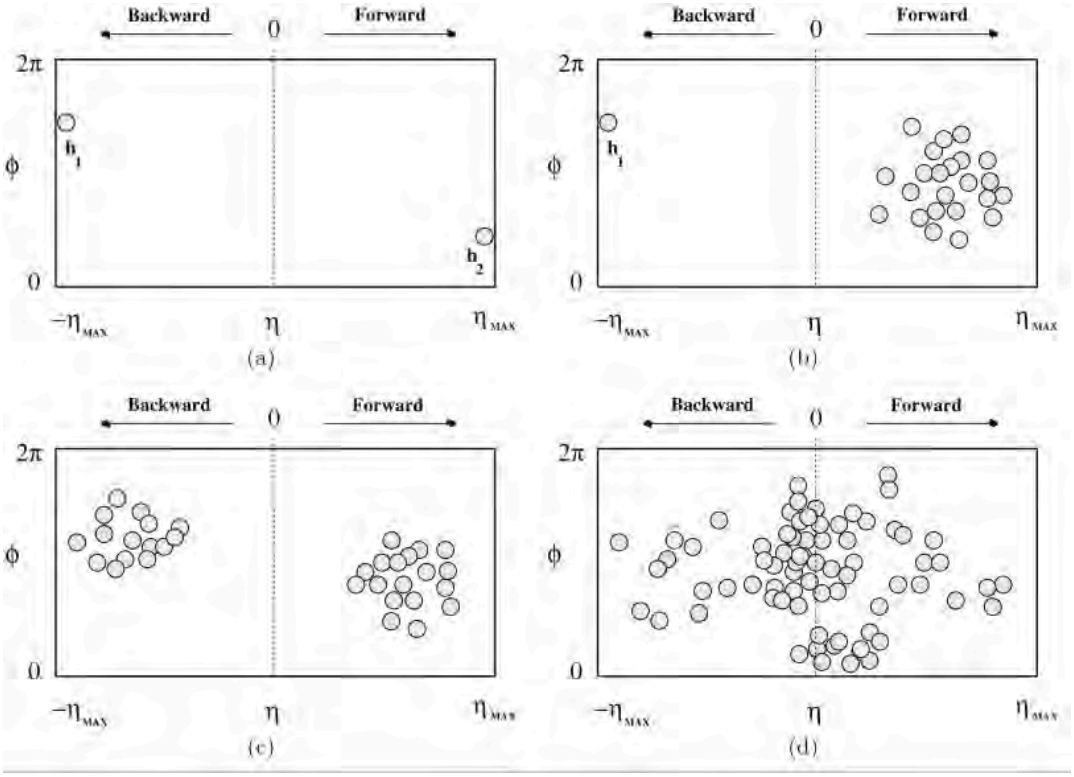

Fig. 1.2: Classification of hadron-hadron collisions. (a) Elastic, (b) Single diffractive, (c)Double diffractive, (d) Non diffractive. h_1 and h_2 are the collision hadrons. Figure from [4].

1.4 Event generators

At LHC energies understanding the final states of the pp collisions is an extremely challenging theoretical problem. There are hundreds of particles produced in a very wide range (many orders of magnitude) of momenta. The technique used to abord this problems is to separate the different types of processes of interest according to the scales of momentum transfer involved. The hard subprocesses can be computed perturbatively. At the lowest scales, of the order of 1 GeV, the partons confined within the beams interact non-perturbatively to create hadrons in the final state of the collisions. These are part of the soft processes which have to be modeled. Also the interplay between hard and soft QCD dynamics has to be studied. All three regimes of the collisions are analyzed with computer simulation based on Monte Carlo techniques. There are various software programs to simulate high energy pp collisions.The event usually combine perturbative QCD (pQCD) information, adding phenomenological results to simulate the *soft* part of the collisions like: the underlying event and the low p_{T} production.

PYTHIA

One of the most famous event generators is PYTHIA which is focused in hadronization studies. Its main feature is the Lund string fragmentation model (see section 1.5.1). The

PYTHIA software is an event generator with emphasis on particle production in collisions between elementary particles [6], in particular e^+e^-, pp and ep colliders. PYTHIA's main objective is to reproduce the data observables. The event generators contain a simulation of several physics aspects. The evolution of an high energy event may arrange this aspectecs as follows [6]:

- Initially two beam particles are coming in towards each other. Normally each particle is characterized by a set of parton distributions, which defines the partonic substructure in terms of flavour composition and energy sharing.
- One shower initiator parton from each beam starts off a sequence of branchings, such as q $\rightarrow$ qg, which build up an initial-state shower.
- One incoming parton from each of the two showers enters the hard process, where then a number of outgoing partons are produced, usually two. It is the nature of this process that determines the main characteristics of the event.
- The hard process may produce a set of short-lived resonances, like the Z^0 or $W^{\pm}$ gauge bosons, whose decay to normal partons has to be considered in close association with the hard process itself.
- The outgoing partons may branch, just like the incoming did, to build up final-state showers.
- In addition to the hard process considered above, further semihard interactions may occur between the other partons of two incoming hadrons.
- When a shower initiator is taken out of a beam particle, a beam remnant is left behind. This remnant may have an internal structure, and a net colour charge that relates it to the rest of the final state.
- The QCD confinement mechanism ensures that the outgoing quarks and gluons are not observable, but instead fragment to colour neutral hadrons.
- Normally the fragmentation mechanism can be seen as occurring in a set of separate colour singlet subsystems, but interconnection effects such as colour rearrangement or Bose$-$Einstein may complicate the picture.
- Many of the produced hadrons are unstable and decay further (see section 1.2.1).

When using PYTHIA it is important to have in mind that "does not represent a dead collection of established results, but rather **one of many possible approaches to the problem of multiparticle production** in high-energy physics, at the frontline of current research" [6].

1.5 Fragmentation functions

The procces in which the colored partons are transformed into colorless hadrons is known either as fragmentation or hadronization. The fragmentation functions are dimension-

less functions that describe the final state of a hadron produced in hard scattering processes, like e^+e^- annihilation, pp collisions, etc.

The fragmentation process has yet to be understood from the first principles, starting form the QCD Lagrangian. This has left the way clear for the development of a number of different phenomenological models. Three main schools are usually distinguished, string fragmentation, independent fragmentation and cluster fragmentation [6]. As the string fragmentation model is connected with the Monte Carlo generator used in this thesis (PYTHIA), the basic string fragmentation will be discussed.

1.5.1 String Fragmentation Model

The string fragmentation Model is described in detail in [6] and [7]. The main idea of this model is to produce hadrons from the energy of a color field between a quark (q) and antiquark ($\bar{q}$) moving apart from their common production vertex. This can be sketched as a colour flux tube stretched, with a size around 1 fm. The field is assumed to be a field with linear potential. The string in one dimension can be represented by the parametrisation of a cylindrical symmetric tube. As the distance between q and $\bar{q}$ increases, the energy in the string increases; when the string breaks up, this lead to the production of a new quark-antiquark pair (q' and $\bar{q}'$), and the system breaks up into two: $q\bar{q}'$ and $\bar{q}q'$ strings. If the energy of these two systems is large enough, more break-ups can occur leading to the production of more quark-antiquark pairs. From the hadron spectroscopy, the amount of energy per unit length of the string is deduced to be $\kappa \approx 1$ GeV/fm [6].

Mesons

In order to generate the new quark-antiquark pair, the Lund model invokes the idea of quantum mechanical tunneling. The strings breaks into two strings that eventually produce new quarks. The new $q_1\bar{q}_1$ pair tunnel out form the quantum vacuum at the point (z_1, t_1) of the space time. After some time, another pair $q_2\bar{q}_2$ in (z_2, t_2). This two adjacent breaks will form a meson. A sketch of the string break-up is shown if Fig. 1.3. The tunneling mechanism implies a suppression of heavy quark production. The reason is that charm and heavy quarks are not expected to be produced in soft fragmentation, but only in perturbative parton-shower mechanisms (q $\rightarrow q\bar{q}$). The ratios of the probabilities as an input in PYTHIA are u:d:s:$c \approx$ 1: 1: 0.3 : 10^{-11} [6].

Baryons

For the baryon production there are two different mechanisms: the diquark mechanism and the popcorn model. The diquark mechanism is an analogue to the meson production, where the string breaks up, but in this case, this break-up produces a pair diquark-antidiquark. These pairs are combined with the original pair, generating a baryon and

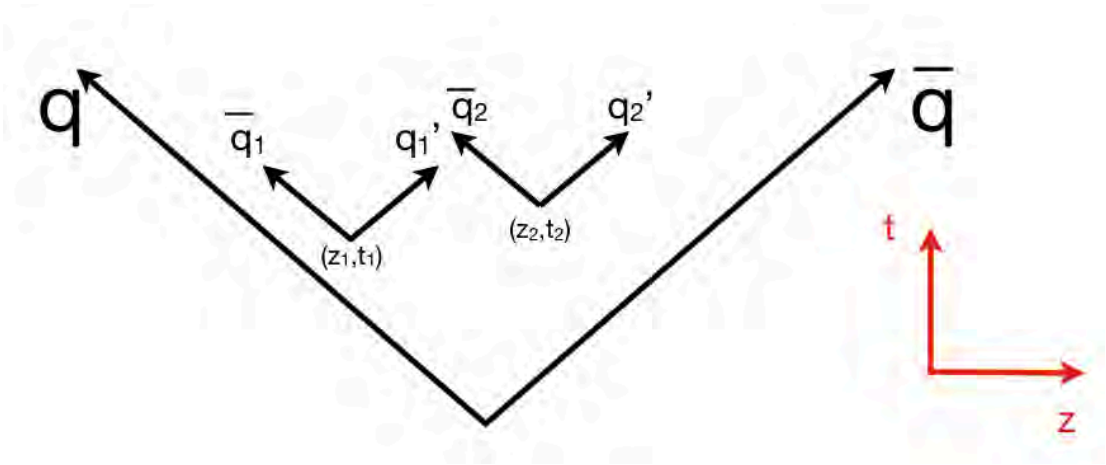

Fig. 1.3: Evolution in the space-time of the initial $q\bar{q}$ pair. The string break-up into new pairs: $q_1\bar{q}_1$ and $q_2\bar{q}_2$ with vertex in (z_1, t_1) and (z_2, t_2) respectively.

antibaryon. The probability to create a diquark pair rather than an antiquark is an input parameters of the diquark production model.

The popcorn model assumes a string color field produced by a quark-antiquark pair with a color: $q(color)\bar{q}(anticolor)$[5]; for instance, $q(r)\bar{q}(\bar{r})$. If the string breaks-up and original fragmentation creates a pair $q\bar{q}(\bar{r})$, but the virtual fluctuations can produce a $q_1(g)\bar{q_1}(\bar{g})$. In the last case the pair of quark are attracted, as well as the pair of antiquarks with an interaction between them. This can create an additional pair $q_2(b)\bar{q_2}(\bar{b})$, creating as a final state q(r)$q_1(g)q_2(b)$ and $\bar{q}(\bar{r})\bar{q}_1(\bar{g})\bar{q}_2(\bar{b})$. This configuration produces a baryon and antibaryon.

It is also possible to create two pairs of $b\bar{b}$ between the pair $q_1(g)\bar{q_1}(\bar{g})$. In this process the final configuration is baryon-meson-antibaryon. This two are the dominants configuration and their relative contributions is a model parameter.

1.6 Kinematic variables

The Fig. 1.4 shows the kinematic variables that relate particle momentum (p), to the dynamics that is occurring in the heavy-ion reaction. The main variables are the projection

[5]The possible color charges are: blue (b), green (g). red (r), and their respective anticolor.

of the momentum in the longitudinal plane (p_Z) and the projection of the momentum in the transverse plane (p_{T}) with reference to the beam axis. There is also two angles, θ which measures the inclination angle of the particle respect to the collision axis, and ϕ the azimuthal angle of the vector (p_{T}).

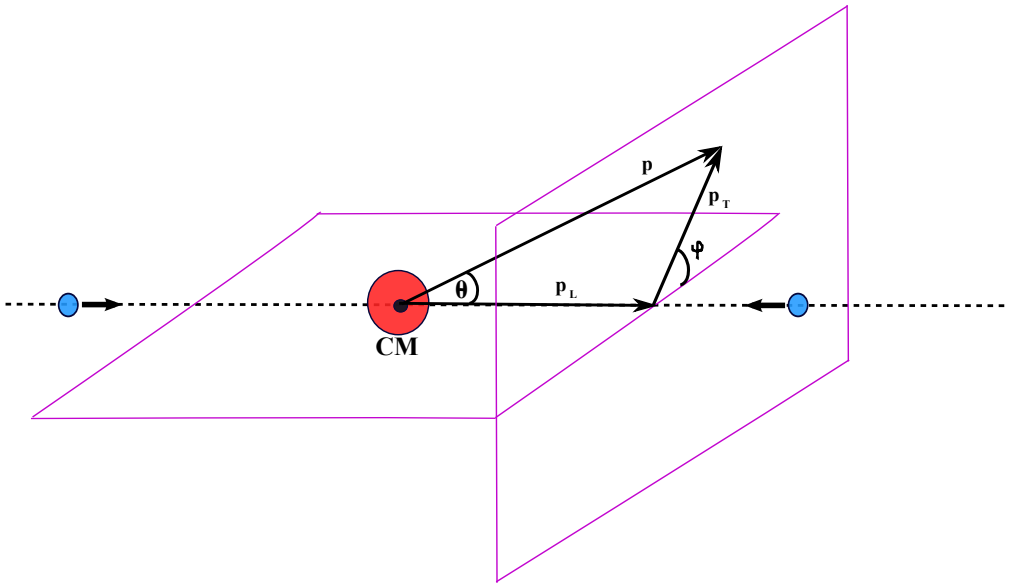

Fig. 1.4: Descomposition of particle momentum into the parallel p_L and the transverse p_{T} components in the CM frame. The inclination angle θ and the azimuthal angle ϕ is also shown.

1.6.1 Rapidity

Defining the rapidity, y, is very convenient for describing particle kinematics. The rapidity is defined as:

$$y = \left(\frac{E + p_Z}{E - p_Z} \right) \tag{1.2}$$

where E is the energy of the particle and p_Z the longitudinal component of the momentum. An advantage of the rapidity over the velocity is that it transforms straightforward under Lorentz boosts. If y is defined as 1.2, the boosted frame, y', is:

$$y' = y + y_{CM} \tag{1.3}$$

In symmetric collisions the CM frame has to be in the middle between the rapidities of the projectile $y_{CM} = y_p/2$. In this case the particle-rapidity spectrum must be symmetric around y_{CM} [8].

1.6.2 Rapidity gap

The rapidity "gap" Δy is defined as the difference between the rapidities of projectile and target.

1.6.3 Pseudorapidity

It is common that the particles are not identified, which means, we do not know their masses, and these are required to determine their rapidity. So that, is more convenient to use pseudorapidity for calculations. For this we have to consider when the mass of the particle is small relative to the momentum, this means the momentum alone determines the energy of the particle.

$$E = \sqrt{p^2 + m^2} \approx p \tag{1.4}$$

The pseudo-rapidity is defined as:

$$\eta = \frac{1}{2} \ln \left(\frac{p + p_L}{p - p_L} \right) = \frac{1}{2} \ln \left(\frac{1 + cos\theta}{1 - cos\theta} \right) = \ln \left(cot \frac{\theta}{2} \right) \tag{1.5}$$

Where θ is the angle of the particle emitted respect to the beam axis.So that, pseudo-rapidity is a natural variable to use, because the detector covers a well defined θ region with respect to the beam axis.

The Fig. 1.5 shows some values for η, as a function of the angle of the emitted particle respect to the beam axis.

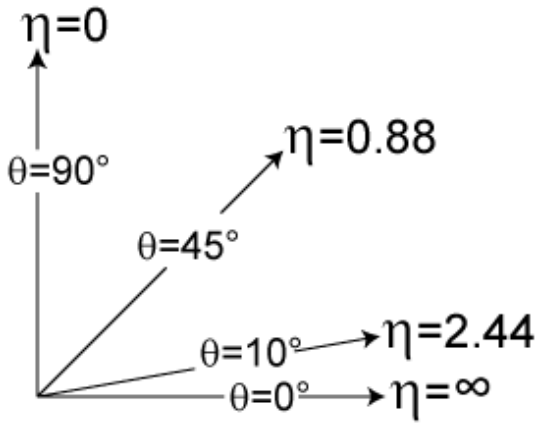

Fig. 1.5: Different values of η, as a function of the angle.

1.7 Heavy Ion Collisions

The ultrarelativistic Heavy Ion Collisions produce and environment with high energy, high parton density and high temperature, where the deconfinement should occur. These conditions generate a new state of matter known as *Quark Gluon Plasma* (QGP). This state is sensitive to the (perturbative) part of quark interactions with the gluon field at short distances (1 fm). Our goal is to study the quark gluon plasma measuring some of their properties through experimental observables like: p_{T} spectra, identified masses, etc.

Two types of information can be extracted from the QGP formed at high energy densities : The first consists on measuring the thermodynamical characteristics of the system in expansion like: chemical freeze-out, kinematical freeze-out, yields, etc. The second is the study of the passage of particles through the very dense system (jet quenching or parton energy loss).

1.7.1 Energy Loss mechanisms

The total energy loss of a particle traversing a very dense medium as the quark gluon plasma is composed by two different mechanisms: collisions and radiation. The collision energy loss is due to elastic scatterings with the particles of the medium, this mechanism dominates at low momentum. Most of the theories attribute the main contribution to partonic energy loss to radiative processes, produced by the gluon bremsstrahlung.

Some observables can be analyzed in order to confirm the effects of the medium-induced energy loss in nucleus-nucleus collisions. The natural method to extract this information is to compare a given observable in nucleus-nucleus (AA) collisions to those in proton-proton (pp) collisions. In this terms, we are comparing the properties of the properties of a "hot dense medium" (AA) and the "vacuum" (pp). Phenomenologically the jet quenching evidence can be observed by different measurements like: the suppression of the spectrum ($\frac{dN_{AA}}{dp_{\mathrm{T}}}$) of high p_{T} hadrons or high p_{T} dihadron back to back azimuthal correlations.

1.7.2 Parton energy loss measured in ALICE

Suppression of charged particle production at high p_{T} has been reported by ALICE in [12]. In this paper, ALICE quantify the nuclear modification effects at high p_{T} reporting the so-called nuclear modification factor R_{AA}. R_{AA} is defined as the ratio of the charged particle spectra in Pb-Pb to the one in pp normalized to the number of events respectively(N_{ev}^{AA}, N_{ev}^{pp}), scaled by the number of binary nucleon-nucleon collisions $< N_{coll} >$.

$$R_{AA} = \left(\frac{(\frac{1}{N_{ev}^{AA}})\frac{d^2N}{dp_T^{AA}d_\eta}}{< N_{col} > (\frac{1}{N_{ev}^{pp}})\frac{d^2N}{dp_T^{pp}d_\eta}} \right) \tag{1.6}$$

In the left panel of Fig. 1.6 the p_{T} spectra of primary charged particles are shown the ALICE results for central and peripheral of Pb-Pb collisions at 2.76 TeV. The black line denotes the scaled p_{T} from pp collisions at the same energy. It can be observed that the behavior of the p_{T} spectra for peripheral and pp collisions is very similar, whereas that, for central collisions, the p_{T} spectra is clearly suppressed respect to the pp reference in the p_{T} range higher than 2 GeV/c. The right panel of Fig. 1.6 shows the nuclear modification factor for central (0-5%) and peripheral Pb-Pb collisions. In peripheral collisions, the nuclear modification factor has a maximum close to 0.7 and seems to be constant for p_{T} higher than 2 GeV/c. In central collisions, the nuclear modification factor reaches a maximum value of 0.3 at p_{T} = 2 GeV/c, and then a suppression at p_{T} = 6-7 GeV/c. From p_{T} = 7 to 20 GeV/c the R_{AA} shows a significant rise.

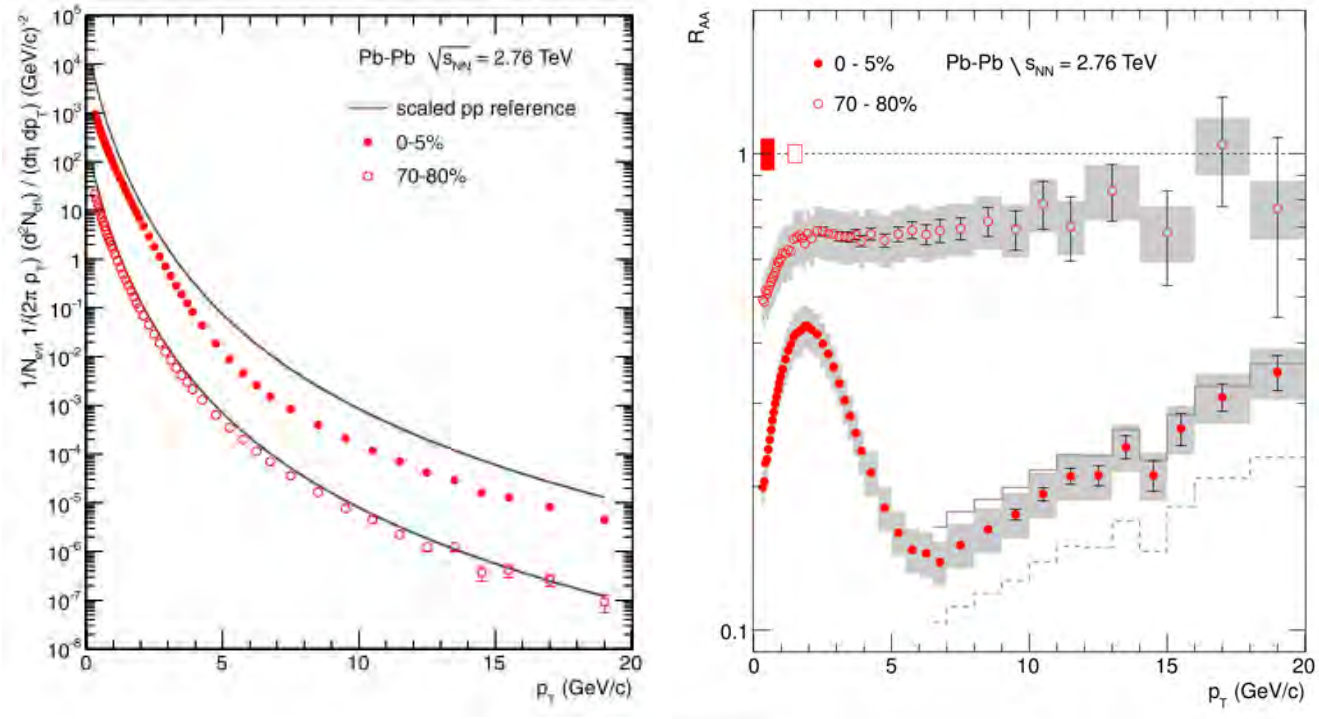

Fig. 1.6: Left panel: p_{T} spectra of primary charged particles are shown the ALICE results for central and peripheral of Pb-Pb collisions at 2.76 TeV. The black line denotes the scaled p_{T} in pp collisions. Right panel: Nuclear modification factor for central and peripheral collisions as a function of p_{T}. Both figures were taken from [12].

2

Experiment set-up: A Large Ion Collider Experiment

The ALICE experiment is one of the four main experiments at the Large Hadron Collider (LHC) [1] and was designed mainly to the study of strong interaction matter and the quark-gluon plasma at very high densities and extreme conditions in heavy ions collisions (Pb-Pb) at the LHC. The ALICE Collaboration has also studied collisions with pp collisions and p-A, which has provided a baseline comparison measurement to distinguish true dense matter effects present in Pb-Pb collisions from those already present in pp and pPb collisions. However, ALICE also allows to explore pp collisions in a completely new and interesting energy range, this jump in the energy regime historically is related to new discoveries. [2]

2.1 ALICE detector

ALICE detector shown in Fig. 2.1 is composed by a central barrel detector system and a forward system.

[1] The LHC at the European Organization for Nuclear Research (CERN) is a 27 km circular underground particle accelerator that straddles the border of France and Switzerland near Geneva. The design centre-of mass energy, of the LHC is $\sqrt{s}$ = 14 TeV for pp collisions, while for Pb-Pb collisions is expected to be $\sqrt{s}_{NN}$ = 5.52 TeV, this will exceed that available at RHIC by a factor of about 30. This is due to the fact that the maximum energy for ions is $E_{\max}\frac{Z}{A}$. Where Z is the proton number, A is the nuclear mass number, and E_{max} the maximum energy at the LHC. The $\frac{Z}{A}$ ratio determines the acceleration capability because while the uncharged neutrons are unaffected by the electromagnetic fields, they remain bound in the nucleus [5].

[2] With the LHC working at half of the maximum energy, CMS and ATLAS announced the discovery of a new particle on 4 July 2012, later identified as a Higgs boson. This discovery at the LHC energies marks the dawn of the new era in particle physics.

The central barrel covers mid-rapidity ($|\eta| < 0.9$) over the full azimuth and consist of: the L3 magnet which generates a magnetic field of 0.5 T, an Inner tracking system (ITS), a Time Projection Chamber (TPC) as the main tracking device of the experiment, a Time Of Flight (TOF) detector, a ring-imaging Cherenkov detector (HMPID), a transition radiation detector (TRD), an electromagnetic calorimeter (PHOS). A Cosmic Ray DEtector (ACORDE) is used to trigger in cosmic rays and is located at the top of the L3 magnet.

The forward system includes a muon spectrometer (-4.0 $< |\eta| <$ -2.4) and some forward detectors for multiplicity measurements FMD, PDM and T0 and VZERO which are used as trigger detectors.

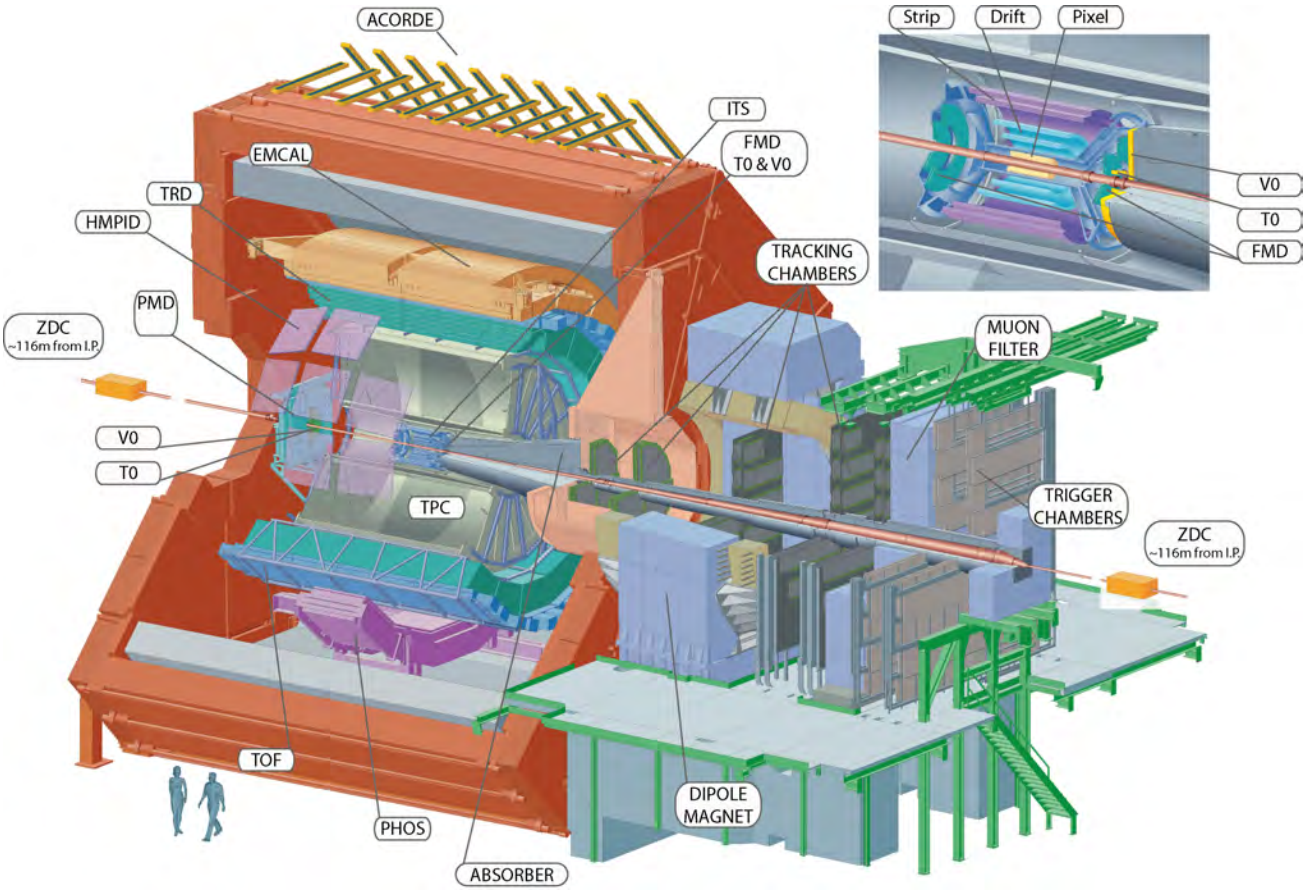

Fig. 2.1: ALICE detector schematic view.

2.1.1 VZERO

VZERO detector [13] is a detector consisting of two circular arrays of scintillators , known as V0A and V0C, located asymmetrically on either side of the nominal ALICE interaction point. V0A is located to 330 cm from the interaction point on the opposite side to the muon spectrometer while V0C is located to 90 cm from the interaction point in front of the hadronic absorber.

Each of the VZERO arrays is composed by 32 counters distributed in four rings in radial direction and each ring is divided in eight sectors of 45^o, as shown in Fig. 2.2. Each of this rings covers different rapidity units, the values for both VZERO arrays are shown in table 2.1

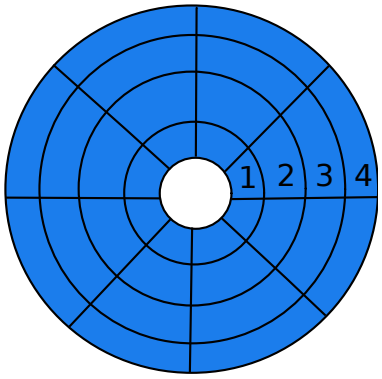

Fig. 2.2: Segmentation of V0A and V0C detectors.

This detector has several functions:

1. **Trigger:** one of the main functions of the VZERO detector is to provide a minimum bias (MB) trigger for the detectors in the central barrel both in pp and Pb-Pb collisions. Also, provides centrality triggers in Pb-Pb collisions, classifying them in central and semi-central through the measure of multiplicity of the events. Two Minimum-Bias (MB) definition has been used for pp collisions: In 2009 and 2010 data the ALICE MB trigger MB_{OR} was set requiring a hit in the SPD or in either one of the VZERO arrays. Since 2011 the ALICE MB trigger moved to a rigorous coincidence condition either between both VZERO arrays and the LHC bunch crossing signals or between both VZERO arrays.
2. **Background rejection** Background in the collision comes from interactions between the beams injected in the accelerator and the residual gas or the beam halo. The particles coming from real collisions and the particles coming from beam-gas background can be separated, comparing the arrival time of the particles to both of the VZERO arrays.
3. **Luminosity** The VZERO system provides the integrated luminosity for the ALICE experiment.

Ring	V0 A			V0 C		
	η_{max} / η_{min}	θ_{max} / θ_{min}	r_{max} / r_{min}	η_{max} / η_{min}	θ_{max} / θ_{min}	r_{max} / r_{min}
1	5.1 / 4.5	0.7 / 1.3	4.3/ 7.5	-3.7 / -3.2	177.0 / 175.3	4.3/ 7.5
2	4.5 / 3.9	1.3 / 2.3	4.3/ 7.5	-3.2 / -2.7	175.3 / 172.4	4.3/ 7.5
3	3.9 / 3.4	2.3 / 3.8	4.3/ 7.5	-2.7 / -2.2	172.4 / 167.5	4.3/ 7.5
4	3.4 / 2.8	3.8 / 6.9	4.3/ 7.5	-2.2 / -1.7	167.5 / 159.8	4.3/ 7.5

Table 2.1: Values of pseudorapidity and angular acceptance (deg.), and z (cm) position along the beam axis of V0A and V0C rings, as seen from the ALICE nominal position.

2.1.2 Inner Tracking System: ITS

The ITS [14] is the closest detector to the beam axis, it consists of six silicon layers segmented in 3 sub-detectors of different kind as shown in Fig 2.3. Two layers of Silicon Pixel Detectors (SPD) in the innermost part, located at a radii of 3.9 and 7.6 cm respectively, this two layers are very important for finding the primary vertex and to measure the impact parameter of the secondary particles from weak decays. Next there are two layers of Silicon Drift Detectors (SDD) located at a radii of 15.0 and 23.9 cm respectively, this two layers provides 2 of the 4 samples of energy loss (dE/dx) necessary for the PID in the ITS [16]. The two outermost layers located at a radii of 38.4 and 43.4 are Silicon Strip Detectors and are very important since they connect the ITS tracks from the ITS to the TPC, moreover, the SSD provide the other two samples of (dE/dx) for the PID at low p_{T} .

The ITS covers the pseudo-rapidity range ($|\eta| < 0.9$) for all the primary vertex reconstructed within the length of the interaction diamond (1 σ), *i.e.* 10.6 cm along the beam axis. Their main functions are the primary vertex reconstruction with a resolution > 100 μm, tracking and particle identification (PID) for particles with p_{T} lower than 100 MeV and reconstruct particles which do not reach the TPC.

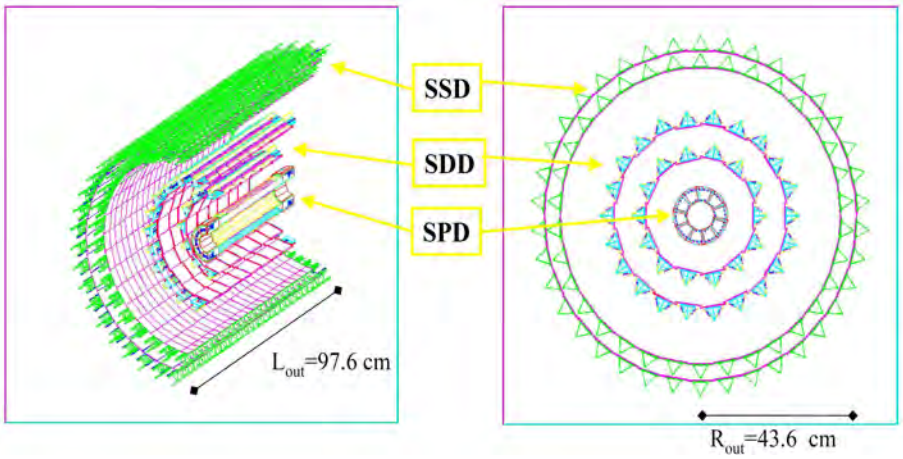

Fig. 2.3: Schematic design of the ITS layers.

2.1.3 Time Projection Chamber: TPC

The Time Projection Chamber is the main tracking and PID device of the central barrel, covering an azimuthal angle of 2π and ($|\eta| < 0.9$). The TPC, shown in Fig. 2.4, is a cylindrical detector with inner radius of about 85 cm, an outer radius of about 247 cm, and an overall length along the beam direction of 500 cm. A high voltage central membrane splits the drift region in two regions, resulting in a maximum drift time of 94 μs [17]. The TPC is filled with a gas mixture of Ne, CO_2 and N_2. If a charged particle crosses the TPC volume, it ionizes gas atoms along its trajectory and a consequence, it loses an amount of energy per track length unit (dE/dx). The amount of energy loss depends on the mass of the particle.

A central membrane located at z = 0 and at HV = 100 kV produces an uniform electric field (see Fig. 2.4) through which the electrons created by the gas ionization, drifts towards the end plates on either sides of the TPC.

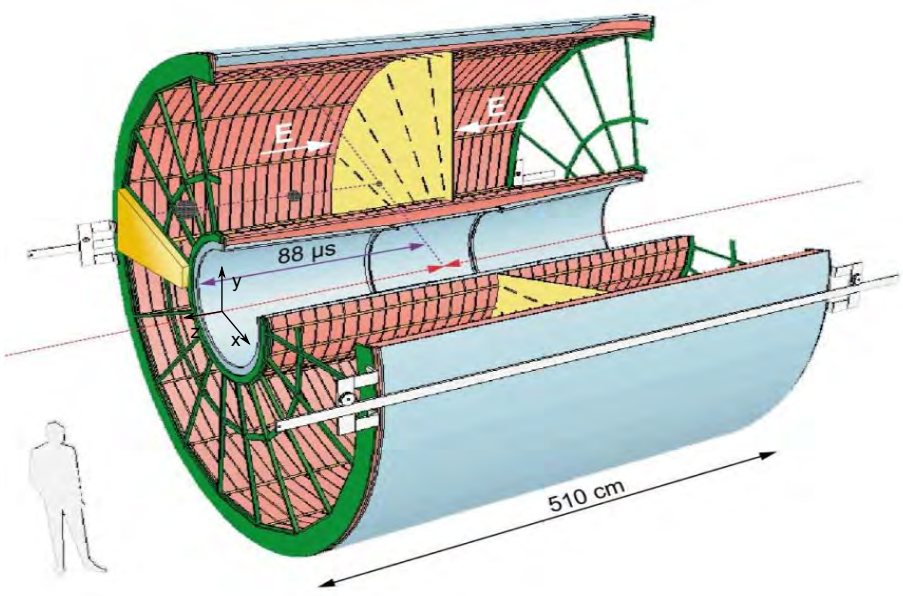

Fig. 2.4: Schematic layout of the Time Projection Chamber.

The TPC end-plates are each segmented into 18 trapezoidal sectors and equipped with multi-wire proportional chambers with cathode pad readout. The sectors are segmented radially in two chambers with varying pad sizes, optimized for the radial dependence of the track density. There are a total of 159 pad rows radially, this means a track which crosses the whole TPC is thus sampled in each pad row. And the dE/dx is measured independently in each one, via the charge of the corresponding clusters.

The TPC allows the tridimensional reconstruction of the tracks produced by the incident charged particles. The pads provide the reconstruction of the coordinates (x ,y) via de distribution of the induced signal. The position of the particle in the drift direction is obtained with the measure of the drift time (Δt) till the readout planes. The drift velocity of the electrons (v_e) in the gas is known; with this the coordinate z is calculated with $z = v_e \Delta t$. Such a three-dimensional signal is called cluster.

2.1.4 Time Of Flight: TOF

The TOF detector has a fundamental role for the PID of pions, kaons and protons in ALICE, it covers the central region of pseudo-rapidity ($|\eta| < 0.9$) and a full azimuthal angle of 2π, in the p_{T} range 0.5 GeV/c till 2.5 GeV/c, allowing to extend the PID p_{T} reach of the TPC. A schematic view is shown in Fig. 2.5. The TOF detector is mounted on an cylindrical structure with an inner radius of 370 cm and an external radius of 399 cm, and the barrel length is around 745 cm. The TOF detector is composed by 18 azimuthal sec-

tors, each sector is divided in 5 modules along the beam direction. Each module contains Multi-gap Resistive Plate Chambers (MRPC).

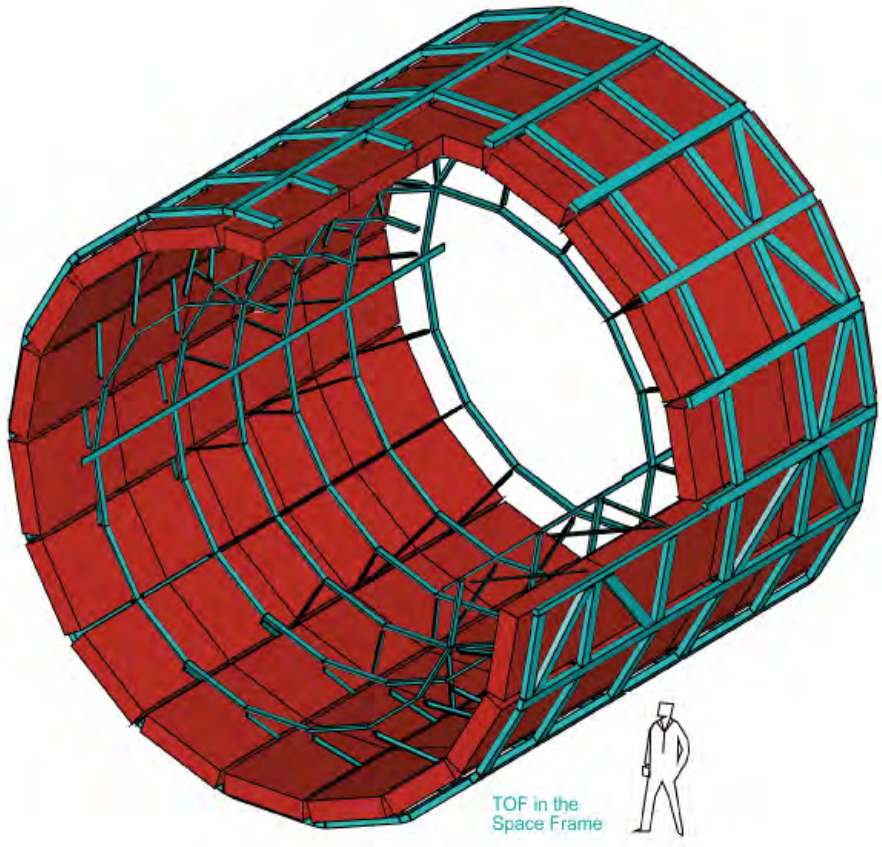

Fig. 2.5: TOF Schematic design

The start time for the measurement of the time of flight of a particle is provided by the T0 detector or estimated using the particle arrival times at the TOF detector. A combinatorial algorithm based on based on the χ^2 minimization between all the possible mass hypotheses is used in the latter case. It can be used when the events has at least 3 particles in the TOF detector. This method is used for events without T0 signal. If both methods are unavailable, an average of TOF start time for the run is used instead [18]. For Pb-Pb collisions it is possible to extend PID till p_{T} = 3.0 GeV/c thanks to the good T0 resolution.

2.1.5 High Momentum Particle IDentification detector: HMPID

The HMPID [19] is mainly designed for the PID at high p_{T} in ALICE covering the pseudo-rapidity range ($|\eta| < 0.5$), and an azimuthal angle of 57.61^o, extending the p_{T} range for pions and kaon till 3-0 GeV/c and till 6.0 GeV/c, which corresponds to 5 % of central barrel phase space.

The HMPID design is shown in Fig. 2.6, it has an active area of 10.5 m^2 divided in 7 identical modules of proximity focusing ring imaging Cherenkov detectors (RICH). It is

located about 5 m in the radial direction from the beam. The identification is based on the Cherenkov angle of the ring which is produced by the charged particle.

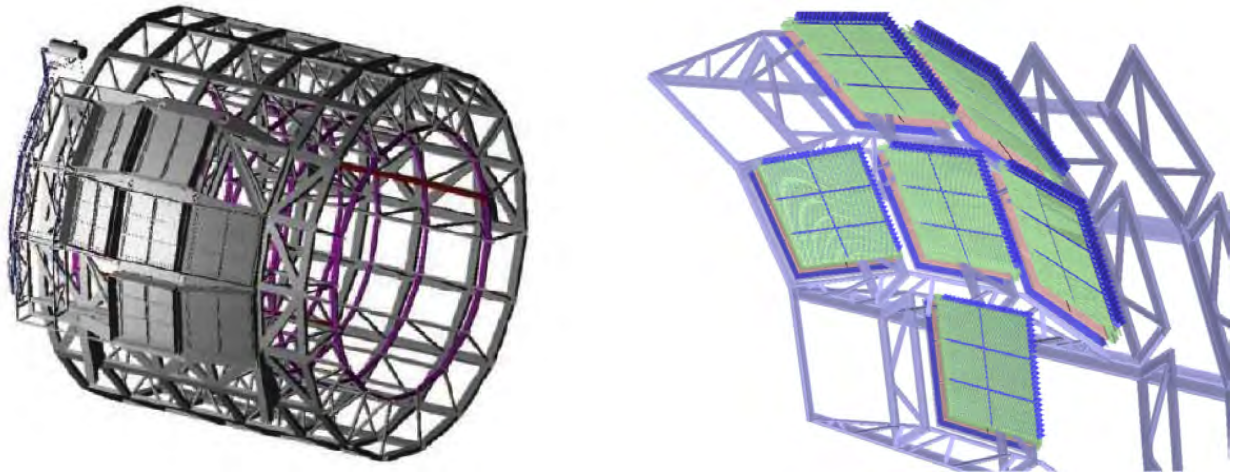

Fig. 2.6: *Left*: HMPID position in the central barrel. *Right*: Example of an HMPID module.

The HMPID working principle is the following: When a charged particle pass through the radiator C_6F_{14}, the radiator (with refractive index $n \approx 1.289$ at 175nm), emits Cherenkov photons that arrives to a thin layer (300 μm) of CsI , where the photoelectrons are produced, the MWPC accumulate charge and induces a positive signal in the pad plane with the readout electronics. The photon position is determined by the center of the charge induced in the cathode pad plane. To avoid that the electrons produced by the proximity gap full of CH_4 enter in the MWPC region. The Cherenkov angle produced by the charged particle only depends of the velocity of the particle (β) and the refractive index (n) of the radiator as:

$$\cos\theta = \frac{1}{n\beta}, \tag{2.1}$$

2.2 Software tools

The software framework is a set of tool that allows the data processing. A special software used in most of the high energy physics experiments is ROOT [20]. ROOT provides a large set of tools in order to perform different kind of analysis as: generation of events, detector simulation, data acquisition, framework for data analysis or visualization. It is based on a C++ computer language.

2.2.1 Aliroot

The offline framework of the ALICE experiment is known as Aliroot [21] and it is based on ROOT. Aliroot is the code for both simulation or data reconstruction of the ALICE

detector performance. Its role is shown schematically in Fig 2.7. It also contains tools for the data analysis. In case of simulation the data is produced by the event generators (PYTHIA, PHOJET, HERWIG), this data generated contains all the information (PID and momentum) about the generated particles. The data produced by the event generators are then transformed into data representing the detector response. The information is reduced to that generated by particles crossing a detector, the interactions between the particles and detectors are simulated by the transport code GEANT3 [22]. Finally, "raw data" are produced from simulated events. The following processes are the reconstruction and the analysis data, this takes as input and make exactly the same treatment for the real or simulated data. The reconstruction algorithms (explained in the section 2.2.3) have to reconstruct the full information about the particles trajectory with all the detectors involved. To evaluate the software and detector performance, simulated events are processed through the whole cycle and finally the reconstructed particles are compared to the Monte Carlo generated ones. With this the efficiency of the detector can be evaluated as shown in chapter 4.

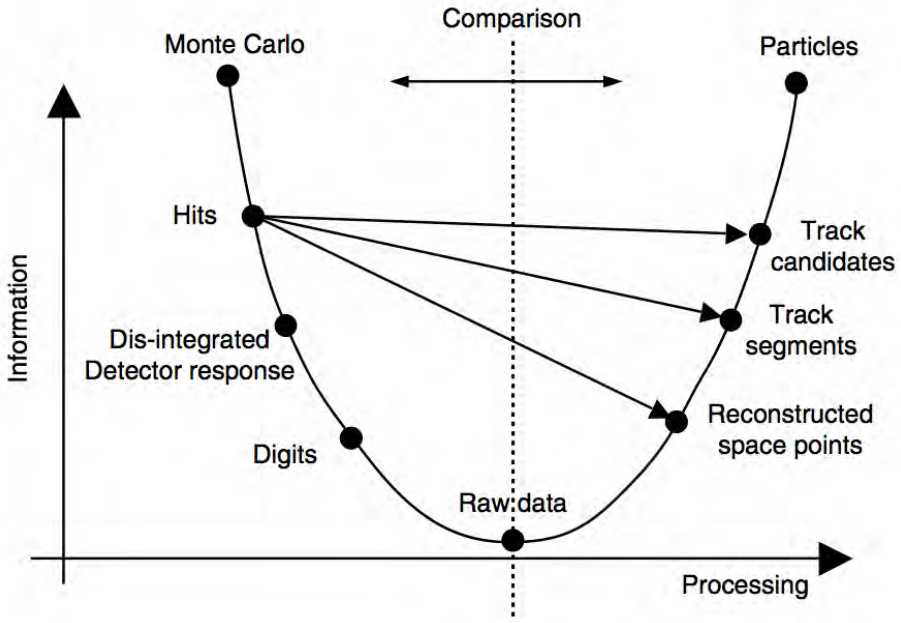

Fig. 2.7: Data processing framework. The left part shows the chain followed by the events generators and the right part the chain followed by the particles produced in real data. The information in both cases are stored in the same way as *Raw data*. Fig. taken from [14].

2.2.2 Detector response simulation

Complementing the event generators it is necessary to simulate the pass of particles through the detectors. It is very important to have a a high-quality and reliable detector response simulation code. This is commonly referred as transport code.

GEANT 3

The transport package implemented by ALICE is GEANT 3 [9]. GEANT 3 [3] is a software designed to describe the pass of particles through matter based on Monte Carlo methods and has been extensively used by the High Energy Physics community for simulation on the detector response.

The main GEANT features are:

- Full detector simulation: geometry, material, size, coordinates, etc.
- Particle transport trough the detectors, taking into account the detectors, and the physics interactions between the material and the particles produced by the events generators.
- Store the trajectories and the detectors response.
- Visualization of the detectors and the tracks.

FLUKA

Another detector response simulation is FLUKA [4]. FLUKA [11] is a multipurpose transport Monte Carlo code, able to treat hadron−hadron, hadron−nucleus, neutrino, electromagnetic, and μ interactions up to 10000 TeV. It also provides an alternative to GEANT3 to full detector simulation. FLUKA has particularly important role in ALICE in the design of the front absorber and the beam shield.

2.2.3 Reconstruction method

Track reconstruction is of vital importance and one of the most challenging task in ALICE. Determining the momentum of the particles as close as possible to the point where they were produced is the main goal on the reconstruction process. Also, is very important that the reconstruction procedure be capable of extrapolate the track though all detectors situated on the outermost part of the interaction point, this provides the particle identification method in some of the sub detectors like TOF and HMPID.

Primary vertex reconstruction with SPD

The primary vertex reconstruction in ALICE [14] is mainly obtained by the silicon pixel detectors of the ITS. The algorithm used in the SPD correlate the space points [5] in the two pixel layers. This starts by looking at the distribution of the z coordinates of the

[3] Acronym of Geometry ANd Tracking.

[4] Acronym of FLUktuierende KAskade first designed for the hadron interactions in radiation studies connected with the 300 GeV Project at CERN [10].

[5] A reconstructed space point means the position estimated where the particle crossed the sensitive element of a detector.

reconstructed space points in the first pixel layers. At a vertex z coordinate z_{true}=0 the distribution is symmetric and its centroid (z_{cen}) is very close to the nominal vertex position. If the primary vertex is moved along the z axis, a fraction of the hits will be lost and the centroid of the distribution will not be the primary vertex. The correlation between the true vertex position and the distribution for primary vertex located not too far (up to 10 cm) from z_{true}=0 is shown in Fig. 2.8. The saturation effect at large z_{true} values of the vertex position, is not critical, since the procedure is only meant to find a rough vertex position, in order to introduce some cut along z.

A monotonic relationship, through a polynomial fit, was used to evaluate a first approximated value (z_v^0 of z_v) from the centroid of the z coordinate distribution of the reconstructed space points.

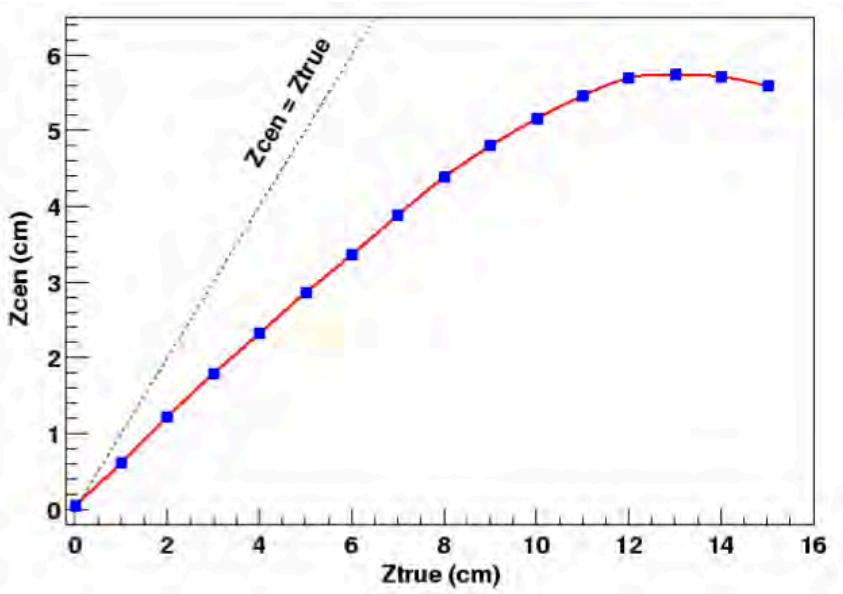

Fig. 2.8: Correlation between the centroid of the z distribution, z_{cen}, and the true position of the primary vertex, z_{true} Fig. taken from [14].

The Fig 2.9 shows a sketch of the algorithm used to correlate the two point in the two SPD layers. A first estimation of the vertex location, z_v^0 is made first, using the distribution of the reconstructed points in the innermost layers. The correlation of the points z_1, and z_2 in the two layers is then considered, selecting only those pairs which give a vertex position z_v within the confidence region between z_{min} and z_{max}.

A similar approach is applied to the reconstruction of the vertex position on the transverse plane. The deviation of the track projection from a straight line is small, and can be obtained even with a linear approximation, specially for high momentum particles. The true coordinates can be found through an iterative procedure. By taking centroids x_v, y_v, and z_v distributions, it is possible to estimate the location of the primary vertex in three dimension [14].

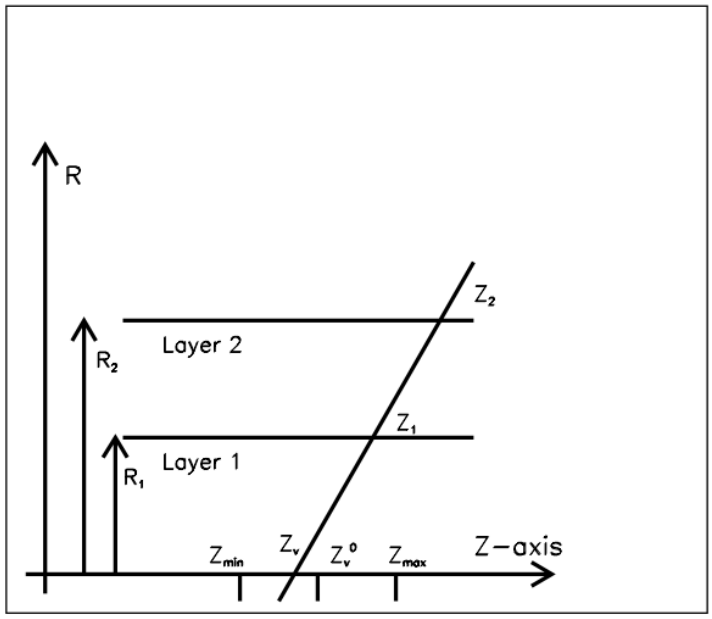

Fig. 2.9: Sketch of the algorithm used to correlate the two point in the two SPD layers. Fig.taken from [14]

Track reconstruction

The track reconstruction in ALICE is performed using the Kalman filter approach, which is a powerful method for statistical estimations and predictions. This approach provides a lot of attractive properties. The method can be used in both track finding and track fitting simultaneously, and also provides a natural way to find extrapolation of a track from one detector to another.

The reconstruction begins with cluster [6] finding in all of the central barrel detectors (see Fig. 2.10). With the two SPD layers of the ITS, the primary vertex is estimated and the track finding begins. It starts at the outer radius of the TPC where the density of clusters is minimal, the tracks "candidates" are found and then they are propagated to the inner edge of the TPC (TPCin). At this point the ITS tracker extends the TPC tracks to the inner point of the ITS (ITSin) and then to the primary vertex. After all the TPC tracks are assigned to the ITS, the ITS stand-alone is applied to the rest of ITS clusters, in order to recover the tracks that were not reconstructed in the TPC because of the dead zones between the TPC sectors, the p_{T} cut-off or decays.

The tracking is restarted from the vertex back to the outer layers of the ITS, and then repeated towards the outer wall of the TPC (TPCout). For the track labeled by the ITS tracker as potentially primary, several particle mass-dependent, time of flight hypotheses are calculated. These hypotheses are useful for the particle identification method with TOF detector. When the the track reconstruction reaches the outer wall of the TPC

[6] *Cluster*: This is a set of adjacent (in spacer/or in time) digits that were presumably generated by the same particle crossing the sensitive element of detector. *Digit*: This is a digitalized signal (ADC count) obtained by a sensitive pad of a detector at a certain time.

again, the precision of the track parameters is sufficient to propagate the tracks to the TOF (TOFout), TRD (TRDout) and HMPID (HMPIDout) detectors. When the tracks are extrapolated to TOF (TOF refit) and HMPID (HMPID refit) they acquire the PID information. The last step is a refit procedure backward to the inner radius where the track was reconstructed (TPC and ITS refit). These tracks are called global tracks. The reconstructed tracks, the PID information from the detectors, kink, V0 and particle decays are stored for each event, these objects are known as ESDs [7]. The ESDs contains all the information necessary for the analysis.

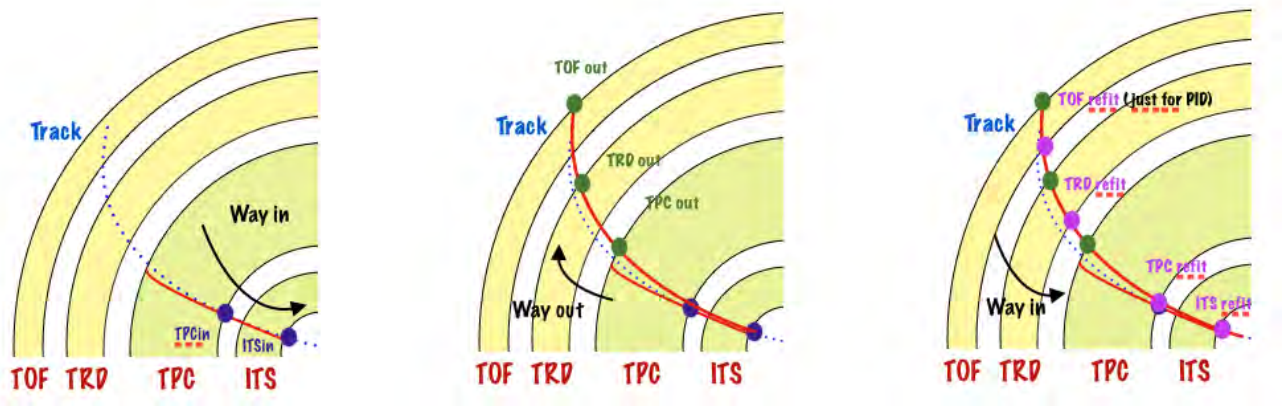

Fig. 2.10: Kalman Filter reconstruction steps.

2.3 Potpourri of ALICE pp results

Some interesting pp studies already performed by the ALICE collaboration are listed below.

Anti-baryon to baryon ratio

Anti-baryon to baryon spectra ratios were recently reported by ALICE [8] baryon anti baryon. The ratio $\bar{B}/B$ was measured for protons and hyperons [9] within the ALICE acceptance. The ratio increases with increasing the beam energy reaching values compatible with unity for $\sqrt{s}$ = 7.0 TeV. Another interesting result is the ratio $\bar{B}/B$ for particles with strange content at a given energy. This provides information about the contribution of mechanism of baryon production. For instance, if the strangeness of the observable increases, one reduce the contribution of the process related to the stopping of different constituents of beam particle. In this case we expect the ratio $\bar{B}/B$ closer to the unity, which it is not observed by ALICE.

[7] Event Summary Data.

[8] *Eur. Phys. J. C* (2013) 73: 2496.

[9] Baryons and their respective anti baryons containing strange quarks are called *hyperons*, i.e. Λ, charged Ξ and Ω.

Event shapes variables: Transverse sphericity (S_T)

Measurements of the sphericity of primary charged particles in pp at $\sqrt{s}$ = 0.9, 2.76 and 7 TeV has been reported by ALICE [10] is a momentum space variable, commonly classified as an event shape observable. The lower and upper limits of this variable are related to two specific configurations of events: “jetty like“ and isotropic events respectively. No energy dependence of the mean sphericity has been observed, but a dependence on the multiplicity of the events seems to present. The combined study of the sphericity and the mean p_{T} comparison between data and Monte Carlo generators has provided an indication that most of the events generators produce events with higher multiplicity by generating more-back to-back jets, which corresponds to low sphericity events.

Pion, Kaon and Proton production at $\sqrt{s}$ = 900 GeV

First ALICE results on charged hadron production at $\sqrt{s}$ = 900 GeV has been already reported [11]. Particle Identification is performed using the specific energy loss in the ITS and TPC. Also the time of flight is used to identify hadrons at higher momenta. Several particle identification methods are combined over different momentum ranges, which result in a combined spectra for pions, kaons and protons from p_T = 100 MeV/c to 2.5 GeV/c. The Monte Carlo models (Pythia different tunes and Phojet) give a poor description of the data. The ratio K/π is in agreement with previous results at lower energies. The p/π is compared to PHENIX results and seems to increase, however it is not conclusive due to size of the errors.

[10] *Eur. Phys. J. C* (2012) 72:2124.
[11] *Eur. Phys. J. C*(2011) 71:1655.

3

Particle Identification in ALICE

In ALICE most of the techniques for Particle Identification (PID) are used. This allows the production of pions, kaons and protons to be measured over a wide transverse momentum (p_{T}) range. The ITS and the TPC measure the specific energy loss (dE/dx) of the particle, which provides track-by-track PID in the p_{T} range 0.1 to $\simeq$1.0 GeV/c. The TOF contributes to PID for the p_{T} range between 0.5 GeV/c and 3-4 GeV/c, while the HMPID extends the identification of protons till $p_{\mathrm{T}} \simeq 6$ GeV/c. High p_{T} particles (up to 20 GeV/c) are identified using the relativistic rise of the specific energy loss in the TPC.

The separation power in number of standard deviations between two particles can be calculated just as the difference (Δ) between the mean of the peak divided by the Gaussian width (σ) of the detector response for the parcel. The Fig 3.1 shows the separation power of the detectors in the central barrel between kaon and pion (left panel) and separation between proton and kaon (right panel) as a function of p_{T} . Please note that this separation is for Pb-Pb collisions, for pp collisions the p_{T} range for the two sigma separation has lower p_{T} range.

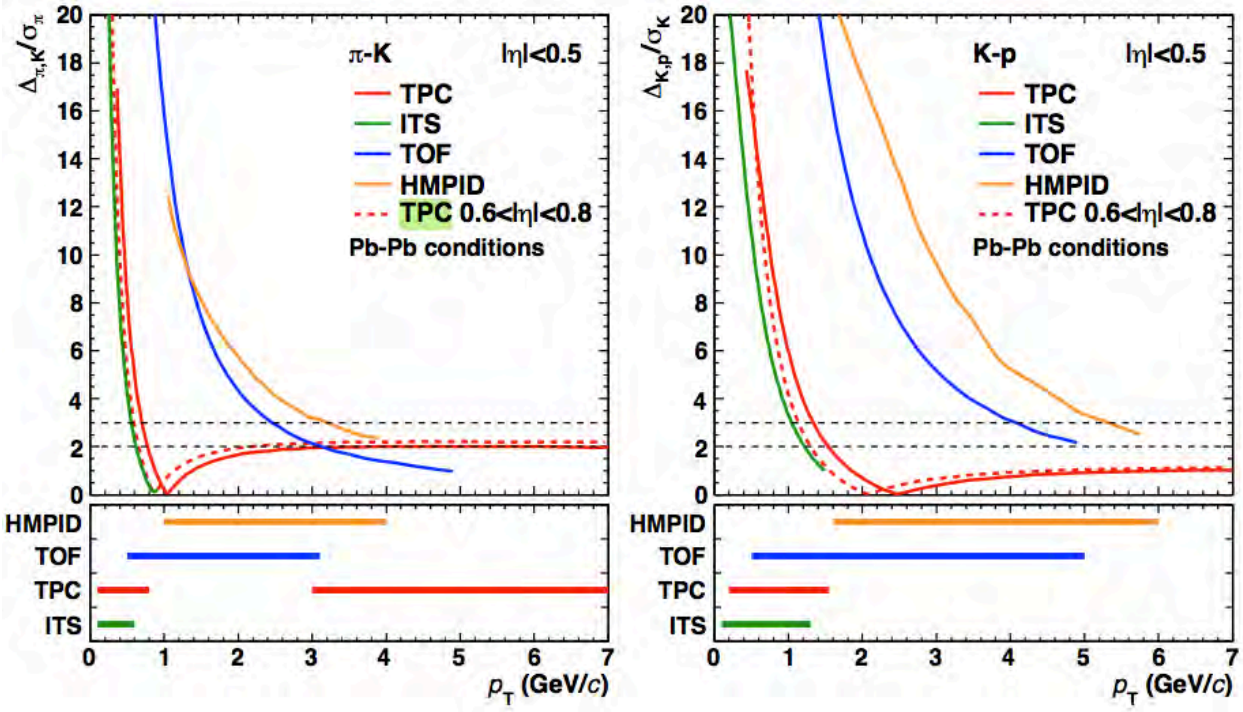

Fig. 3.1: Separation power in term of number of standard deviations of hadron for some detectors in the central barrel. Figure taken from [15].

3.1 ITS PID

As mentioned above two of the SSD layers and two of the SDD layers provide the dE/dx measurement that is used for PID in the non relativistic ($1/\beta^2$) region. The ITS is the only detector that can provide PID for very low momentum particles or particles not reconstructed by the TPC.

The Fig 3.2 shows the PID capabilities of the ITS as a function of momentum. Pions, kaons and protons can be observed, a small band can be seen below 200 MeV, this corresponds to electrons and muons, which can not be distinguished from pions after this values. The dE/dx sample as a function of the parameter $\beta\gamma$ ($\beta\gamma$= p/m) for pions, kaons and protons is parametrized via:

$$dE/dx = \begin{cases} a_0 \frac{a_1+2\ln(\gamma)-\beta^2}{\beta^2}((\beta\gamma - a_3)^2) + a_4), & \text{if } \beta\gamma < a_2 \\ a_0 \frac{a_1+2\ln(\gamma)-\beta^2}{\beta^2}((a_2 - a_3)^2 + a_4), & \text{if } \beta\gamma \geq a_2 \end{cases} \tag{3.1}$$

with p = momentum in the primary vertex, and a_i are free parameters [23]. The solid lines in Fig 3.2 are calculated for the different species with this parametrization. The parameters are obtained for different data samples.

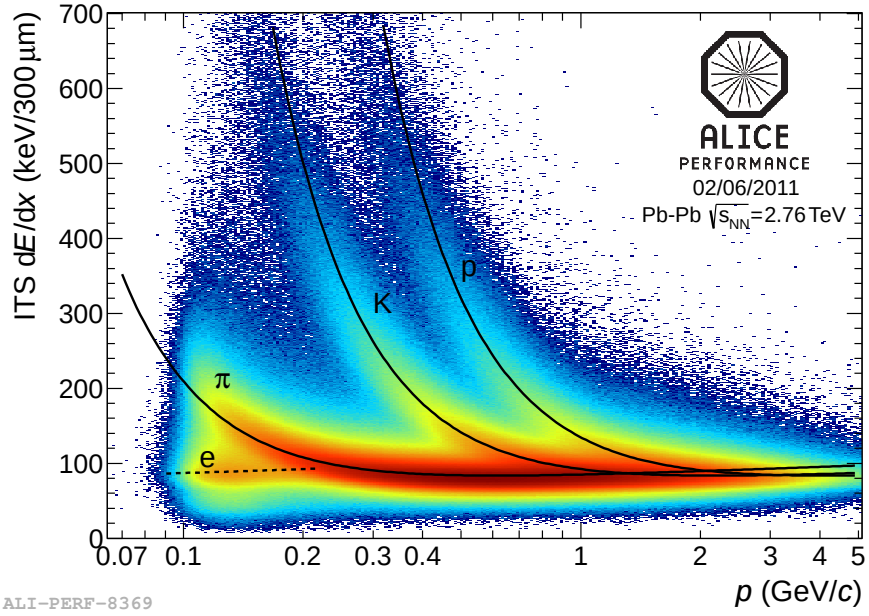

Fig. 3.2: Energy loss signal as a function of momentum measured with the ITS in Pb-Pb collisions at $\sqrt{s}$ = 2.76 TeV.

3.2 TPC PID

The dE/dx measurement for the TPC is obtained from the number of clusters assigned to the track, so that it can be a maximum of 159 samples. The dE/dx information is extracted from the total charge, Q_i, which represents the sum over the pads in one row. The energy loss distribution measured shows a tail towards higher energy losses, which leads to a problem when one try to estimate the mean energy loss, which in this case does not corresponds to the average energy loss. To avoid this problem a truncated mean method is used.

The truncated mean $< S >_\eta$ method consist in a cut-off parameter η between 0 and 1. The truncated mean is defined as the average over the $m = \eta n$ lowest values among the Q_i samples.

$$< S >_\eta = \frac{1}{m} \sum_{1}^{m} S_j \tag{3.2}$$

where $i = 0, \ldots, n$ and the sum extend over the lowest m elements ordered Q_{i-1},Q_i for all the sample. With Monte Carlo simulation the best value of η found is between 0.35 and 0.75. This range (obtained empirically) produce values of $< S >_\eta$ in a gaussian

distribution. For the ALICE TPC this value is set to η = 0.5 but will be subject of further investigation and may be replaced with a a smooth weighting function. $< S >_\eta$ is denoted as the TPC signal and is the quantity denoted as dE/dx and is called TPC signal [24].

For the TPC signal or TPC dE/dx the values are calculated using a parametrization of the Bethe-Bloch curve used previously in the ALEPH experiment [1], in the following way:

$$f(\beta\gamma) = \frac{P_1}{\beta^{P_4}}(P_2 - \beta^{P_4} - \ln(P_3 + \frac{1}{(\beta\gamma)^{P_5}}) \tag{3.3}$$

Where the parameters P_i depend of the data sample used in the analysis.

The Fig 3.3 shows the dE/dx in the TPC as a function of the momentum. The solid lines represent the value calculated via the Bethe-Bloch parametrization for the different species: electrons, pions, kaons, protons.

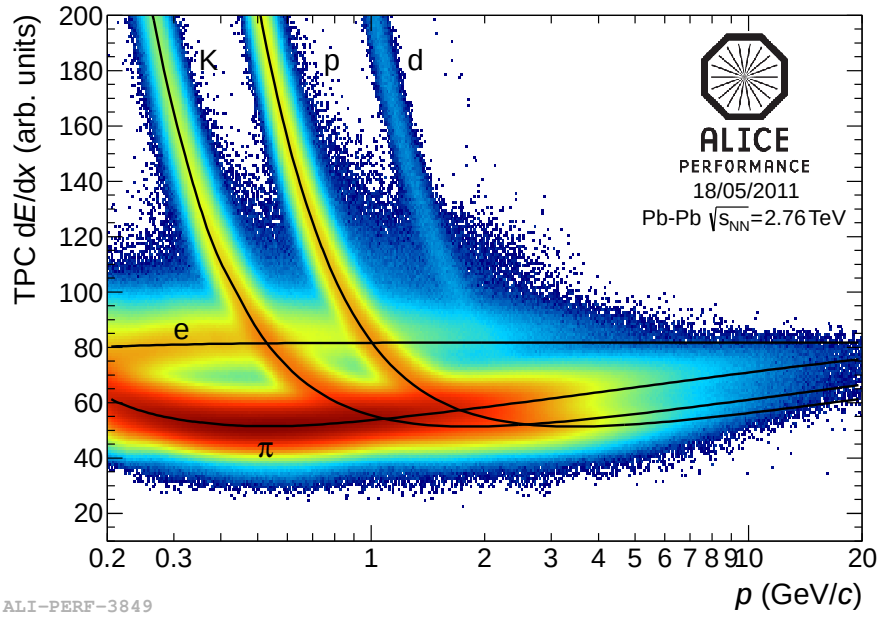

Fig. 3.3: dE/dx as a function of momentum measured with the TPC in Pb-Pb collisions at $\sqrt{s}$ = 2.76 TeV. The solid lines correspond to the calculated value of the Bethe-Bloch parametrization.

3.3 TOF PID

TOF detector identifies particles using their time of flight, *i.e.* the time the particle travels from the primary vertex to the TOF sensible pad. The starting sample for the TOF signal consist of all TPC tracks which can be extrapolated from the TPC outer wall to the

[1] ALEPH is one of the experiments in the Large Electron Positron collider (LEP) that worked at CERN during the period 1989-2000.

TOF inner radius (R $\approx$ 3.7 m). After this extrapolation, the tracks are ordered according their curvature, so that matching procedure is first applied to the highest momentum tracks. The ordering in momentum contributes to reducing the contamination from fakes associations. In the matching process, each track is extrapolated through the TOF detector, until its extrapolation traverses one of the preselected TOF pads, then the time signal on this pad is associated to the track. In case the track did not fall within the active area of the pads, a looser criterion is applied selecting the time signal closest to the track trajectory. Once a time signal is assigned to a track it is flagged to prevent fake associations to other tracks.

With the tracks with a matching TOF signal, the PID procedure can be applied. In Fig 3.4 the velocity ($\beta = v/c$) of particles, defined as: $L/(ct_{TOF})$ [2] is shown as a function of the momentum of the particle. The separation bands for pions, kaons and protons are evident.

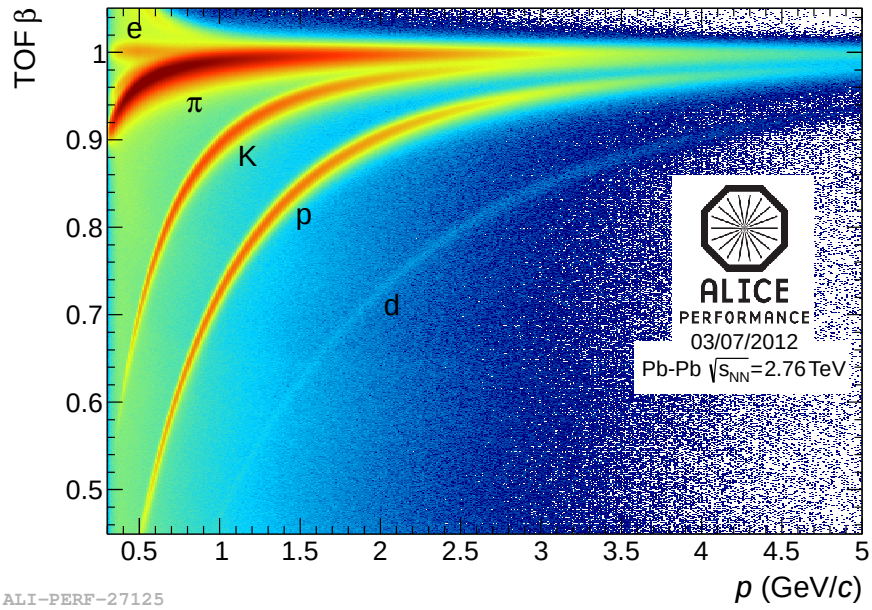

Fig. 3.4: Velocity as a function of momentum measured with the TOF in Pb-Pb collisions at $\sqrt{s}$ = 2.76 TeV. The points outside the bands corresponds to the background due to the mismatch in Pb-Pb collisions.

3.4 HMPID PID

The charged particles in the HMPID flow the formula of a Cherenkov detector, with refraction index n = 1.289 (λ = 175 nm). The Fig 3.5 shows the theoretical curve for the HMPID and the Cherenkov angle obtained as a function of momentum for all track reconstructed with HMPID. The momentum is obtained from the curvature and the helix

[2] Where L is the track length and c the speed of light.

made by the track due to the magnetic field. The velocity β, is obtained from θ_{Ch} once the momentum is known.

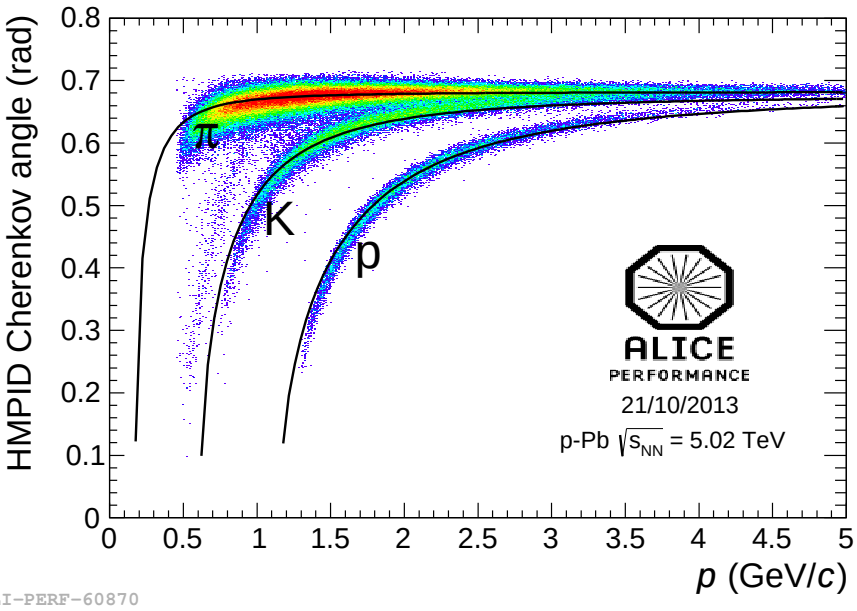

Fig. 3.5: θ_{Ch} as a function of momentum for pions, kaons, and protons measured with the HMPID in p-Pb collisions at $\sqrt{s_{NN}}$ = 5.02 TeV.

4

Results: $\pi^{\pm}$, $\mathrm{K}^{\pm}$, p and $\bar{\mathrm{p}}$ transverse momentum spectra in pp collisions

The measurement of transverse momentum spectra is of fundamental interest in hadronic collisions. The information obtained from the spectra in pp collisions provides very important benchmark to understand the behavior of the hadron production in Pb−Pb collisions. In Pb−Pb the spectra at low p_{T} is sensitive to mass effects related generally to flow while at high p_{T} the particle spectra is sensitive to the jet quenching, the particle identification can allow us to learn how the medium affects the particle composition.

4.1 Event selection

The events used in this analysis were selected using the class: *AliPhysicsSelection*, which selects events according to the ALICE triggers definitions. In this analysis the trigger used was the Minimum-Bias trigger. It is also required that the events have at least one contributor in the TPC and the primary vertex position reconstructed within a 10 cm distance from the nominal interaction point in the z axis. Data recorded during the 2010 and 2011 LHC pp runs at $\sqrt{s}$ = 0.9, 2.76 and 7 TeV were used for this analysis.

4.1.1 Minimum Bias Events

Minimum Bias (MB) is a generic term which refers to events that are selected with a "*loose*" trigger that accepts a large fraction of the inelastic cross section [25]. The MB triggers are designed to trigger on all inelastic interactions inside the detector. In ALICE the information of the detectors V0 and SPD are combined to select only events coming

from real pp collisions and to exclude interactions of the beam with the residual gas in the beam pipe. The beam-gas events are rejected using the fact that the arrival time of particles at V0A and at V0C differs from that of real pp collisions.

We define t_0 as the time when the bunches coming from opposite directions cross the nominal interaction point. Particles originating from pp collisions will arrive at the V0A (V0C) approximately 11.3 ns (3.0 ns) after t_0[13]. If the particles arrive at one of the arrays before t_0 this means they were produced by beam gas interaction behind one of the V0 arrays.

4.1.2 Track Selection

In this analysis only global tracks were [1] selected using the standard 2011 track cuts. The standard track cuts provide an accurate selection for the spectra analysis, and it has been used in previous ALICE results [17] and [18].

The standard track cuts consist in:

- At least 70 crossed rows on the TPC, and a χ^2 of the momentum fit smaller than 4 per cluster. Since each cluster in the TPC provides two degrees of freedom and the number of parameters of the track fit is much smaller than the number of clusters, the χ^2 cut is approximately 2 per degree of freedom. [17]

- At least two clusters in the ITS must be associated to the track, out of which at least one is from the SPD.

- Distance-of-closest approach (DCA_Z) to the reconstructed event vertex less than 2 cm.

- Kinks daughter rejection: This cut rejects the tracks charged kaons identified by their weak decays inside the TPC. This is done using the kinematics of kink topology measured as a secondary vertex with one mother track and one daughter track with the same charge [2]. The decay channel of kaons can be consulted in section 1.2.1.

- TPC and ITS refit:Ask for the last pass of the reconstruction to refit in the inward direction in order to get the track parameters at the vertex.

- χ^2 per ITS cluster less than 36.

[1] A global track make use of ITS, TRD, TPC and TOF information, this ensures precise information of the reconstruction like: high tracking efficiency and $\mathrm{d}E/\mathrm{d}x$ resolution. The other set of tracks that can be used in an analysis is the TPC-only tracks, which only use TPC information.

[2] The decays kinematics allows the separation between kaons from kink topology and the main source of background kinks due to the charged pion decays. This is done measuring the transverse momentum of the daughter with respect to the mother's direction, q_t. It has different values depending on the decays, a cut on q_t removes the pions decays.

4.2 TOF analysis strategy

The TOF PID strategy presented here is based on a statistical method, known as unfolding. The unfolding method was selected over the track by track method because it allows to extend the p_{T} range of PID, reaching values of p_{T} around 2.5 GeV/*c* for pions and kaons and 3.0 GeV/*c* for protons [3].

The particle identification is done as a function of p_{T} only with tracks after the track selection and the PID method used in TOF is the following: Identify the primary particles pions (π^+), antipions (π^-), kaons (K^+), antikaons (K^-), protons (p) and antiprotons ($\bar{\mathrm{p}}$) in the data sample using a statistical method based on the response function of TOF: the time of flight. These yields need to be corrected for different detector inefficiencies, which can only be done comparing the results of reconstructed particles generated by the event generators (PYTHIA). There are different types of efficiencies to consider in order to correct the p_{T} spectra. At the end the spectra has to be normalized to the number inelastic events, this takes into account the efficiencies of the event selection.

All the steps of the method used to obtain the final spectra are described in the following sections: a)Raw yield extraction from data, b)Apply efficiency correction to raw yield relying on Monte Carlo models, c) Apply feed-down correction based both on data and MC information.

4.2.1 Raw yield extraction

The PID estimator used for the raw yield extraction is the time difference Δt_i, defined as:

$$\Delta t_i = t_{TOF} - t_0 - t_{exp,i} \tag{4.1}$$

where t_{TOF} is the time-of-flight measured by the TOF detector, $t_{exp,i}$ is the expected time-of-flight for the mass hypothesis i computed in the reconstruction procedure and t_0 is the event start time.

For an ideal time of flight detector the Δt shape, in the correct mass hypothesis, is gaussian. In the case of TOF, due to residual miscalibration, the TOF signal is not purely gaussian but it is described by a function that includes a gaussian term plus an exponential tail on its right-end side.

In detail, the unfolding method applied for each mass hypothesis is the following: All the selected tracks are supposed to be of type i. With this mass hypothesis the rapidity is calculated and only tracks with $|y_i| < 0.5$ are accepted. The rapidity y_i of identified particles is computed with

[3] For the 900 GeV analysis the p_{T} reach is smaller compared to the higher energies just because of the statistics of the data sample.

$$y_i = \operatorname{arcsin} h \frac{\sqrt{p^2 - p_T^2}}{\sqrt{m_T^2 + p_T^2}} \tag{4.2}$$

Then the Δt_i distribution is computed for each p_{T} interval. It is evident that the mass hypothesis, i, is correct only for some tracks, hence the Δt_i distribution is composed by three sub-samples, one for each particles species. The sub-sample centered at zero corresponds to the tracks of the species i for which the mass hypothesis is correct (signal), the others are due to the particles of species $j \neq i$ (background 1) and due to the particles of type $k \neq i$ (background 2) where e.g. i are pions, j are kaons and k are protons.

The Fig. 4.1, 4.2 and 4.3 show the Δt_π, Δt_K and Δt_p as a function of p_{T} , for the pions, kaons and protons respectively. The color on the plots corresponds to a third axis value that indicates the number of tracks. The yield extraction is performed in different p_{T} bins. This means that several p_{T} cuts are performed on Fig 4.1,4.2 and 4.3 and then a projection to the Δt is performed. This generates a distribution composed by 3 contributions, each of these contributions correspond to a different particle species for several p_{T} bins.

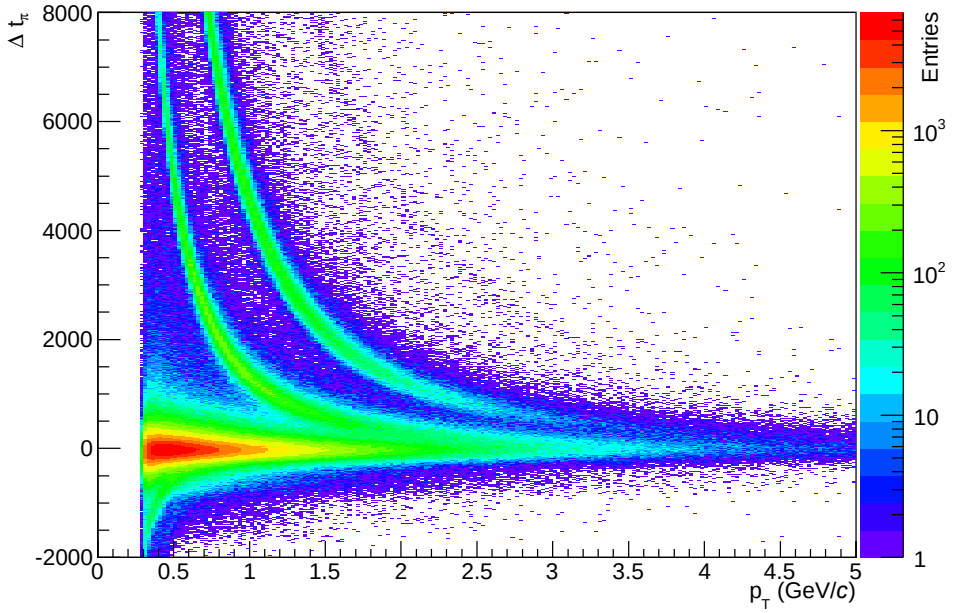

Fig. 4.1: Δt_π distribution. The distribution centered at zero corresponds to pions positive and negative. The other bands corresponds to the kaons and protons background.

In each p_{T} bin, the Δt_i is fitted with function composed by 3 gaussian each gaussian with an exponential tail on the right side. The procedure is repeated 6 times: for pions $\pm$, kaons $\pm$, protons and antiprotons.

The plots in Fig. 4.4, 4.5, and 4.6 show an example of the fits using the 3 different mass hypothesis for pp collisions at $\sqrt{s}$ = 2.76 GeV.

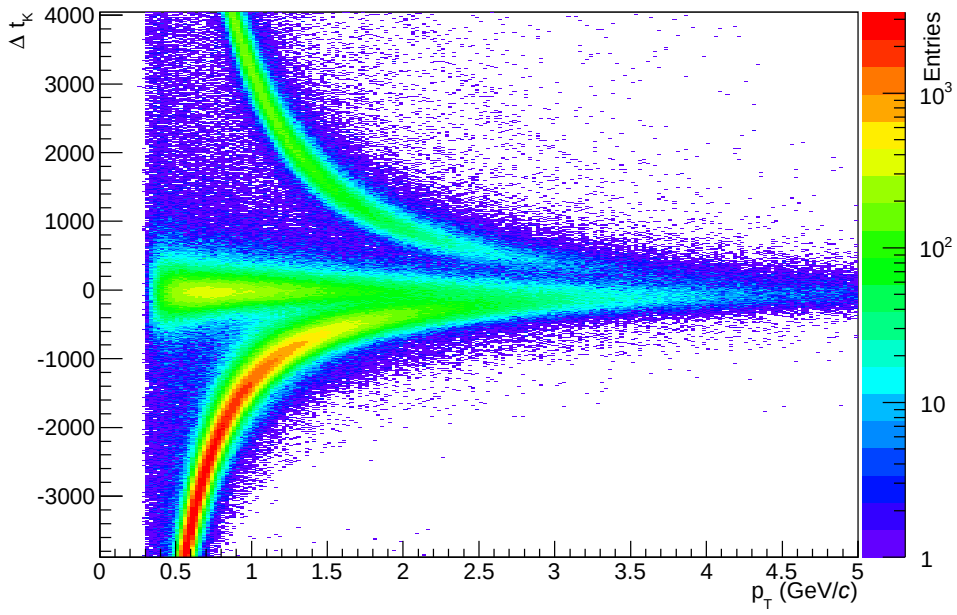

Fig. 4.2: Δt_K distribution. The distribution centered at zero corresponds to kaons positive and negative. The other bands corresponds to the pions and protons background.

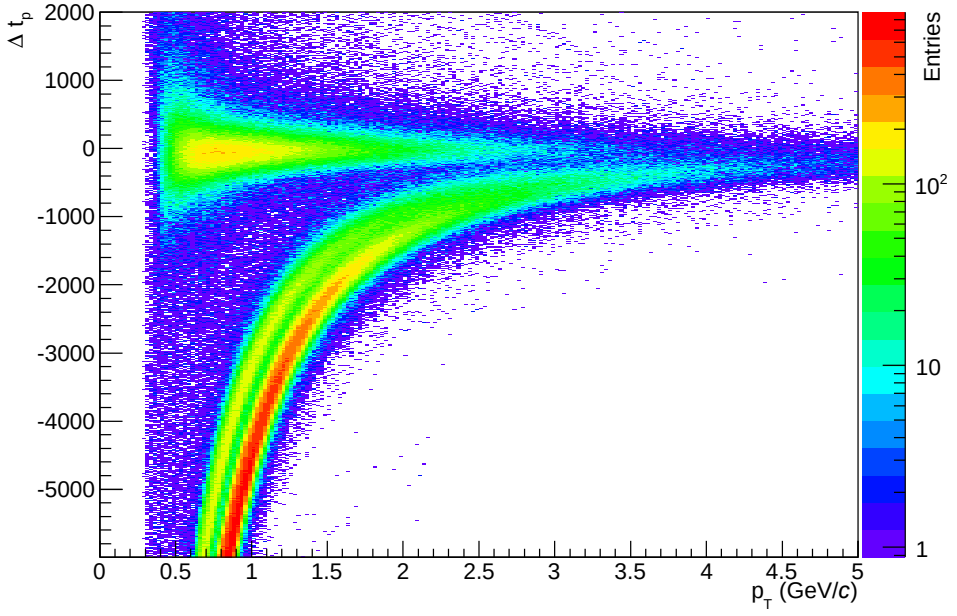

Fig. 4.3: Δt_p distribution. The distribution centered at zero corresponds to protons positive and negative. The other bands corresponds to the pions and kaons background.

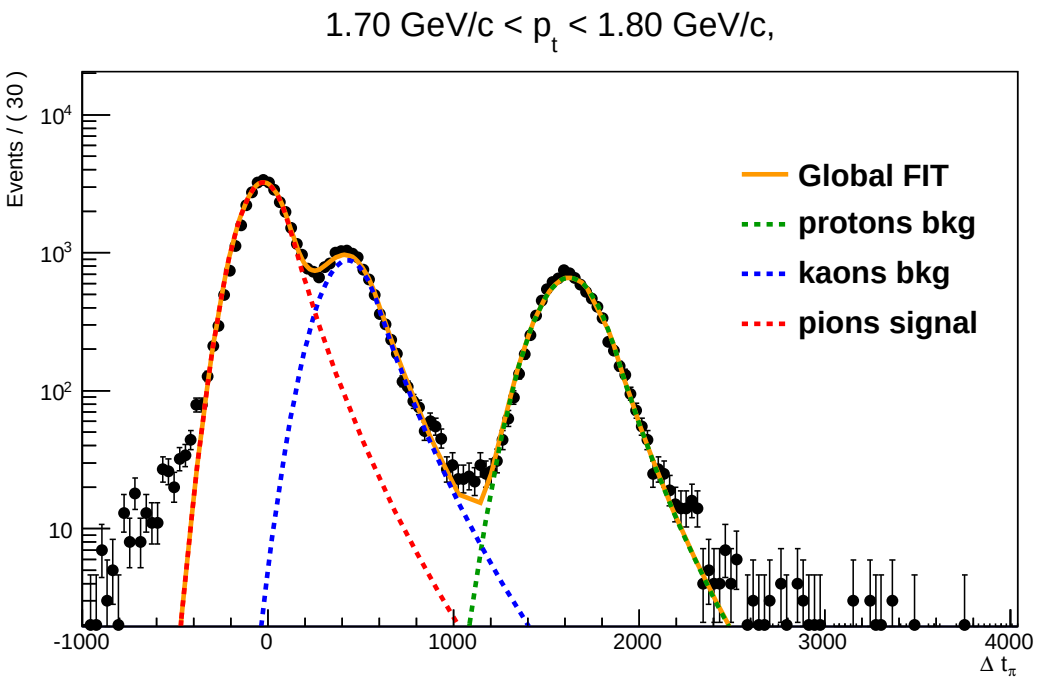

Fig. 4.4: Fit example for the pion signal (red), kaon background (green) and proton background (blue). The global fit (orange) to the data points is the sum of the signal and the background.

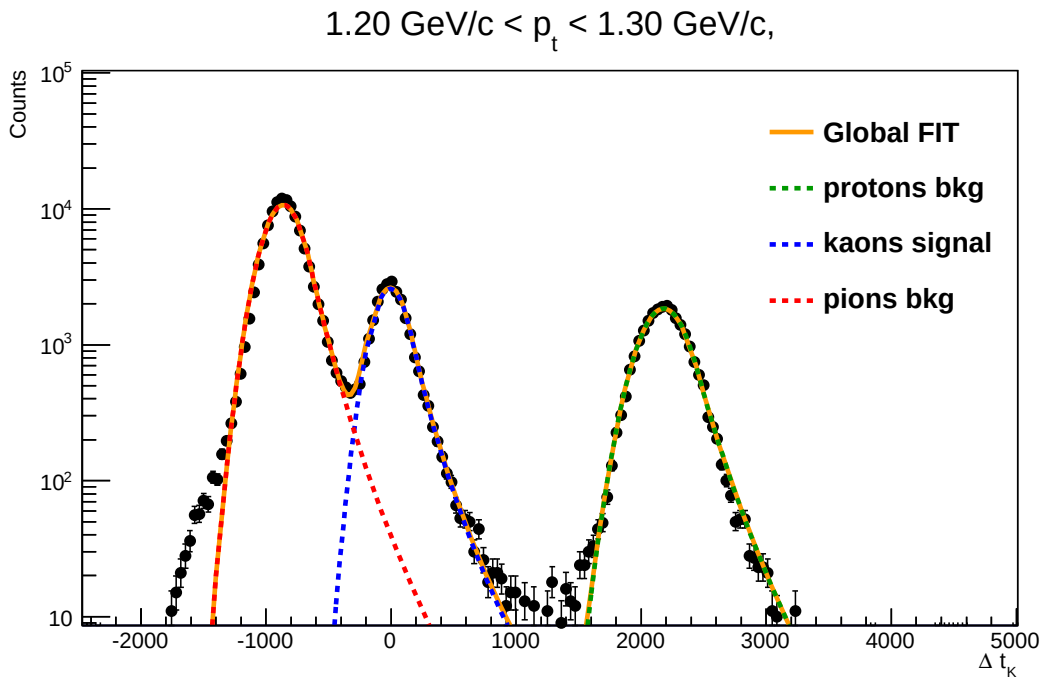

Fig. 4.5: Fit example for the kaon signal (green), pion background (red) and proton background (blue). The global fit (orange) to the data points is the sum of the signal and the background.

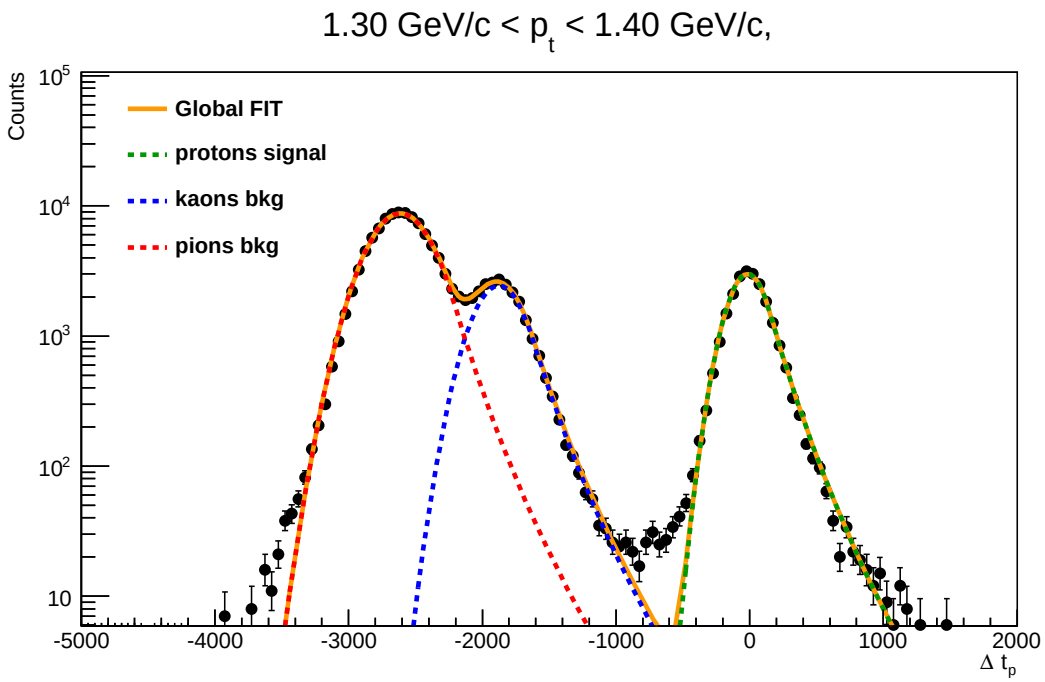

Fig. 4.6: Fit example for the proton signal (blue), kaon background (green) and pion background (red). The global fit (orange) to the data points is the sum of the signal and the background.

The integral extracted from the signal fit function in each p_{T} bin is called raw yield. The integrals of the global fit are constrained to be between zero and the total number of analyzed tracks. As we mentioned earlier, the distributions are composed of 3 subsamples: 1 signal and 2 backgrounds. The parameters to fit in each sub-sample are 4; 2 parameters come from the gaussian part: the *mean*, and the *sigma*. And 2 parameters come from the exponential part: the *tail* (the point where the exponential start to contribute), and the *slope* of the exponential.

The parameters are set free in the low p_{T} part, where the separation between species is very good. However, for the high p_{T} part the parameters are allowed to vary within very loss bounds, fixing the saturation values at high p_{T} . After that, a function is fitted to the parameters (mean and sigma) for the signal and the background. Finally, the fit to the Δt_i distributions is performed again evaluating this function in each p_{T} bin allowing to vary within very loose bounds in all the p_{T} range.

4.2.2 Efficiency corrections

To obtain the final spectra, several efficiency corrections need to be take into account. The efficiency corrections consist in determine the quantity of real particles produced in the collisions [4]; this obtained based on the event generators. The method consist in applying exactly the same analysis procedure through the whole cycle (see section 2.2.1) to the events generated and the events coming from real data. The next step is to compare the Monte Carlo generated results, to the real reconstructed data. In this way the detector performance is evaluated. All the corrections applied are denominated as efficiency corrections.

The efficiency corrections are a track level correction which are factorized in 4 different parts, all of them are p_{T} dependent

$$Eff_{\mathrm{Total}} = Eff_{\mathrm{Track}} \times Eff_{\mathrm{Match}} \times Eff_{\mathrm{Vtx}} \tag{4.3}$$

Tracking efficiency

The tracking efficiency, Eff_{Track}, is evaluated using Monte Carlo simulations. This correction takes into account the fact that not all the primary particles can be reconstructed by the TPC. (see Section 2.2.2). It is defined for all the tracks after Minimum Bias trigger and the Vertex Selection as:

$$Eff_{\mathrm{Track}} = \frac{(PhysicalPrimary+ \mid \eta \mid < 0.9+ \mid y \mid < 0.5)_{REC}}{(PhysicalPrimary+ \mid \eta \mid < 0.9+ \mid y \mid < 0.5)_{GEN}} \tag{4.4}$$

[4]The number of particles reconstructed by our detectors are only a part of the real number of particles produced in the collisions, some of them are lost due to the detector acceptance, detector dead zones, noisy channels in the detector, etc.

This means the fraction of primary (Physical Primary) reconstructed tracks over the generated primary particles in the same rapidity window. The tracking efficiency depends of the particle species. The results obtained for each particle species and charge are shown in Fig. 4.7.

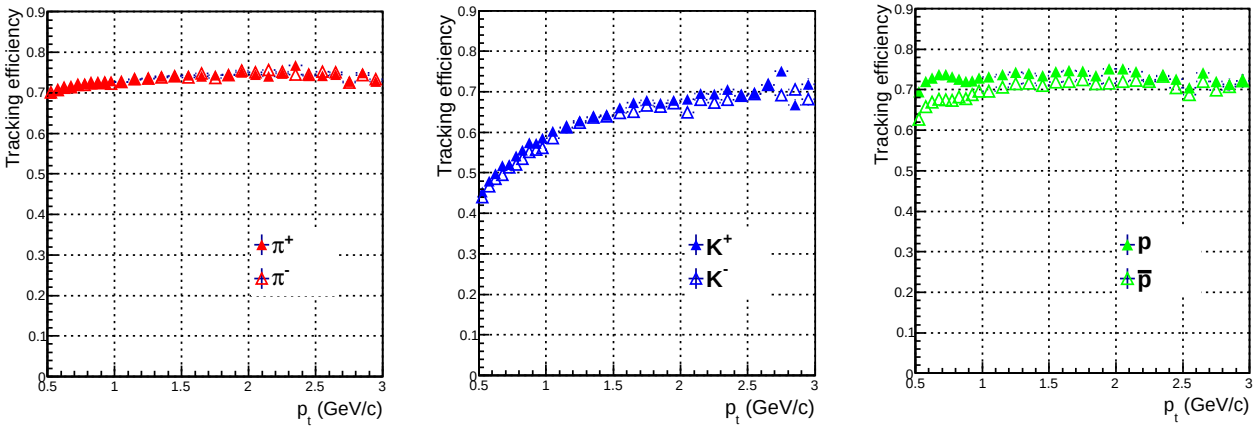

Fig. 4.7: Tracking efficiency in pp collisions at $\sqrt{s}$ = 2.76 TeV. From left to right: pions, kaons and protons.

Matching efficiency

The matching efficiency, Eff_{Match}, is evaluated using Monte Carlo simulations. This correction takes into account the fact that not all the global reconstructed tracks are reconstructed by TOF. The matching efficiency is defined for all the tracks after Minimum Bias trigger and the Vertex Selection as:

$$Eff_{\mathrm{Match}} = \frac{(StandardTrackCuts + TOF_{out} + TOF_{time} + \mid \eta \mid < 0.9 + \mid y \mid < 0.5)_{REC}}{(StandardTrackCuts + \mid \eta \mid < 0.9 + \mid y \mid < 0.5)_{REC}} \tag{4.5}$$

This means the fraction of primary tracks satisfactorily matched with a TOF signal over the reconstructed primary tracks in the same rapidity window. The results obtained for each particle species and charge are shown in Fig 4.8.

The matching efficiency depends on the fraction of tracks lost during the propagation from the TPC to TOF due to the geometrical acceptance, weak decays and the interactions with the material. In addition, it includes the probability to match a track reaching the TOF with a TOF hit. This cuts are necessary for the TOF tracks are denoted as TOF_{out} and TOF_{time}.

Due to the presence of the magnetic field which deflects the charged particles, the Eff_{Match} at p_{T} < 0.5 GeV/c drops quickly and a little variation in the track momenta can cause a significant variation. To minimize the sensitivity of the analysis to imperfections in the simulation of the matching efficiency and to the uncertainty induced on the corresponding correction, only tracks with p_{T} > 0.5 GeV/c were considered for the TOF analysis.

In the case of protons, the p_{T} spectra are reported starting from p_{T} = 0.8 GeV/c since, below this threshold, the estimated time, $t_{exp,p}$, suffers imperfections in the correction factors due to the energy loss in the material. This causes the signal distribution to be unsatisfactorily described by the fit function used in the procedure, and the result of the interpolation may be not reliable.

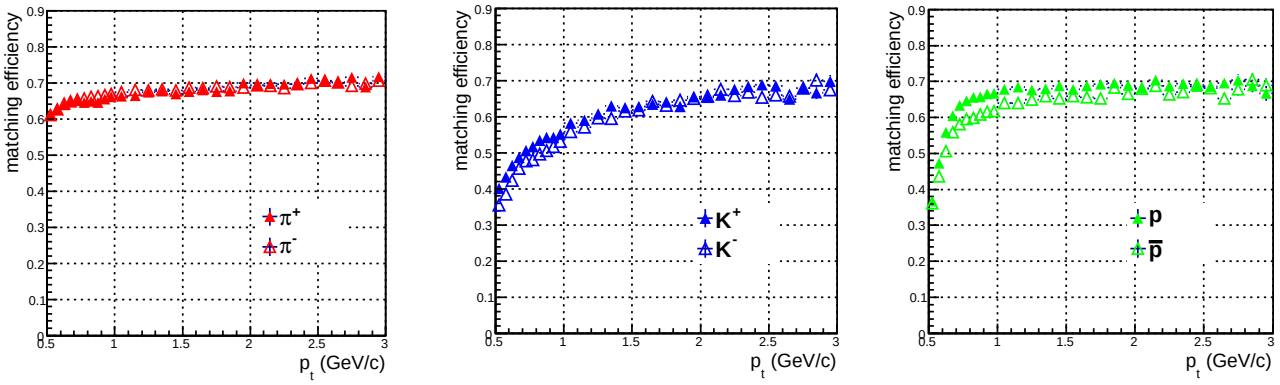

Fig. 4.8: TOF matching efficiency in pp collisions at $\sqrt{s}$ = 2.76 TeV. From left to right: pions, kaons and protons.

GEANT/FLUKA correction

An extra correction is applied to the tracking and matching efficiency. This is usually known as *GEANT/FLUKA correction* [5]. This correction takes into account that the cross sections for antiprotons and negative kaons are not well reproduced in the transport code GEANT 3. As the transport code FLUKA provides an accurate description, the comparison between GEANT 3 and FLUKA provides a correction factor that need to be applied to the efficiencies terms. It is important to mention that the latest version of GEANT 3 used only for the 2.76 TeV analysis has been patched for the antiproton cross section, so that the correction for this data sample was only applied to the negative kaons. The Fig. 4.9 shows the GEANT/FLUKA correction that has to be multiplied for the tracking and for the matching efficiency.

Vertex efficiency

The vertex efficiency, Eff_{Vtx}, is evaluated using Monte Carlo simulations. The vertex efficiency is defined as:

$$Eff_{Vtx} = \frac{(PhysicalPrimary+ \mid \eta \mid < 0.9+ \mid y \mid < 0.5) \rightarrow after(MB+ \mid Vtx_z \mid < 10cm))}{((PhysicalPrimary+ \mid \eta \mid < 0.9+ \mid y \mid < 0.5) \rightarrow after(MB))} \quad (4.6)$$

[5] See section 2.2.4 for a more detailed description of the transport code: GEANT3 and FLUKA.

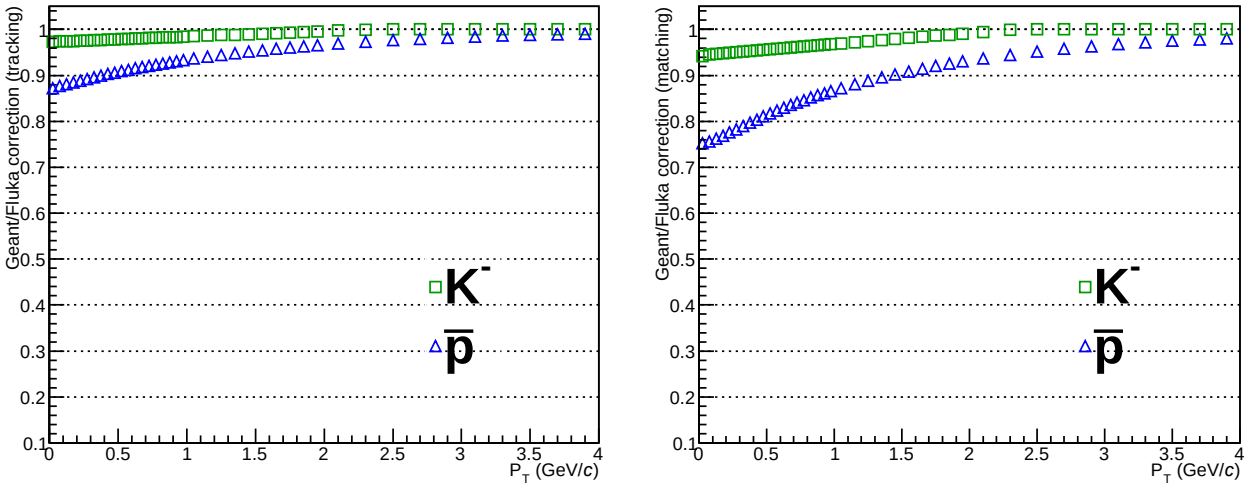

Fig. 4.9: GEANT/FLUKA correction for antikaons and antiprotons. *Left*:Correction applied to the tracking efficiency. *Right*:Correction applied to the matching efficiency.

It represents the ratio of the generated tracks in events with vertex reconstructed and vertex$_z$ $<$ 10 cm over the generated track in events after the minimum bias trigger selection. The vertex efficiency for pp collisions at $\sqrt{s}$ = 0.9 TeV is shown in Fig. 4.10. The value for $\sqrt{s}$ = 2.76 TeV is 0.945, and for $\sqrt{s}$ = 7.0 TeV is 0.99.

Note that the full correction Eff_{Total} is: reconstructed tracks with vertex reconstructed and |Vtx$_z$ |$<$ 10 cm / generated tracks in all events.

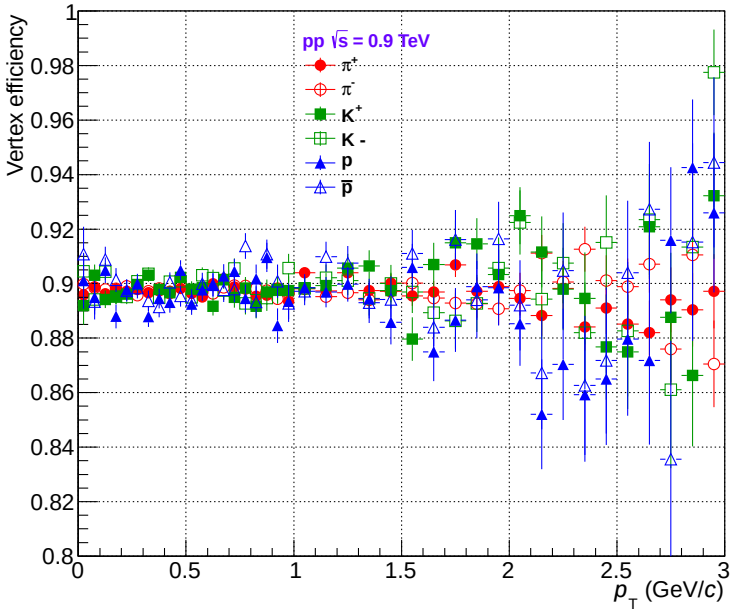

Fig. 4.10: Vertex efficiency for all particle species for pp collisions at $\sqrt{s}$ = 0.9 TeV. The vertex efficiency is taken constant for all species.

Trigger efficiency

The trigger efficiency, Eff_{trigger}, comes from an ALICE paper [31] , which reports the cross sections in pp collisions. The values for the three energies were obtained from the ALICE simulation, using the adjusted PYTHIA6 and PHOJET event generators [31]. The table 4.1 shows the values of the MB_{OR} trigger efficiency for the 3 energies. It is important to mention that this efficiency is obtained at event level; unlike the other efficiency which were obtained at track level.

$\sqrt{s}$ (TeV)	MB_{OR} (%)
0.9	$91.0^{+3.2}_{-1.0}$
2.76	$88.1^{+5.9}_{-3.5}$
7.0	$85.2^{+6.2}_{-3.0}$

Table 4.1: MB_{OR} trigger efficiencies obtained from adjusted Monte Carlo simulations. [31]

4.3 Feed-down correction

The results presented here correspond to **primary particles** [6] produced in the collision. Since strangeness production is typically underestimated in the existent event generators, and the interaction of low p_T particles with the material are not perfectly modeled in the transport code, the contamination from this two sources was extracted from the data sample.

The method to obtain the correct fraction on primary particles, *FractionPrim*, consist in fitting the transverse distance of closest approach to the vertex (DCA_{XY}) distributions of the selected tracks for the analysis with three distributions corresponding to the expected shapes for primary particles, secondary particles from weak decays or secondary particles [7] from material knock out particles [8] extracted from Monte Carlo. This distributions will be denoted as *templates* in the following. Each template is obtained from each of this contributions for each species. This is done for Monte Carlo and data in several p_{T} bins. In the Monte Carlo the type of particle is known while in the data we trust on our particle identification done track by track using an exclusive 3 σ_{TOF} [9] cut method.

[6] **Primary particles** are defined as all the particles produced in the collision including all decay products, except products from weak decays of strange particles such as K^0_s and Λ and of muons. This definition is used since in the simulation these are the final-state particles created by the Monte Carlo generators, which are then propagated (and decayed) in the subsequent detector simulation.

[7] A **secondary particle from weak decay** is a daughter particle from a weak decay of a light hadron (See section 1.2.1) or of a muon.

[8] All particles, which are neither primaries nor secondaries from weak decays, are considered as **secondaries from material**.

[9] The exclusive 3 σ_{TOF} consists in evaluate the Δt_i distributions as a function of p_{T} . If a 3 σ cut is applied, in protons for instance, this means that the selection is applied on all the track inside 3 σ from the mean value of the Δt_{p} and outside 3 σ from the Δt_{K}, and Δt_{π} mean value. With this method the contamination is practically negligible.

The procedure to establish the primary fraction from data is the following: The total number of tracks in data are constrained to the total number of entries. In the Monte Carlo simulation three DCA_{XY} templates distributions are obtained for each particle species: the primary particles, the weak decay daughters and products of interaction with the material. This distributions are showed on the left panel of Fig. 4.12. The method is based on the ROOT class *TFractionFitter* described in [28]. This class calculate the relative contributions for each template to the data distributions. The fit to the data is shown on right side of Fig 4.11 and 4.12 for pions and protons respectively.

The example of the DCA fit shown on Fig. 4.12 shows three contributions with differ in shape substantially. The primary particles distribution represents the resolution of the DCA_{XY} . The secondary particles from weak decays show a wider distribution due to the large $c\tau$ of weakly decaying particles. The contamination of particles from material is flat in the case of protons and negligible in the case of antiprotons. There is no feed-down correction applied to the kaons because its distribution is almost entirely composed of primary particles [18].

The Fig. 4.13 show the fraction of primary particles obtained as a function of p_{T} for pions, antipions, protons and antiprotons from the Monte Carlo templates of weak decays and secondary particles and pp collisions at $\sqrt{s}$ = 900 GeV data.

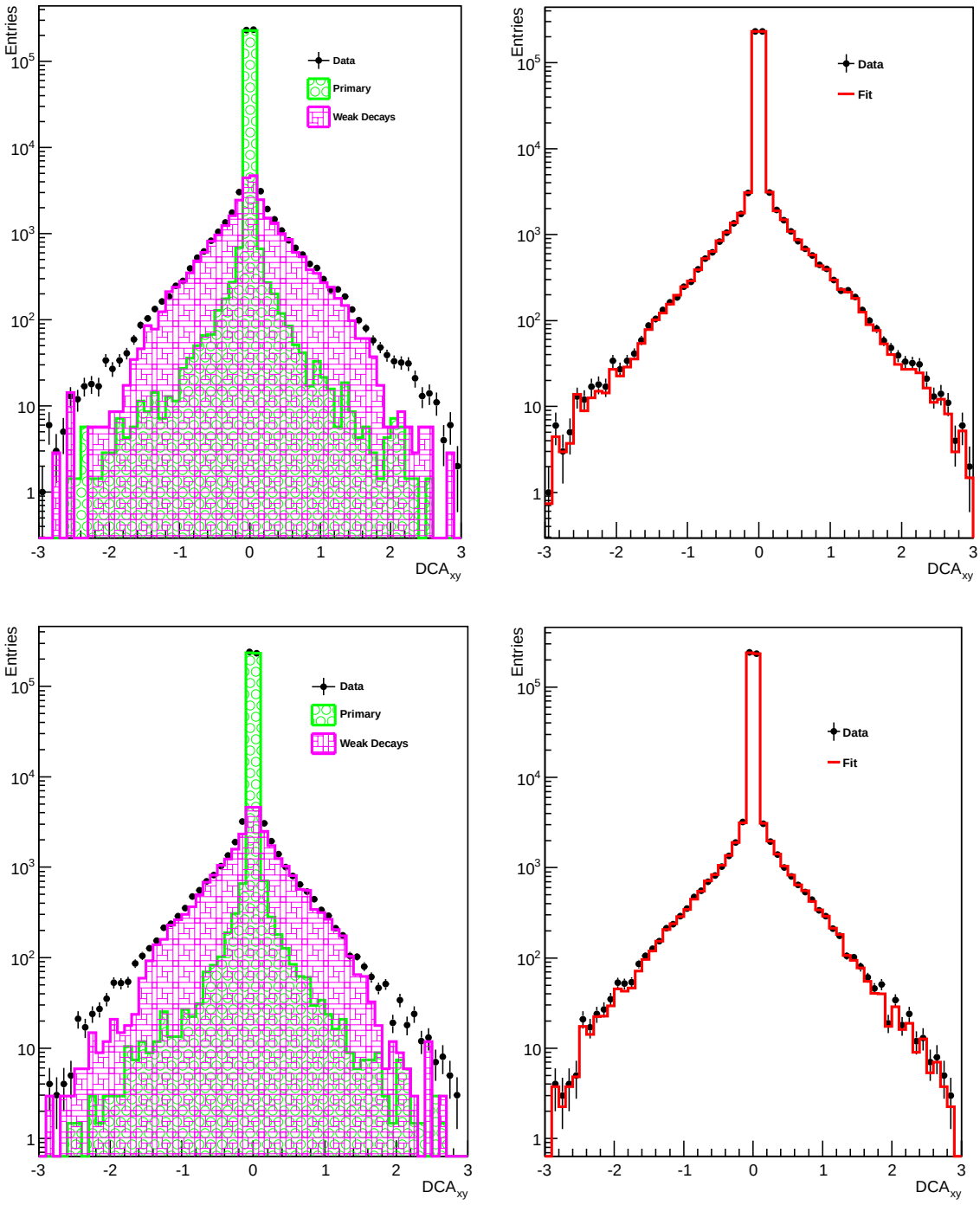

Fig. 4.11: Example of DCA_{XY} fit for pions (top) and antipions (bottom) in the p_T region 0.65 to 0.70 GeV/*c* used to estimate the fraction of primary particles. *Left*: The black points correspond to the DCA_{XY} distribution for pions selected with a 3 σ cut. The total proton production in the data is a mixture of primary, weak decays pions. The green template corresponds to primary protons, the pink template correspond to protons produced via weak decays. In this case there is no material pions. *Right*: Fit of the sum of the contributions extracted from the templates to the data.

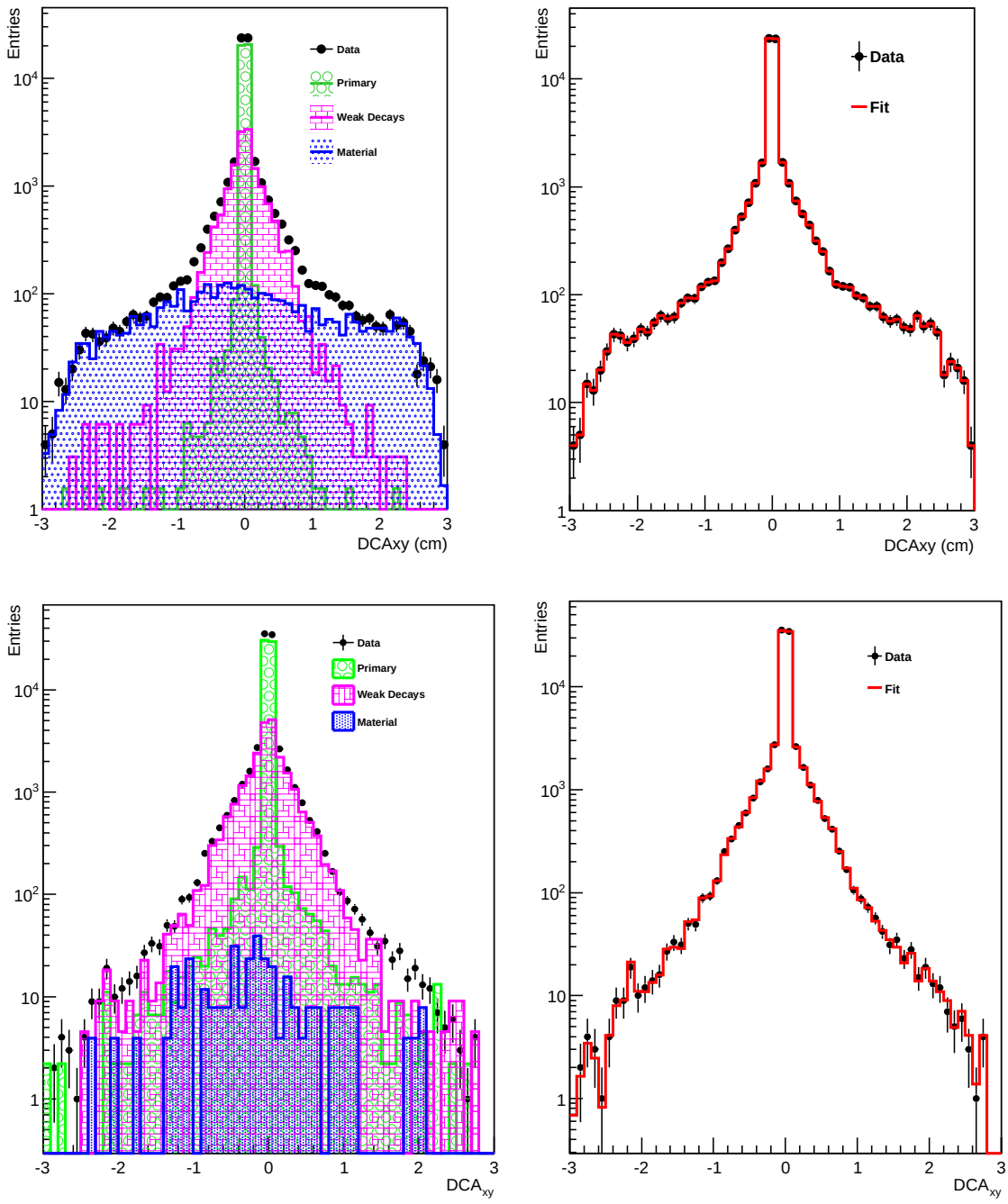

Fig. 4.12: Example of DCA$_{XY}$ fit for protons (top) and antiprotons (bottom) in the p_{T} region 0.8 to 0.85 GeV/c used to estimate the fraction of primary particles. *Left*: The black points correspond to the DCA$_{XY}$ distribution for protons selected with a 3 σ cut. The total proton production in the data is a mixture of primary, weak decays and material protons. The green template corresponds to primary protons, the pink template correspond to protons produced via weak decays and the blue template correspond to material protons. *Right*: Fit of the sum of the contributions extracted from the templates to the data.

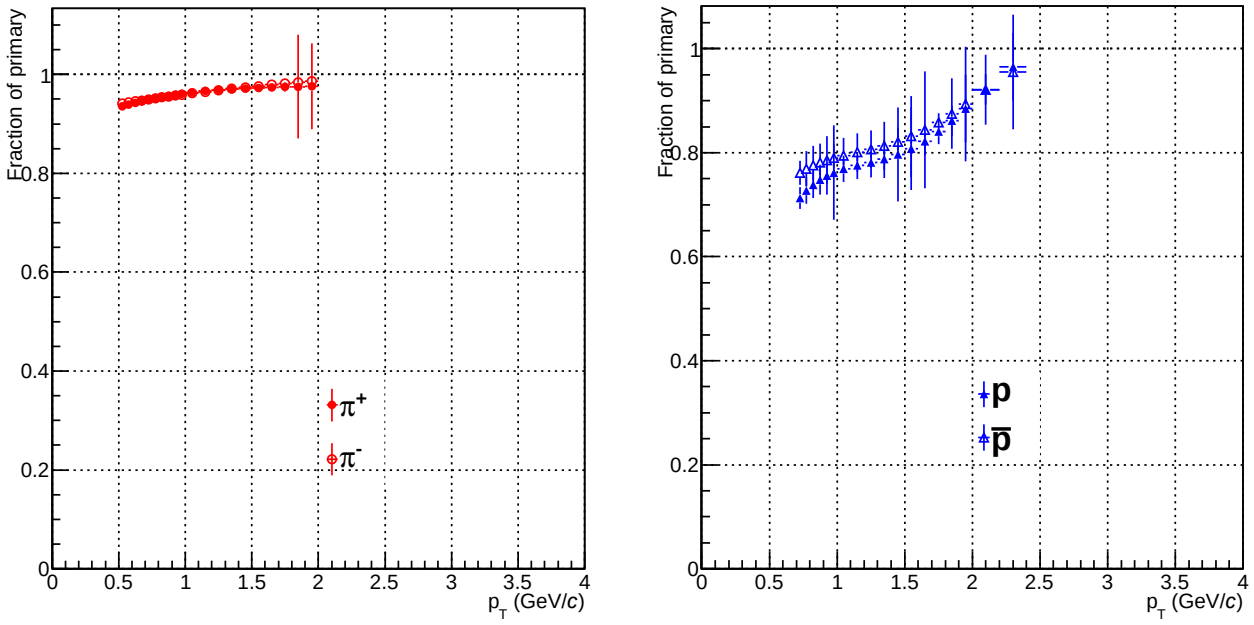

Fig. 4.13: Fraction of primary particles obtained as a function of p_{T} . *Left*: Primary fraction of pions and antipions. *Right*: Primary fraction of protons and antiprotons.

4.4 Systematic uncertainties

The systematic effects following Orear's definition are "a general category which includes effects such as background, selection bias, scanning efficiency, energy resolution, angle resolution, variation of counter efficiency with beam position, and energy, dead time, etc. The uncertainty in the estimation of such systematic effect is called systematic error". [29]. The systematic errors and the systematic uncertainties are treated as synonyms in this text [10]. However according to Barlow [30] the term *systematic error* should be replaced by *systematic uncertainy* only in an irrealistic ideal world.

The different sources of systematic uncertainties in the PID analysis discussed here come from 3 main sources: The PID method, the tracking efficiency, the matching efficiency.

4.4.1 PID method

Due to the unfolding method, a systematic uncertainty could arise from the selection of the parameters of the fit. For this reason the parameters are shifted $\pm$ 10% respect to the standard value. For the signal the parameters varied are the σ, the mean, and the slope of the exponential tail with respect to the standard value. For the background the parameters varied are only the σ and the slope since the change in the mean of 10% of

[10] One should have in mind the existence of the *systematic mistakes* which result form neglecting the systematic effects.

the background produce an unsatisfactory fit and a minor variation produces negligible changes on the raw yield. In Fig. 4.14 and Fig. 4.15 the ratios of varying the signal and the background respect to the standard spectra are showed respectively.

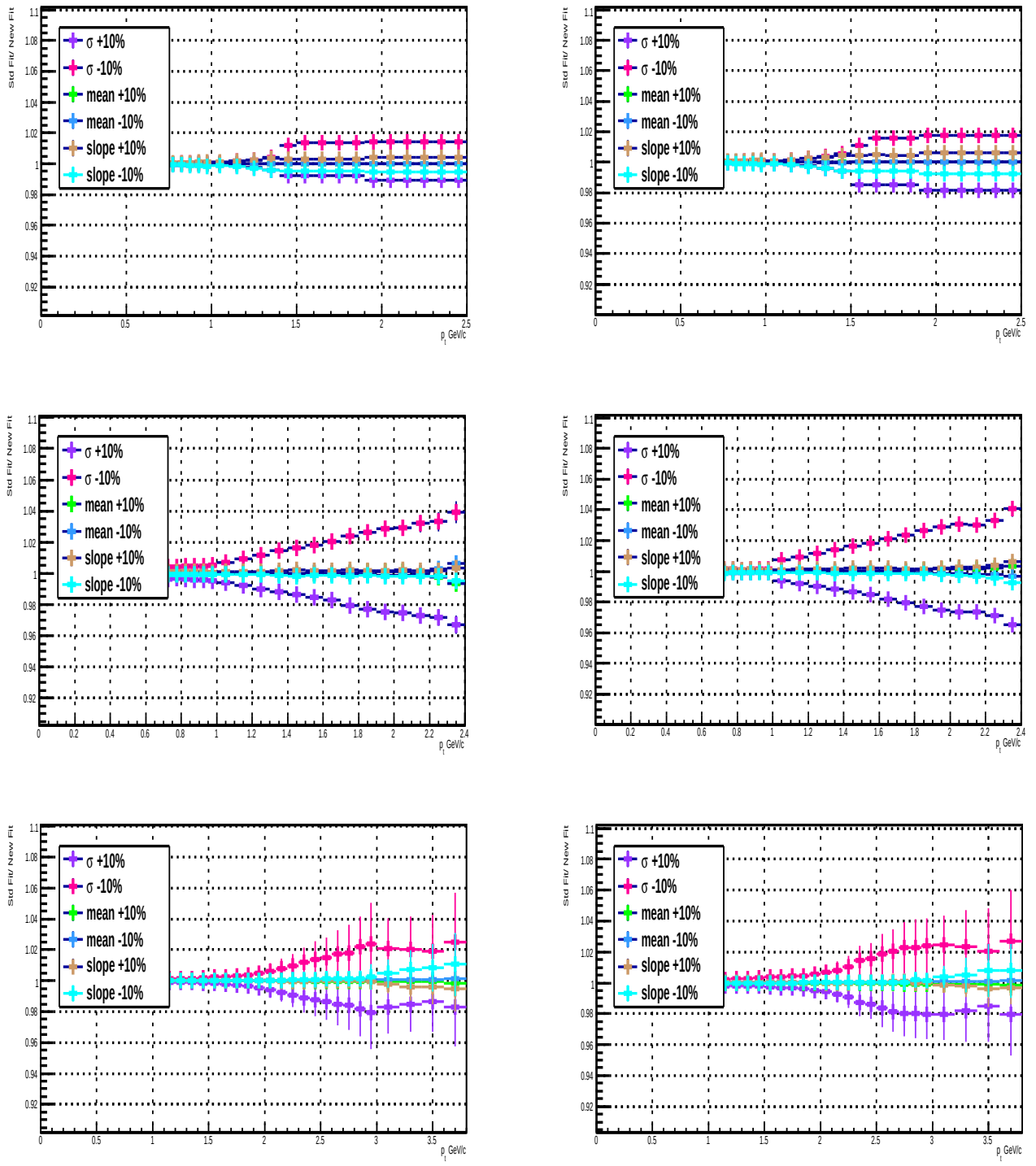

Fig. 4.14: Ratios between the spectra obtained changing the fit parameters of the signal and the standard ones for: pions(top) , kaons (middle) and protons (bottom). Positive particles are shown in the left panel while negative particles are shown in the right panel.

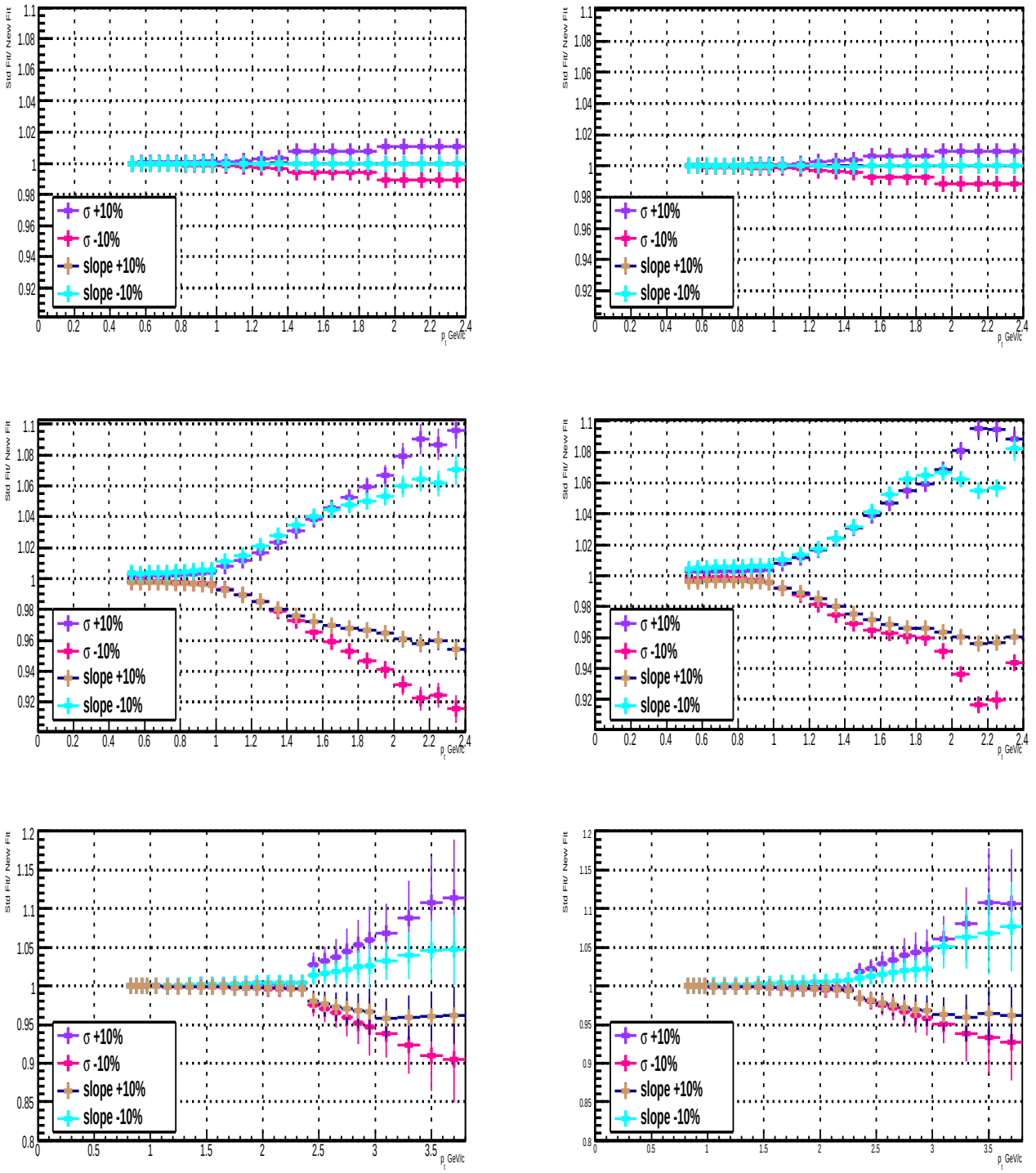

Fig. 4.15: Ratios between the spectra obtained changing the fit parameters of the background and the standard ones for: pions(top) , kaons (middle) and protons (bottom). Positive particles are shown in the left panel while negative particles are shown in the right panel.

4.4.2 Tracking and matching efficiency

The uncertainty in the **global tracking efficiency** was estimated comparing the track matching efficiency from TPC to ITS and from ITS to TPC in data and Monte Carlo in previous ALICE analysis [18]. As this correction is for all the global tracks, it does not depend of the species. The effect is found to be 4%. This correction takes into account the residual imperfections in the description of the ITS detector modules and dead areas.

The **TOF matching efficiency** has been tested with data in previous ALICE analysis [17]. The method consists in using the energy loss in the TPC to cleanly identify the particles. The values of deviations between data matching and Monte-Carlo simulations observed in the case of pions is 3%, for kaons 6% and for protons 4%. The values are just added as constant systematic errors for each species.

The Fig. 4.16 shows the total systematic uncertainties used for the TOF spectra, the main contribution comes form the PID method. To the total systematics still need to be added the constant values as a function of p_{T} that comes from tracking and matching.

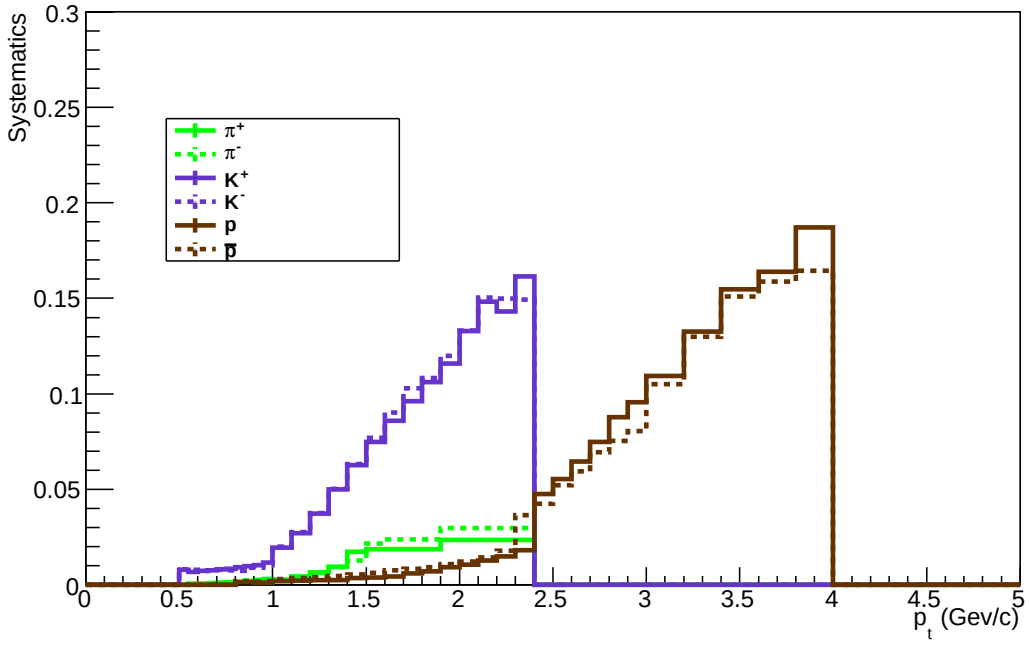

Fig. 4.16: Total systematic uncertainties used for the TOF spectra alone.

As it has been found that the propagation of the systematics in the spectra and the particle ratios are not completely uncorrelated, and it was difficult to propagate, the systematics on the ratio was calculated separately. The Fig. 4.17 shows the systematic errors obtained for the particle ratios.

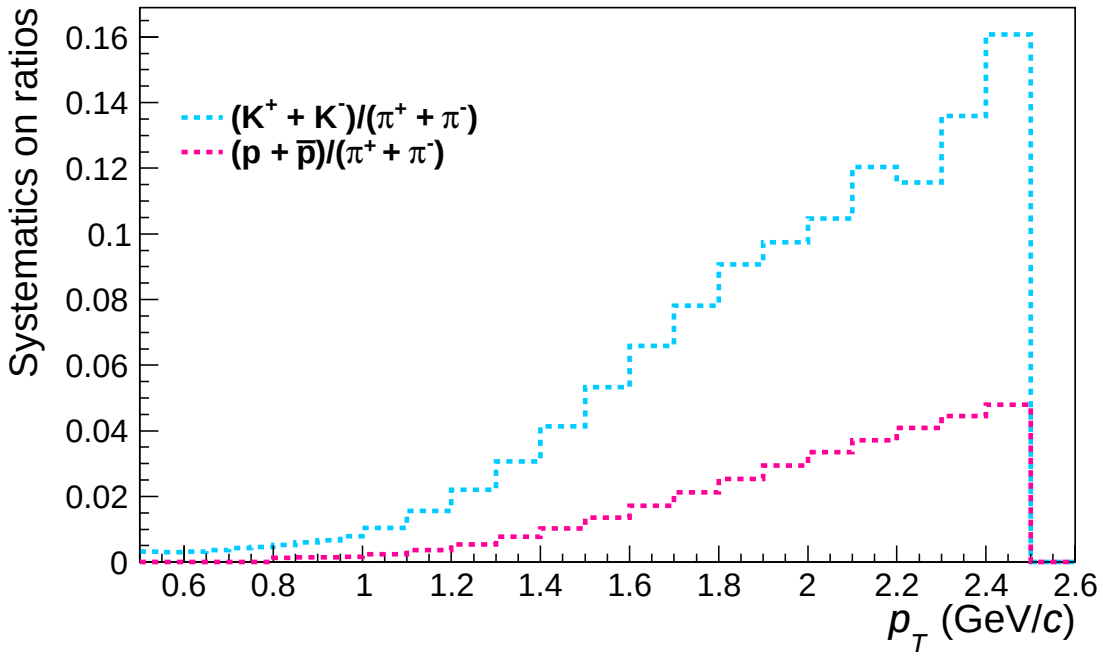

Fig. 4.17: Total systematic uncertainties used for the TOF particle ratios.

4.5 Final Spectra

To obtain the final spectra, the raw spectra have to be corrected for all the factors described below. The final spectra is normalized to N_0, which means the number of events after physic selection. N_0=N_{ev} over the Eff_{trigger}.

$$\frac{1}{N}\frac{d^2N}{dp_{\text{T}}dy} = \frac{1}{N_0} \times Raw \times \frac{1}{Eff_{\text{Match}} \times Eff_{\text{Track}} \times Eff_{\text{Vtx}}} \times FractionPrim \tag{4.7}$$

The final spectra obtained with the TOF are shown in Fig. 4.18 for pions, kaons, and protons respectively.

4.5.1 Comparison between two methods

The TOF analysis for the 2.76 TeV was also performed using a different method not performed by the author of this work. However, to crosscheck the validity of both analysis a comparison was performed. In principle, the method used is exactly the same with only one difference: the only difference was the way to take into account the presence of the exponential tail in the Δt_i distributions. In my case the tail parameter was imposed to be equal to the σ of the gaussian while in the case of the present work the tail was not equal to the σ. Since the origin of the tail is unknown there is no best functional way to take into account the presence of the exponential tail. However, once that the final

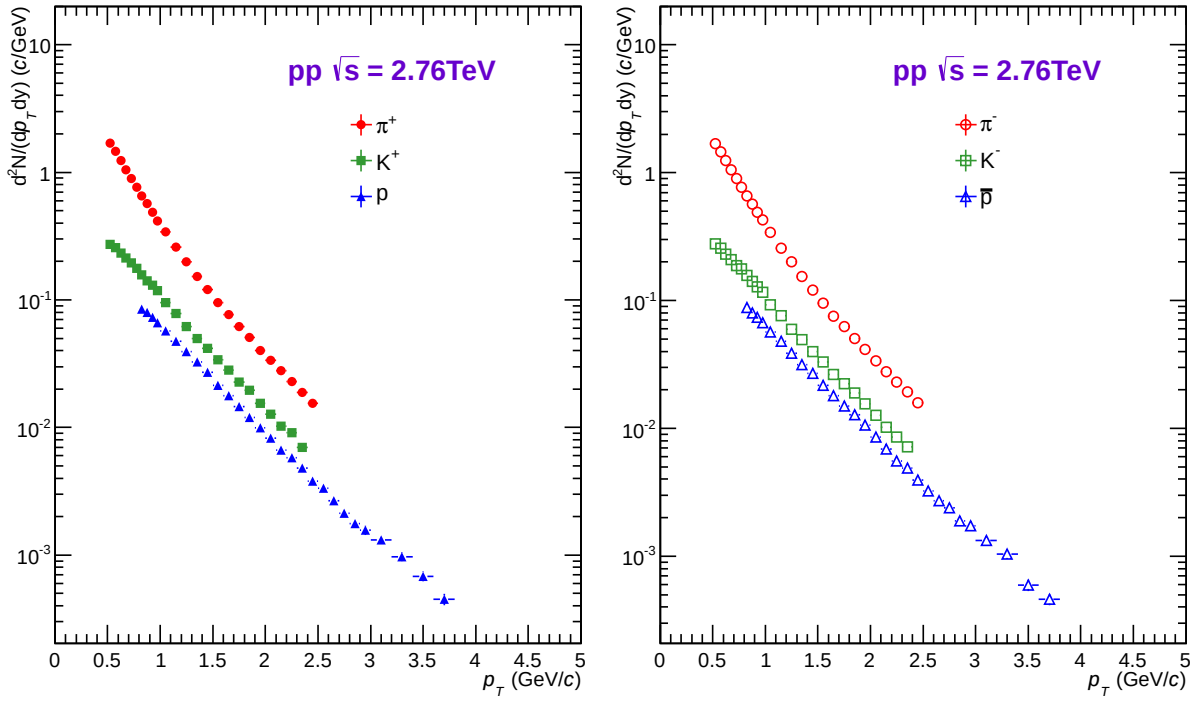

Fig. 4.18: *Left*: TOF final spectra for positive charged hadrons. *Right*: TOF final spectra for negative charged hadrons. Only statistical errors plotted.

spectra and the total systematics have been computed by both TOF analyses the results were compared.

The choice for the preliminary ALICE spectra was based on the comparison with HMPID detector at high p_{T} . However this was arbitrary since within systematic uncertainties the two analysis were perfectly equivalent.

4.6 Combining the spectra at $\sqrt{s}$ = 2.76 TeV with several detectors-

4.6.1 Combining the spectra

The full identified p_{T} spectra measured by ALICE are obtained combining the different detectors and different particle identification methods, this allows to measure the spectra in a large p_{T} range. The methods mentioned in chapter 3, measured the spectra for pions, kaons and protons. The method to combine the different results is to use a weighted mean method, using as weight the uncorrelated systematic uncertainties between the different analyses in the overlap region for the three different species. Fig. 4.19 shows the comparison for the 3 different species: pions (red), kaons (blue) and proton (green) for the TPCTOF_TOF, TPCTOF_ITSsa and HMPID_TOF analyses. Figure taken from the ALICE analysis note [26].

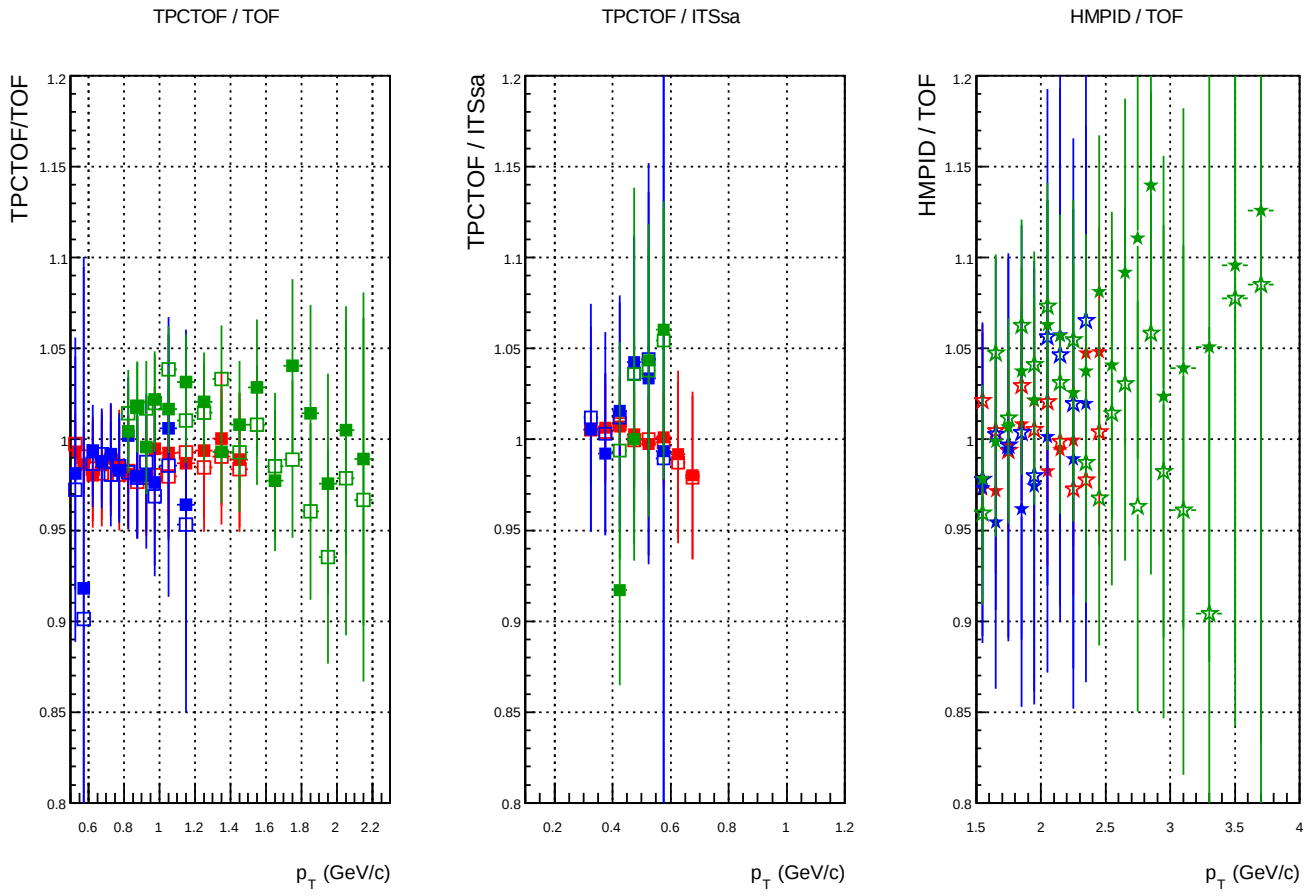

Fig. 4.19: Ratio between the 4 different analyses. Red are pions, blue are kaons and green are protons. Full point are the particle while open point the antiparticles.

The low p_{T} analysis composed for these 4 different analysis is also combined with the high p_{T} analysis, which use a statistical method based on the relativistic rise of the particles to do the PID. The full combination of the spectra is shown in Fig. 4.20 have a p_{T} range from 100 MeV/c till 20 GeV/c for pions, kaons and protons.

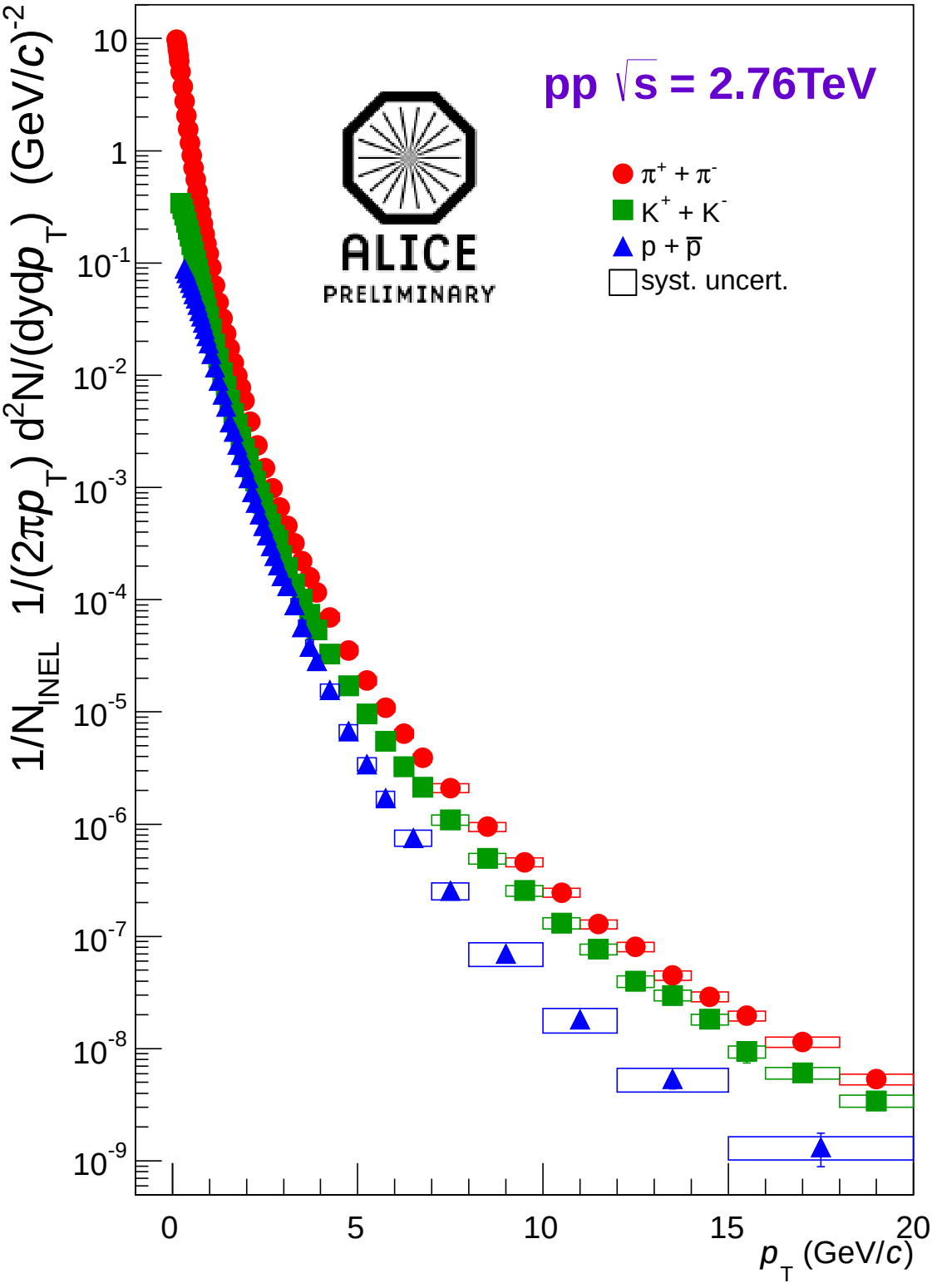

Fig. 4.20: ALICE preliminary combined spectra for pions, kaons and protons in pp collisions at 2.76 TeV.

4.6.2 Particle ratios

The particle ratios $\frac{K^+ + K^-}{\pi^+ + \pi^-}$ and $\frac{p+\bar{p}}{\pi^+ + \pi^-}$ with statistic and systematic errors are shown for only the low p_{T} combined spectra in Fig. 4.21.

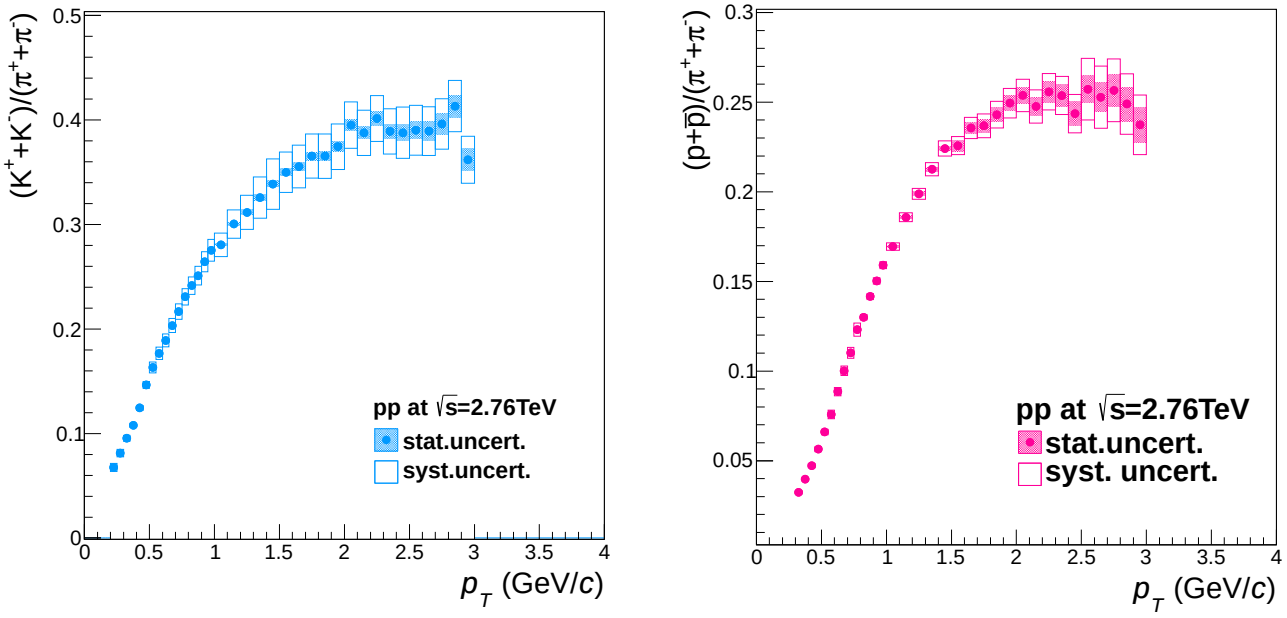

Fig. 4.21: Particle ratios. *Left:* $\frac{K^+ + K^-}{\pi^+ + \pi^-}$ and *Right:* $\frac{p+\bar{p}}{\pi^+ + \pi^-}$ for pp collisions at $\sqrt{s}$ = 2.76 TeV.

The full particle ratios $\frac{K^+ + K^-}{\pi^+ + \pi^-}$ and $\frac{p+\bar{p}}{\pi^+ + \pi^-}$ with only systematic uncertainties are shown in Fig. 4.22. The high p_{T} results has been taken from [27], and shows a better agreement with low p_{T} results than the preliminaries, due to the better understanding of the PID using the relativistic rise.[11].

[11] *arxiv:* 1401.1250.

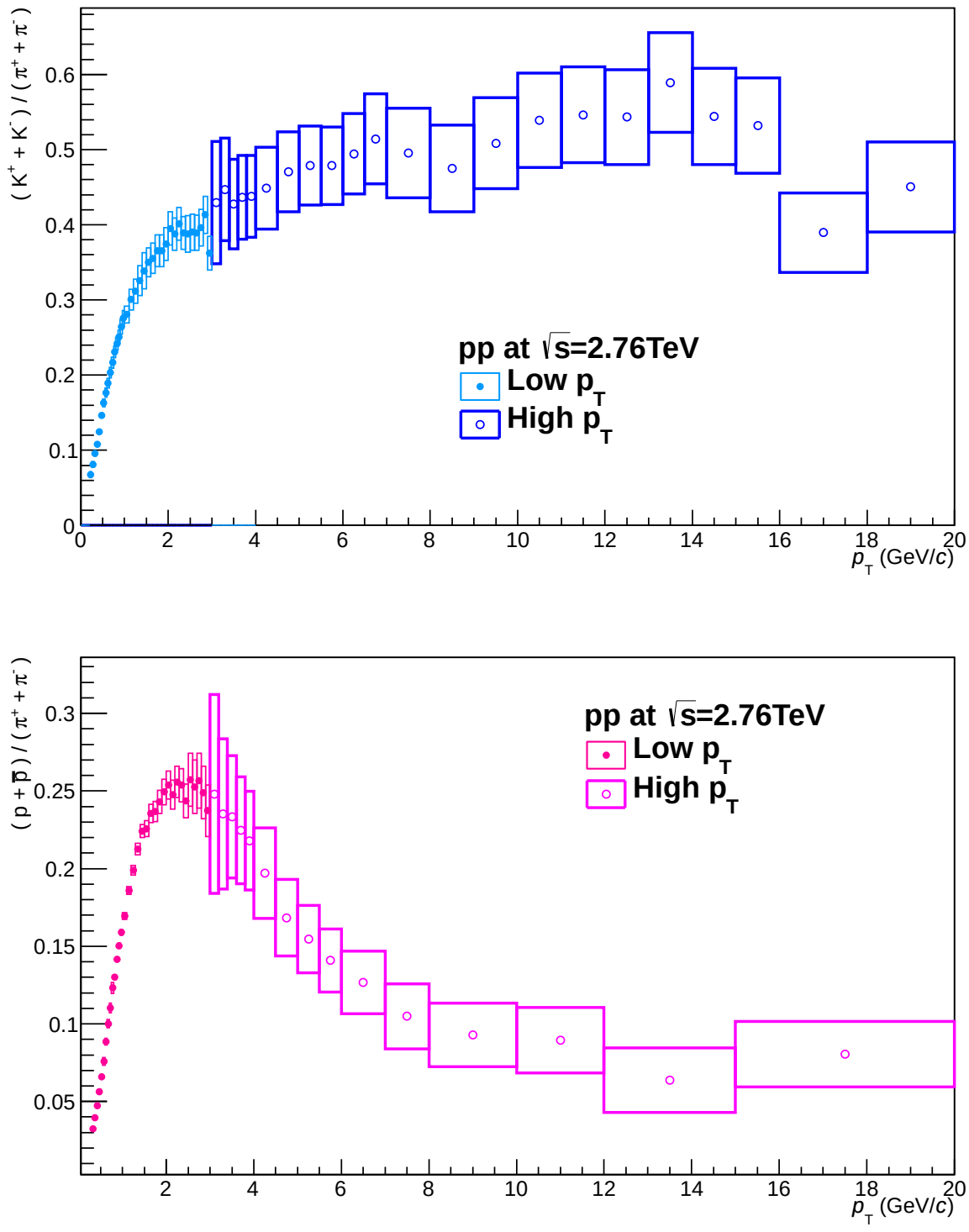

Fig. 4.22: Particle ratios. *Top:* $\frac{K^+ + K^-}{\pi^+ + \pi^-}$ and *Bottom:* $\frac{p+\bar{p}}{\pi^+ + \pi^-}$ for pp collisions at $\sqrt{s}$ = 2.76 TeV. This plots are composed by the preliminary low p_{T} and the final high p_{T} 2.76 TeV results

4.7 R_{AA}

The nuclear modification factor, R_{AA}, can be computed as:

$$R_{\rm AA} = \frac{\left(\frac{d^2N}{dp_{\rm T}dy}\right)_{\rm Pb-Pb}}{< N_{\rm coll} > \left(\frac{d^2N}{dp_{\rm T}dy}\right)_{\rm pp}} \tag{4.8}$$

where N_{coll} is the number of binary nucleon-nucleon collisions. N_{coll} is given by the product of nuclear overlap function T_{AA}[12] and the inelastic NN cross section $\sigma^{NN}_{\rm INEL}$[32].

The R_{AA} allows to quantify the nuclear medium effect at high $p_{\rm T}$. If the R_{AA} = 1 means that there is no nuclear modification.

Fig. 4.23 shows the results for different centralities using the results from the combined pp analysis and the Pb-Pb analysis [18]. This was obtained using the ALICE pp preliminary results for pions $<$ 2.0 GeV/c, kaons $<$ 3.0 GeV/c and protons $<$ 3.0 GeV/c corresponding to the low $p_{\rm T}$ part. The ALICE pp high $p_{\rm T}$ part from [27] and the Pb$-$Pb results from [18].

The R_{AA} shows the consistency on the suppression for protons at $p_{\rm T}$ $<$8 GeV/c, which it is also appreciated for the particle ratios in Fig. 4.21. It is also a big remark for $p_{\rm T}$ higher than 8 GeV/c the pions, kaons, and protons seems to be equally suppressed. This indicates that the particle composition at high $p_{\rm T}$ is similar in heavy ion collisions to those in the vacuum. This is an important measurement that disfavors the jet hadro-chemistry within the jets predicted previously on [33].

[12] Obtained with a simulation based on Monte Carlo Glauber calculation for a given centrality class

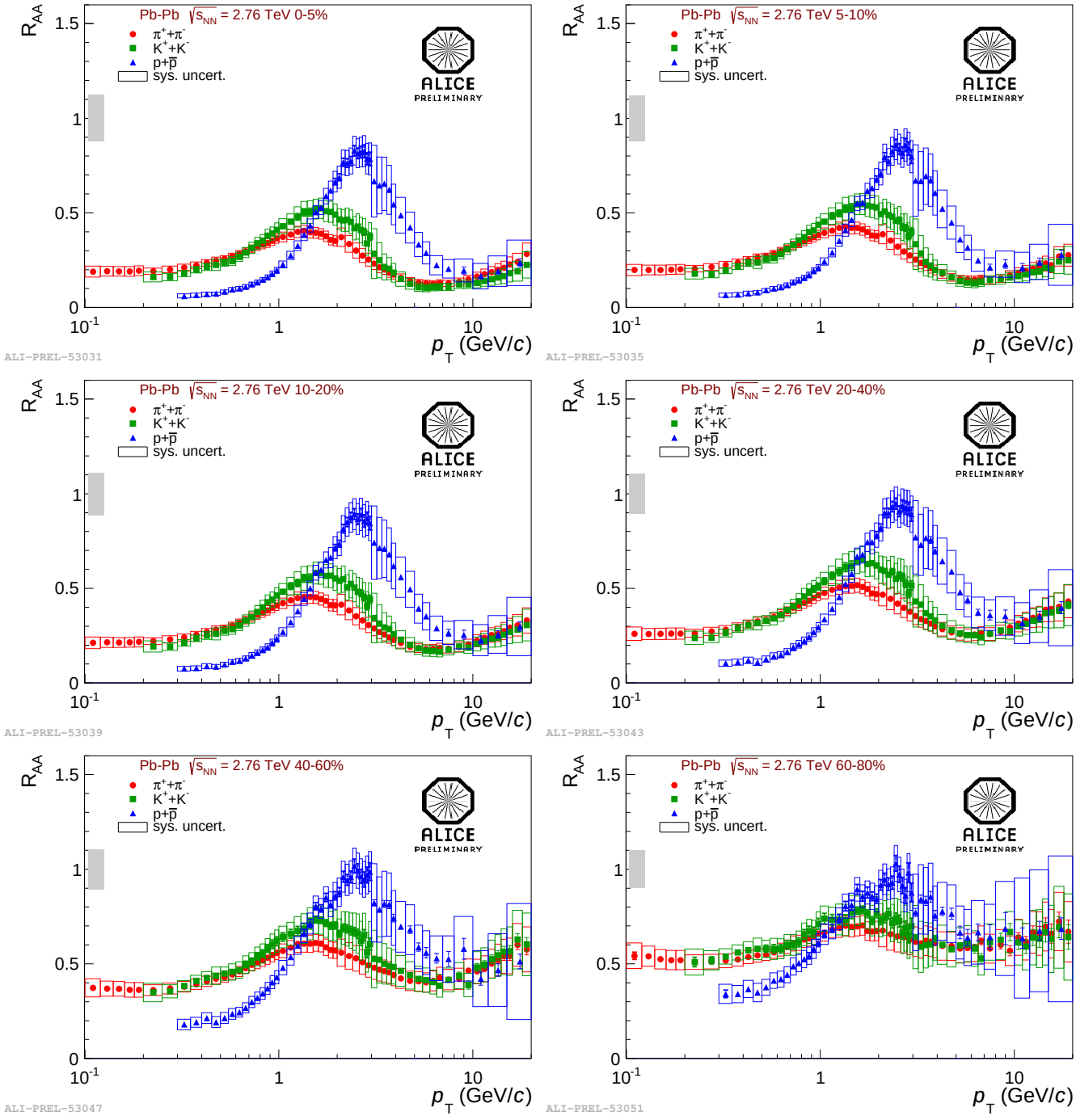

Fig. 4.23: R_{AA} for pions, kaons and protons in different centralities. Error bars indicates the statistical errors and the boxes contain the systematic uncertainties

5

Results for other energies

The low p_{T} particle spectra in the ALICE collaboration has different status at the present. The 900 GeV analysis is already published on [17], the 2.76 and 7.0 TeV analyses are preliminary. In this chapter the results were obtained used the same method explained in Chapter 4. Some details of each energy analysis are presented in the following:

5.1 900 GeV analysis

The main differences with ALICE published results and the analysis done by the author are two:

1. The amount of statistics: This work uses 10 millions of MB events while the published results has 300,000 events only.
2. The low statistics didn't allow to notice the exponential tail on the response function of the time of flight.

Due to this, some examples of the fits for the different mass hypothesis are shown in Fig. 5.1, 5.2, and 5.3 for pp collisions at $\sqrt{s}$ = 900 GeV.

The tracking efficiency is shown in Fig. 5.4.

The matching efficiency is shown in Fig. 5.5.

The Final Spectra for the 900 GeV analysis is shown in Fig. 5.6

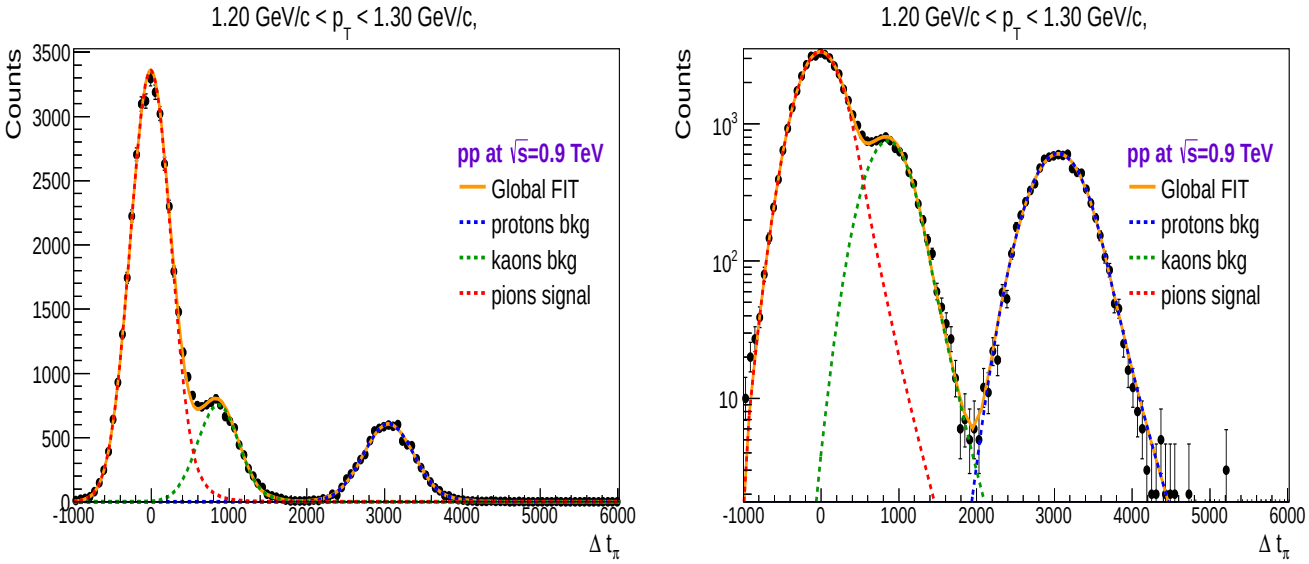

Fig. 5.1: Fit example for the pion signal (red), kaon background (green) and proton background (blue).The global fit (orange) to the data points is the sum of the signal and the background. Left panel: Linear Scale. Right panel: Log scale.

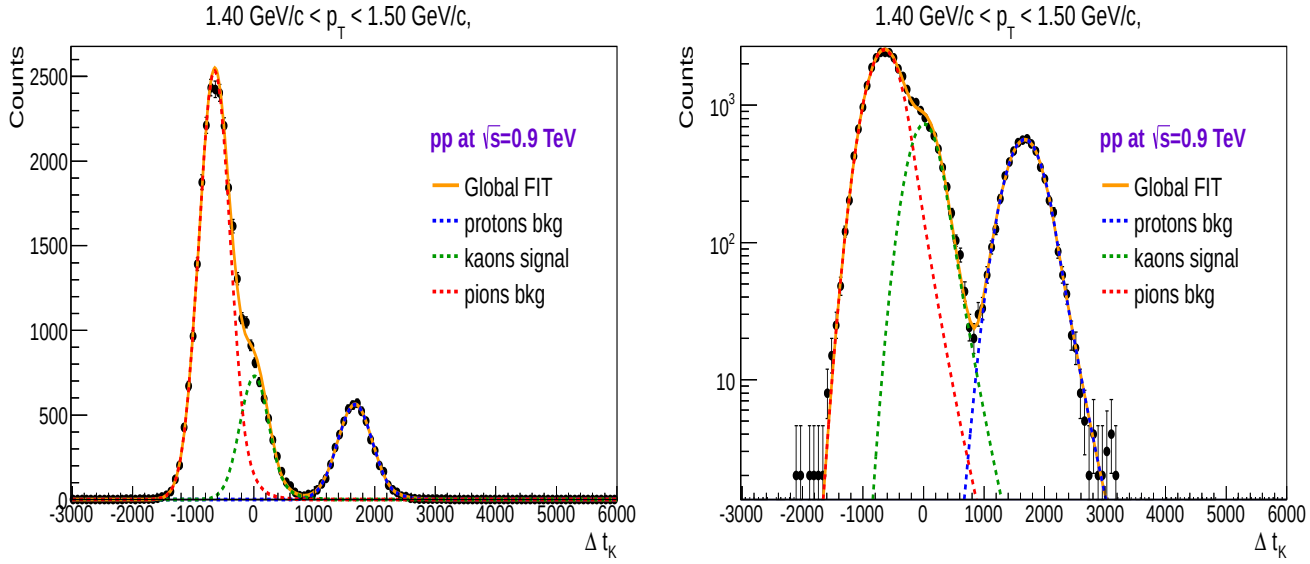

Fig. 5.2: Fit example for the kaon signal (green), pion background (red) and proton background (blue).The global fit (orange) to the data points is the sum of the signal and the background. Left panel: Linear Scale. Right panel: Log scale.

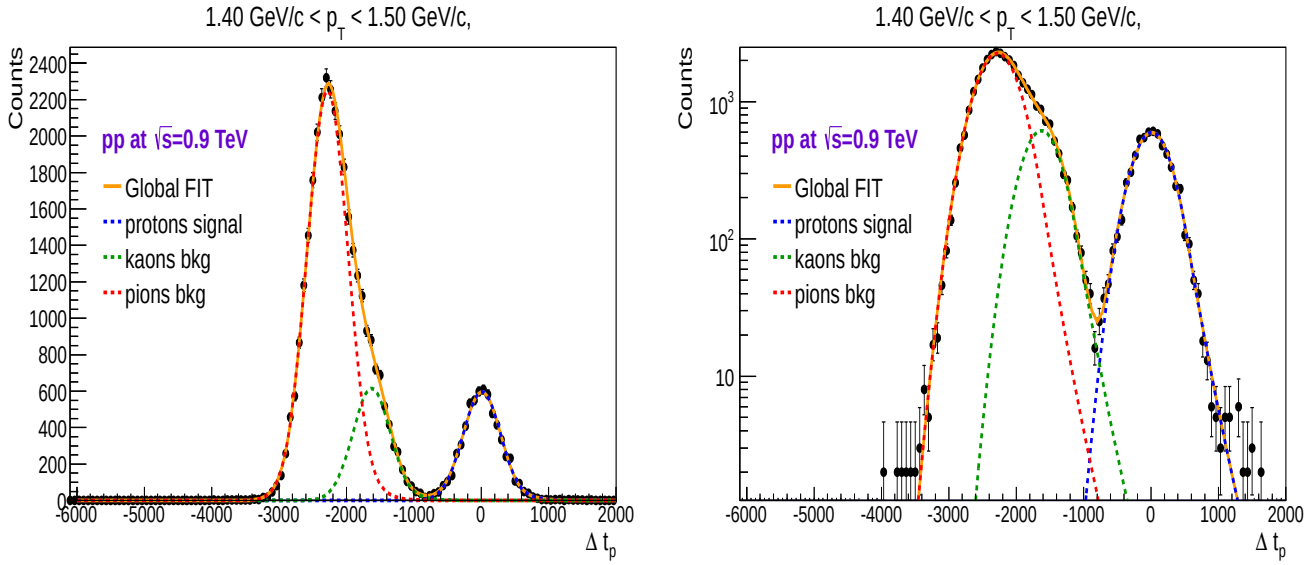

Fig. 5.3: Fit example for the proton signal (blue), kaon background (green) and pion background (red).The global fit (orange) to the data points is the sum of the signal and the background. Left panel: Linear Scale. Right panel: Log scale.

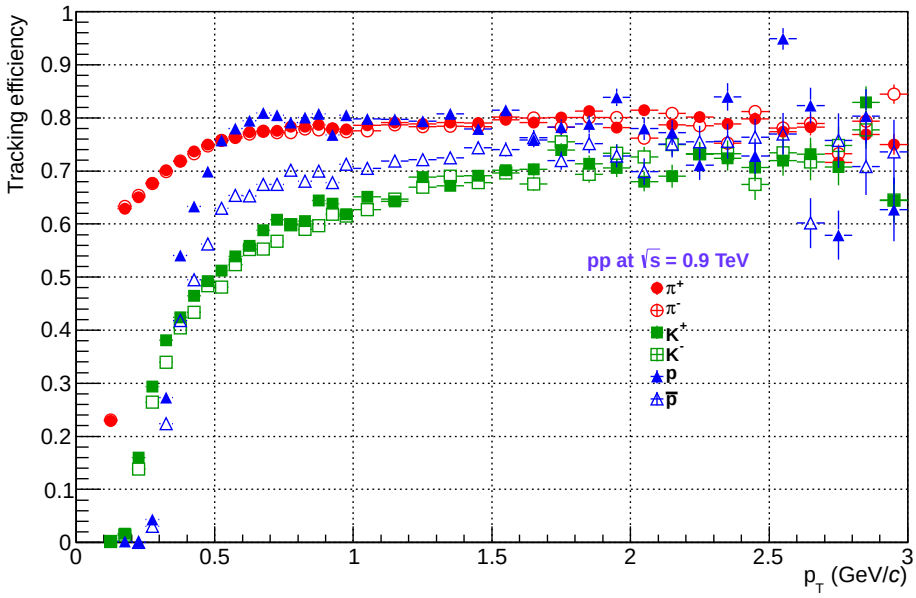

Fig. 5.4: Tracking efficiency for all particle species in pp collisions at $\sqrt{s}$ = 0.9 TeV.

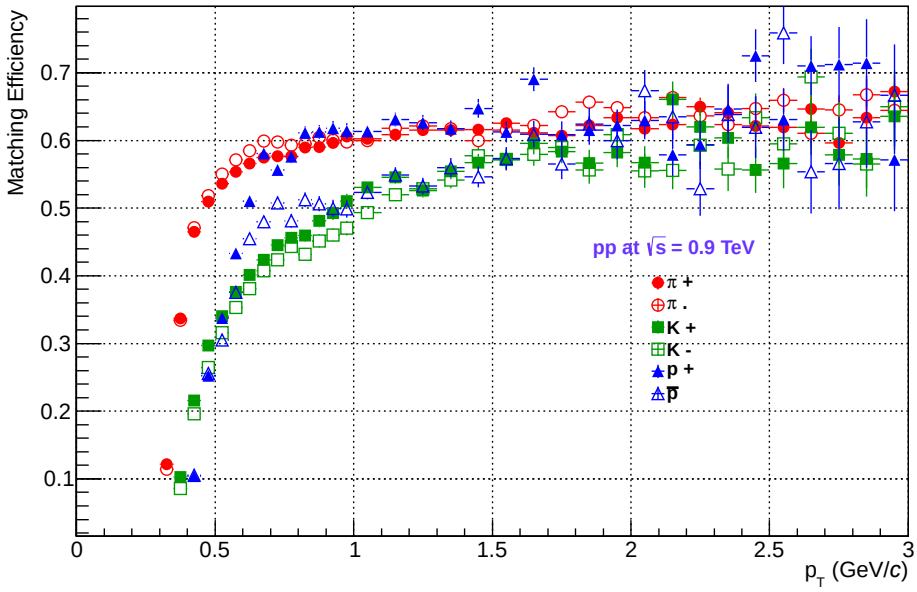

Fig. 5.5: Matching efficiency for all particle species in pp collisions at $\sqrt{s}$ = 0.9 TeV.

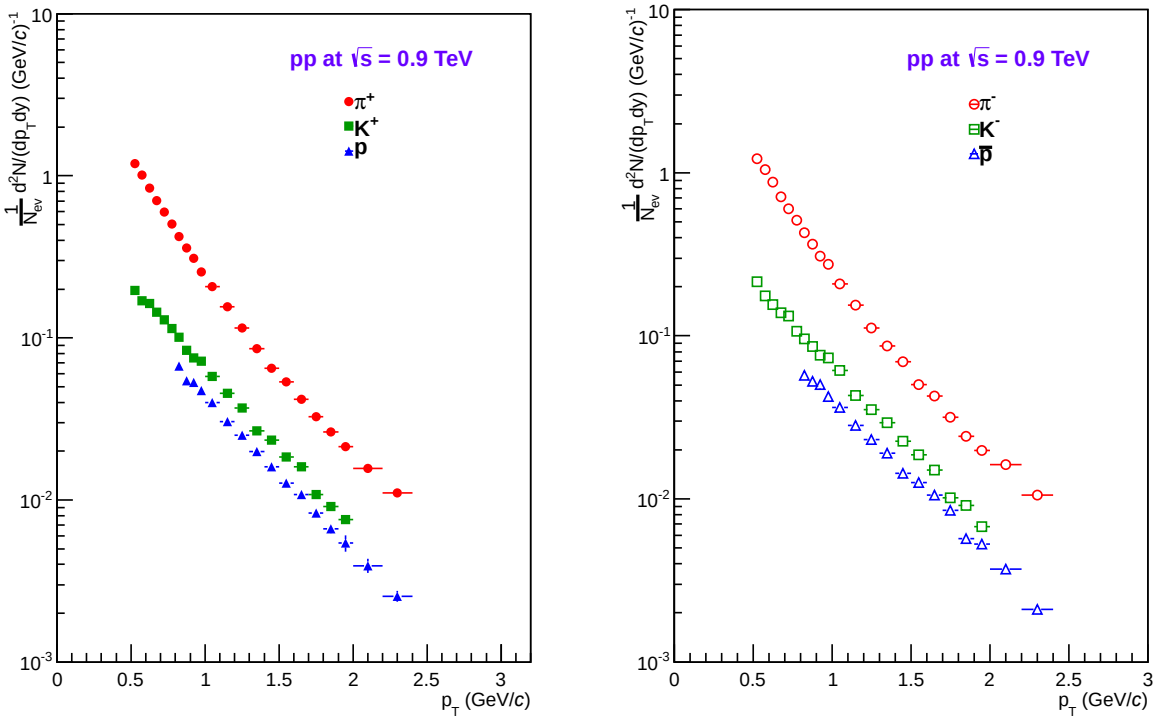

Fig. 5.6: Left: TOF final spectra for positive charged hadrons. Right: TOF final spectra for negative charged hadrons. Only statistical errors plotted.

5.2 7 TeV analysis

Due to this, some examples of the fits for the different mass hypothesis are shown In Fig. 5.7, 5.8, and 5.9 for pp collisions at $\sqrt{s}$ = 7.0 TeV.

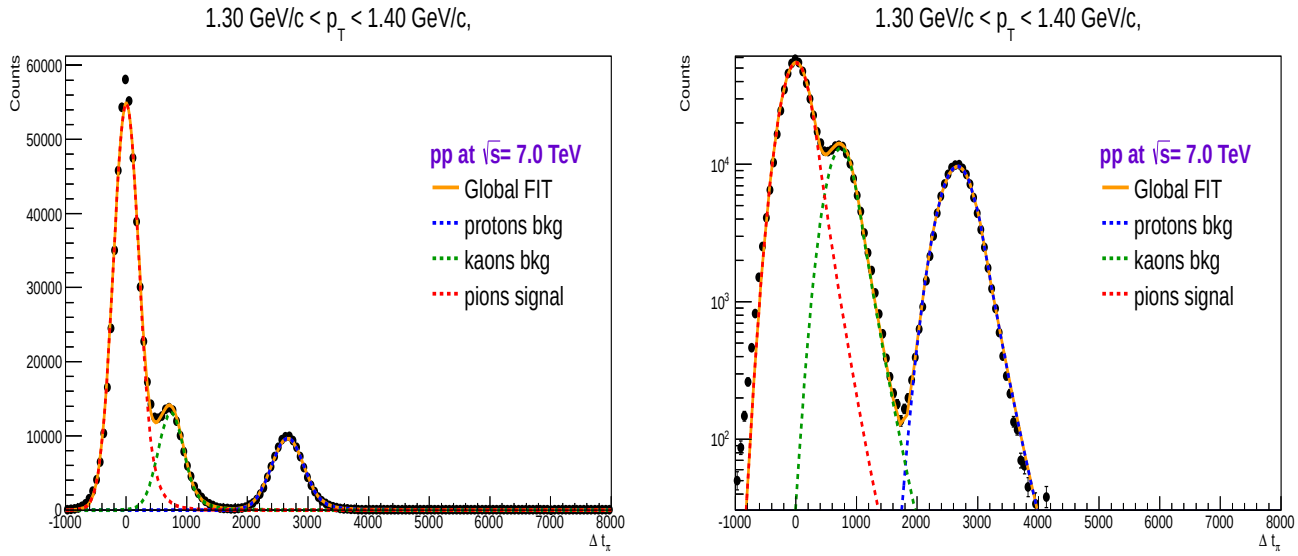

Fig. 5.7: Fit example for the pion signal (red), kaon background (green) and proton background (blue).The global fit (orange) to the data points is the sum of the signal and the background. Left panel: Linear Scale. Right panel: Log scale.

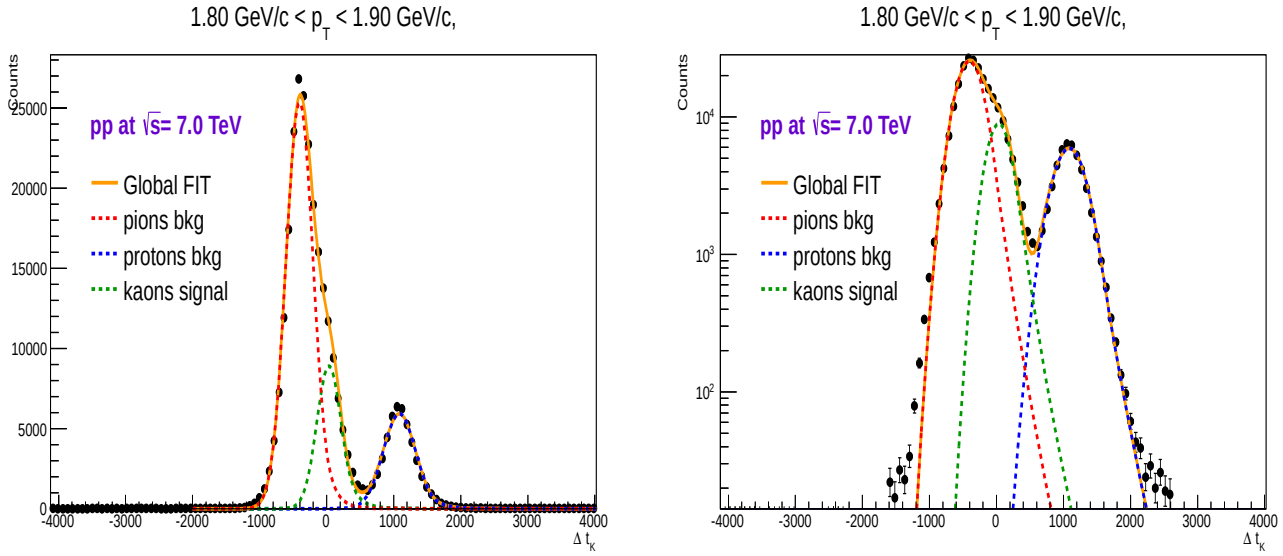

Fig. 5.8: Fit example for the kaon signal (green), pion background (red) and proton background (blue).The global fit (orange) to the data points is the sum of the signal and the background. Left panel: Linear Scale. Right panel: Log scale.

The Final Spectra for the 7 TeV analysis is shown in Fig. 5.10, and the comparison with preliminary ALICE results is shown in Fig. 5.11, the results shown here are on

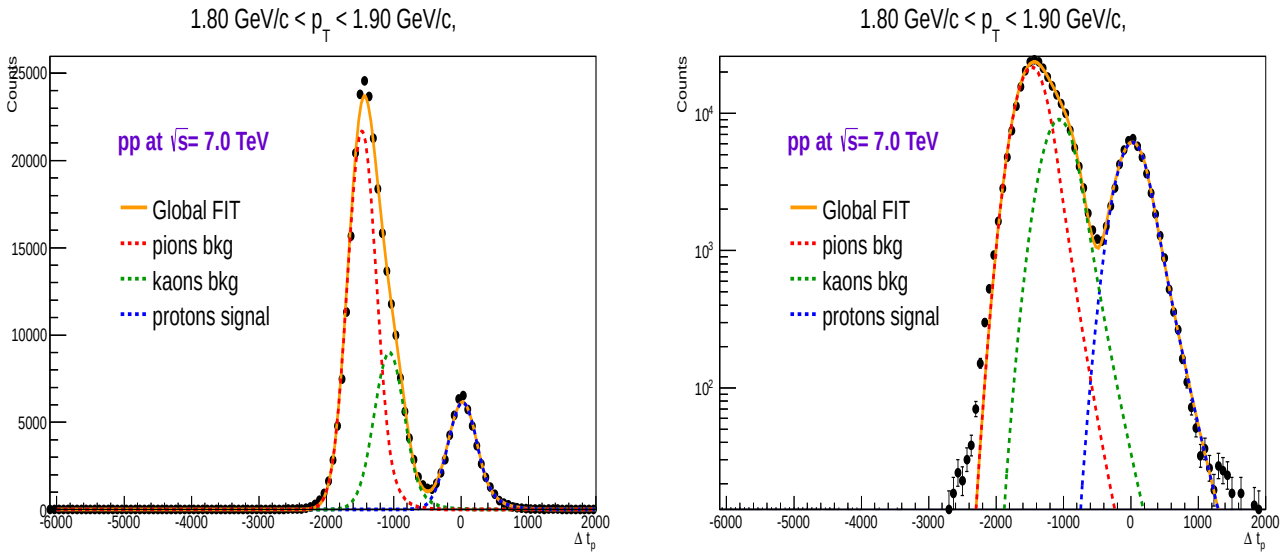

Fig. 5.9: Fit example for the proton signal (blue), kaon background (green) and pion background (red).The global fit (orange) to the data points is the sum of the signal and the background. Left panel: Linear Scale. Right panel: Log scale.

agreement with preliminary results for all species.

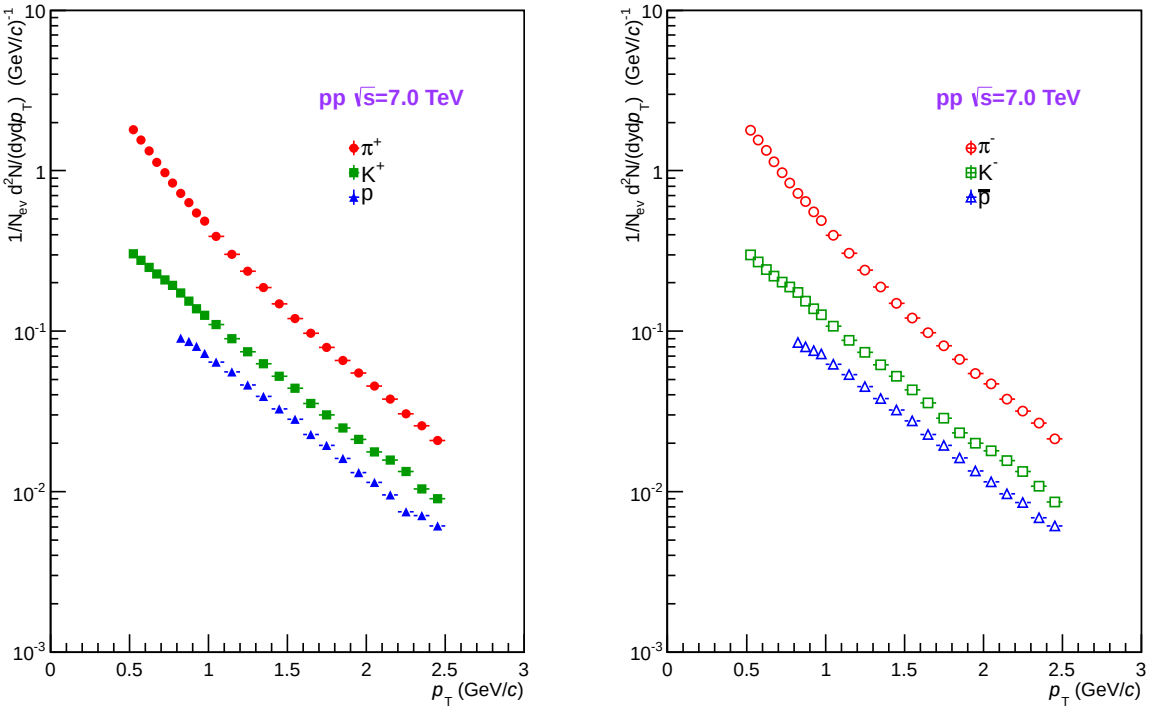

Fig. 5.10: *Left*: TOF final spectra for positive charged hadrons. *Right*: TOF final spectra for negative charged hadrons. Only statistical errors plotted.

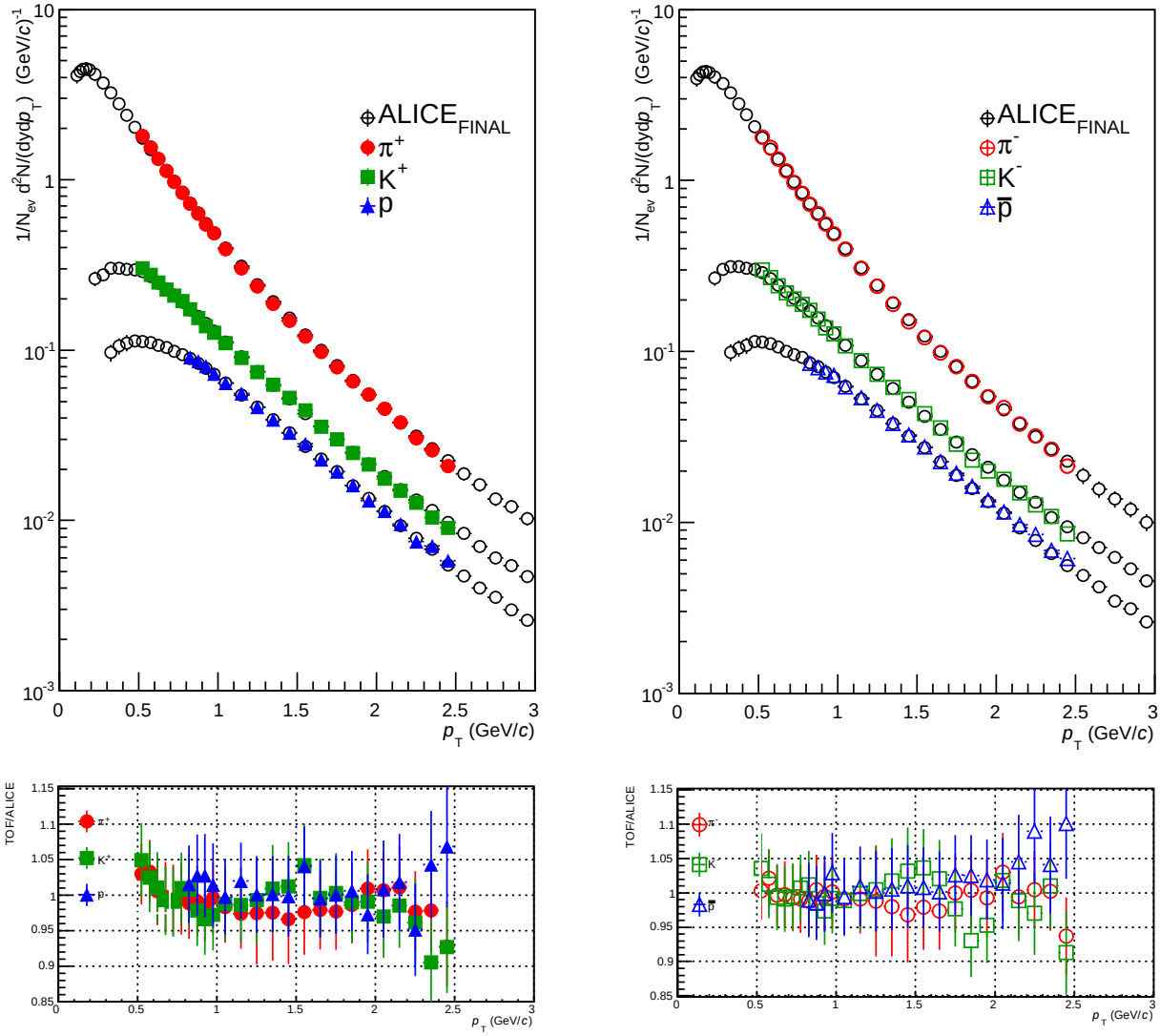

Fig. 5.11: *Left*: TOF spectra and ALICE preliminary for positive charged hadrons. *Right*: TOF and ALICE preliminary spectra for negative charged hadrons.The bottom plots show the ratios respect to ALICE preliminary results.

5.3 Particle ratios

Fig. 5.12 shows a comparison of the particle ratios using the 3 different results obtained in this work. No energy dependence is observed, note that Fig. 5.12 only shows statistical errors.

The Fig. 5.13 shows a comparison of the particle ratios using the 900 GeV results, the 2.76 and 7 TeV ALICE preliminary results. It is important to mention that the statistical uncertainties in the 900 GeV results are not negligible.

The 900 GeV analysis was redone with the new sample of statistics following the same procedure explained in this chapter. All the details concerning this analysis can be found

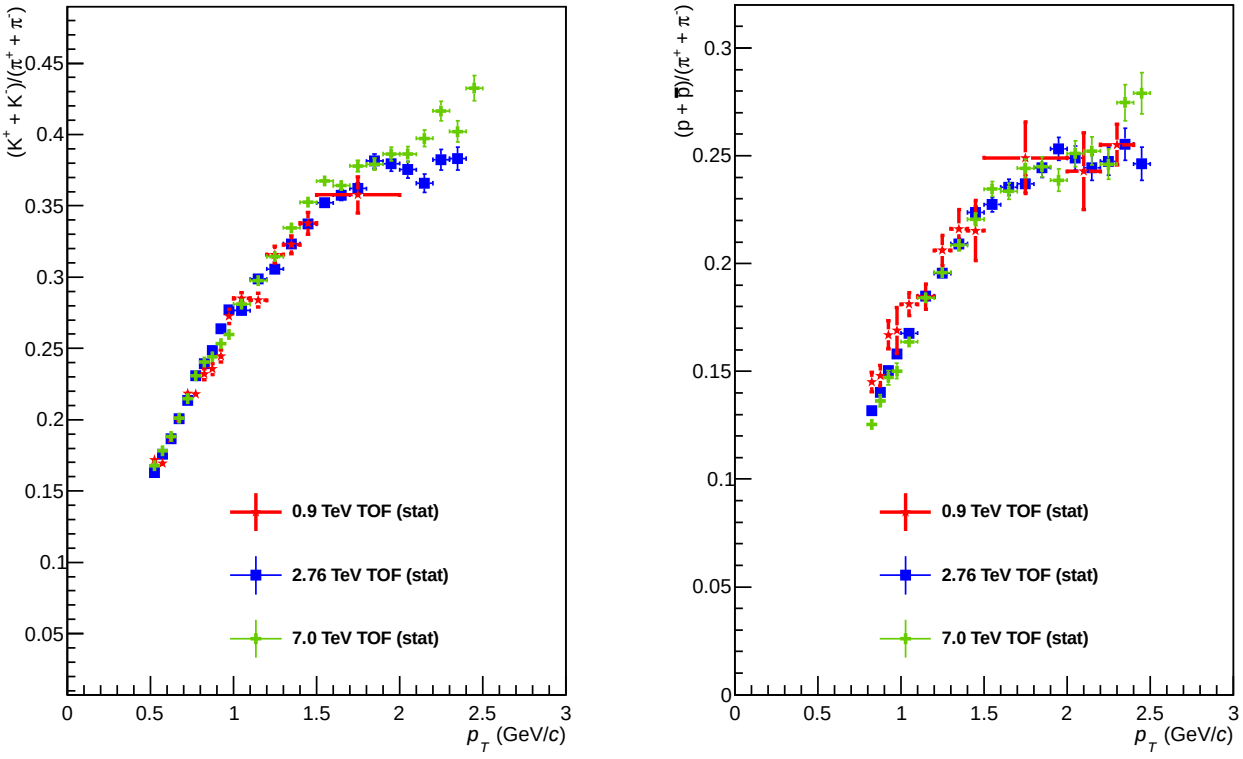

Fig. 5.12: Particle ratios measured at 3 different energies with TOF. *Left*: p/π. *Right*: K/π.

in Appendix A. A nice improvement can be seen in Fig. 5.13. The particle ratios for the 3 energies are equal within statistical errors. No dependence of the ratios K/π and p/π are observed increasing the $\sqrt{s}$.

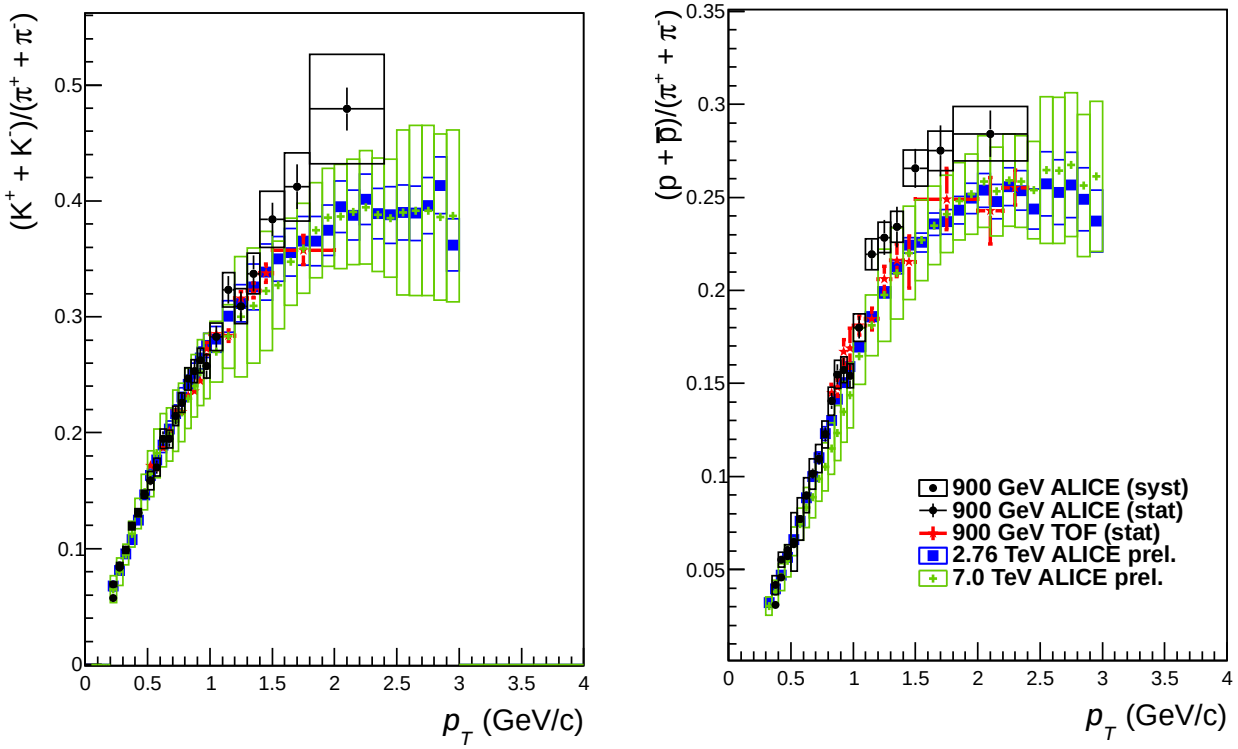

Fig. 5.13: Particle ratios for the 3 different energies. The red 900 GeV TOF points were obtained by the author, the black points corresponds to ALICE data from [17], the blue and green points correspond to ALICE preliminary results at $\sqrt{s}$ = 2.76 and 7 TeV respectively, with only systematic errors for clarity.

6

Transverse Sphericity

The usual strategy in analyzing and explaining the results is to present averaged data and giving the opportunity to theorists to employ their tools to weight the complexity of the data with different theoretical contributions. Another approach is to present the data in a a way where at least some complexity is removed. This is done used the so-called event shapes structures of the events. Usually the events have very different and identifiable structures. In the present work we present the analysis using transverse sphericity (S_{T}) . S_{T} has been already reported for primary charged particles by ALICE [34] and ATLAS [35]. In this chapter an analysis of the identified particle spectra for different S_{T} events are presented. The aim is to use the S_T as a tool to separate jetty events (hard processes) from isotropic events (soft processes) and see observe the particle production in this two opposite types of events.

6.1 S_{T} definition

Given a set of pp events data one can evaluate the various global parameters which can be used to classify and characterize the events. At hadrons colliders, event shape analyses are restricted to the transverse plane in order to avoid the boost along the beam axis [37].

To calculate the transverse sphericity we need to use the transverse momentum matrix:

$$S_{XY} = \begin{pmatrix} p_{x_i^2} & p_{x_i}p_{y_i} \\ p_{x_i}p_{y_i} & p_{y_i^2} \end{pmatrix} \tag{6.1}$$

where (p_{x_i}, p_{y_i}) are the projections, along the x and y beam axis respectively, of the transverse momentum of the particle i.

Since S_{XY} is quadratic in particle momenta, this sphericity is a non-collinear safe quantity in pQCD. The avoid the collinear bias, In this work the same method applied by the ALICE collaboration [34] to linearize the transverse momentum matrix is used:

$$S_{\mathrm{XY}} = \frac{1}{\Sigma_i p_{T_i}} \Sigma_i \frac{1}{p_{T_i}} \begin{pmatrix} p_{x_i^2} & p_{x_i} p_{y_i} \\ p_{x_i} p_{y_i} & p_{y_i^2} \end{pmatrix} \tag{6.2}$$

The transverse sphericity is defined in terms of the eigenvalues $\lambda_1 > \lambda_2$.

$$S_{\mathrm{T}} = \frac{2\lambda_2}{\lambda_2 + \lambda_1} \tag{6.3}$$

This definition of the sphericity allow us to separate the events in two extreme configurations. The limit for low sphericity ($S_{\mathrm{T}} = 0$, which means "jetty" events, and the limit for high sphericity ($S_{\mathrm{T}} = 1$), which means "isotropic events".

6.2 Real data analysis

The data analysis presented in this section correspond to the same data sample and procedure described in Chapter 4. In order to be consistent with the definitions doped by ALICE [34], the multiplicity used was the charged particles ($\mathrm{N_{ch}}$) with p_{T} > 0.5 GeV/c, and also a selection of the events with $\mathrm{N_{ch}}$ >2 was applied in order to have enough particles to calculate the sphericity. The sphericity distribution is shown in Fig.6.1, this shows that the majority of the events has a sphericity $\approx$ 0.5-0.6.

The data used in this section corresponds to same data sample used for the spectra analysis explained in chapter 4. The pion, kaon and proton spectra in different sphericity bins are shown in Fig. 6.2. The kaons spectra was cut till p_{T} = 2.0 GeV/c because the results fir higher p_{T} showed oscillations obtained due to the low statistics. The low sphericity spectra for the 3 species starts to dominate at $\approx$ 2.0 GeV/c over the isotropic, however no clear effects in the spectra are appreciable at this p_{T} range.

Nevertheless, if we look the ratios we can appreciate some difference. Fig. 6.3 shows that the K^+/π^+ ratio are unaffected by the sphericity selection while the p/π^+ shows an appreciable difference in the ratio between the low sphericity and high sphericity events.

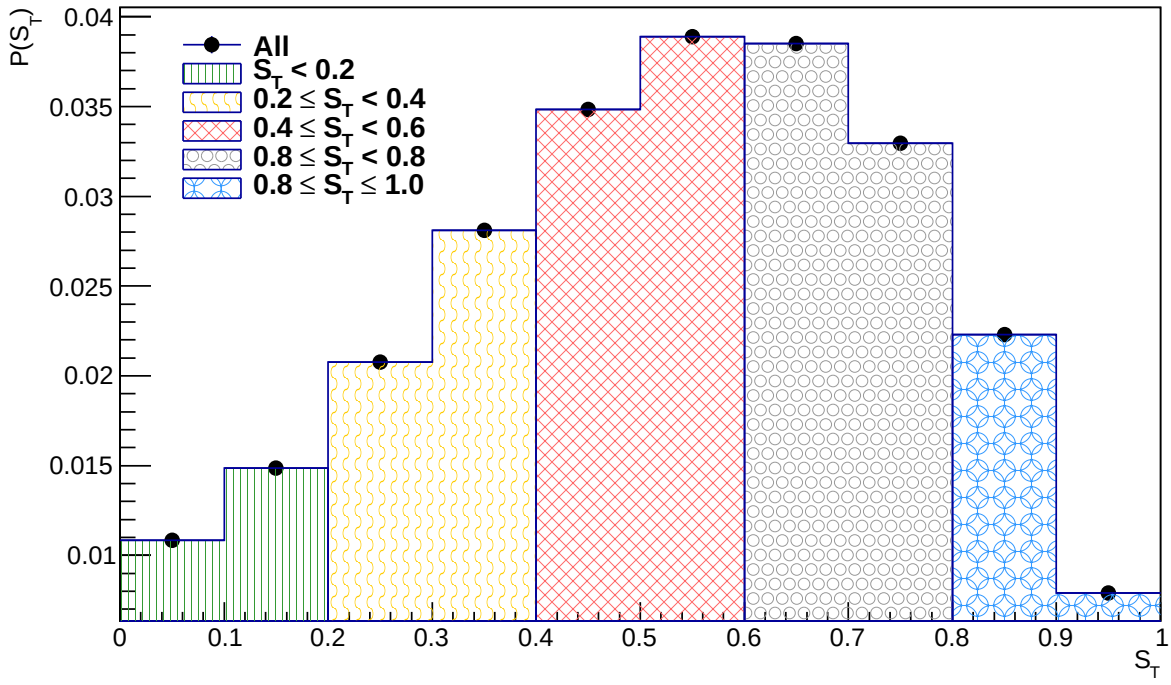

Fig. 6.1: Sphericity distribution in pp collisions at $\sqrt{s}$ = 7.0 TeV.

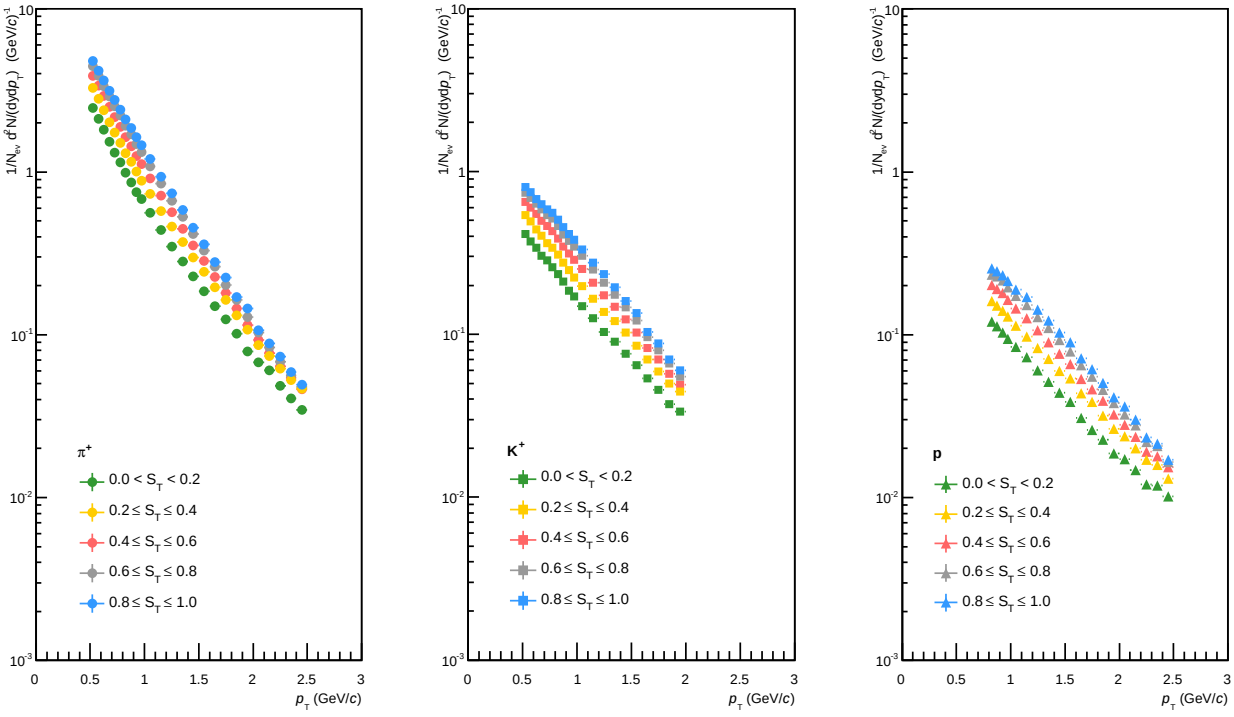

Fig. 6.2: p_{T} spectra of pions (left), kaons (middle) and protons (right) in pp collisions at $\sqrt{s}$ = 7.0 TeV for different S_{T} values.

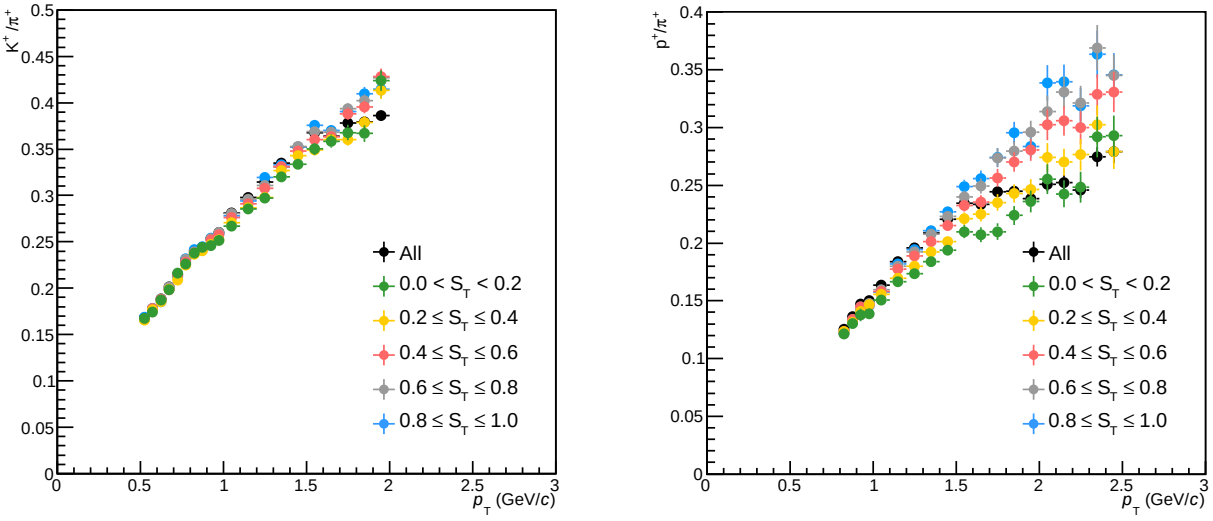

Fig. 6.3: *Left:* p/π and *Right:* K/π ratio as a function of S_{T} in pp collisions at $\sqrt{s}$ = 7.0 TeV.

6.3 MonteCarlo: Pythia 8

The results presented in this section were produced using events generated with Pythia 8, corresponding to Minimum Bias events generally related to *non-single diffractive* events. The events were generated for pp collisions at $\sqrt{s}$ = 7 TeV. The particles selected were primary charged particles including decay products except those from weak decays of strange particles, which is identical to the ALICE primary particles definition (see Section 4.1) The identified particle spectra are computed at ALICE mid-rapidity, $\mid \eta \mid < 0.8$ with a rapidity selection $\mid y_i \mid < 0.5$ (See eq. 4.2). The multiplicity is defined with the charged particles with p_{T} > 0.5 GeV/*c* in the central pseudo-rapidity region $\mid \eta \mid < 0.8$. This definition for the multiplicity and the sphericity is the same adopted by ALICE. [34].

In the reference [39] it is shown that the enhancement on the ratio p/π at around 3 GeV/*c* in PYTHIA is attributed to a mechanism called *color reconnection* (CR). [1] and it is a direct indicator of a collective phenomena present in pp collisions. Our aim is to show with PYTHIA that the enhancement present in the p/π ratio is due to isotropic events, which means, events with high sphericity ($\approx$ 0.8-1.0), and on the other side to show that this enhancement is not present in the jetty events, which means, events with low sphericity ($\approx$ 0.0-0.2). This is motivated due to the fact that in heavy ions has been reported already that the enhancement of the ratio p/π comes from the bulk part.

6.3.1 Multiplicity analysis

As the transverse sphericity depends on the multiplicity it is good to understand the behavior of the ratio as a function of the multiplicity before adding an event shape analysis. In PYTHIA the high multiplicity events are reached due to the number of Multi-parton interactions (MPI)[2]. In particular, the high multiplicity events are characterized by particles with small p_{T} . When binning in multiplicity, an approach used by other analysis [40] is to present the results as multiples of the average charged particles in a pseudo-rapidity window ($< dN_{\mathrm{ch}}/d\eta >$). The variable used to select the different multiplicity bins is $z = \frac{dN_{\mathrm{ch}}/d\eta}{<dN_{\mathrm{ch}}/d\eta>}$. The value in PYTHIA 8 obtained and used for the binning was $\frac{dN_{ch}/d\eta}{<dN_{\mathrm{ch}}/d\eta>}$ = 4.6. Thus the binning is given by

$$z = \frac{dN_{\mathrm{ch}}/d\eta}{< dN_{\mathrm{ch}}/d\eta >} = \frac{N_{ch}}{4.6} \tag{6.4}$$

where N_{ch}, is the number of particles measured in the rapidity window $\mid \eta \mid$<0.8. The multiplicity distribution is shown on Fig. 6.4. The total distribution is divided in 7 multiplicity. The table 6.1 shows the different multiplicity bins with the value of z.

[1] Color reconnection was first studied in the context of the arrangements of partons, the basic idea in the models is that the color reconnection mechanism is the probability to connect patrons by color lines. The mechanism is present in both soft and hard processes, however it has been demonstrated [39] that particles with $p_{\mathrm{T}} > 5$ GeV/*c* are not sensitive to CR.

[2] Since the hadrons are composed by partons, in a collision it is possible to have events where two or more difference hard parton interactions occur simultaneously in a single hadron-hadron collision [38]

Multiplicity bin	N_{ch}
z <1.0	3 - 5
$1.0 \leq z \leq 2.0$	5-9
$2.0 \leq z \leq 3.0$	10-14
$3.0 \leq z \leq 4.0$	15-19
$4.0 \leq z \leq 5.0$	20-24
$5.0 \leq z \leq 7.0$	25-34
$7.0 \leq z$	35 $\leq$

Table 6.1: Multiplicity bins with the corresponding number of charged particle in that multiplicity bin

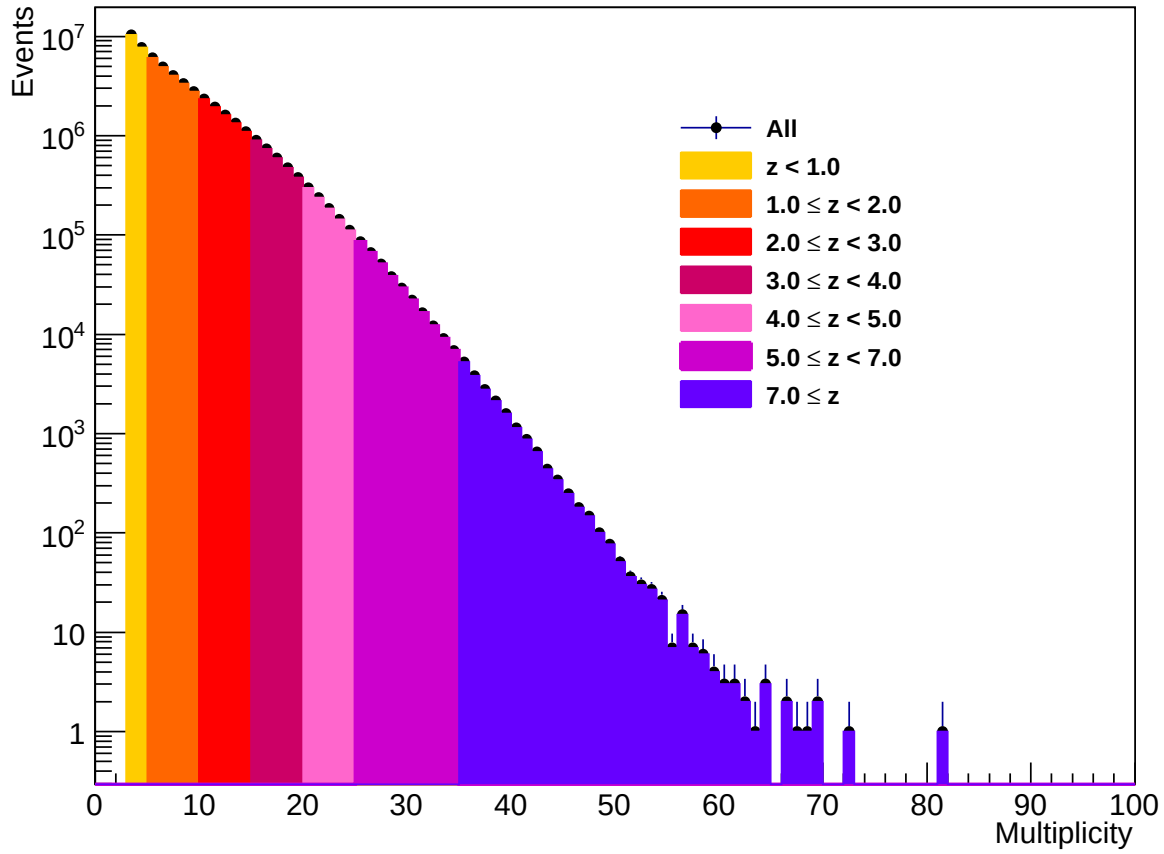

Fig. 6.4: Multiplicity distribution splited in different multiplicity bins for pp collisions at $\sqrt{s}$ =7.0 TeV. Obtained with PYTHIA 8.

Finally, the identified primary pions, kaons and proton spectra are obtained in each multiplicity bin. The spectra are shown in Fig. 6.5. To see the evolution of the hadron production the ratios p/π and K/π are obtained and shown in Fig. 6.6. There is a small dependence on the ratio p/π as a function of multiplicity. There are two observations: the first is the tiny shift of the peak to higher p_{T} with increasing multiplicity; this is analogous to Pb-Pb collisions where the peak of the p/π ratio moves to higher p_{T} when

increasing the centrality of the event. [27]. The second observation is the enhancement of the p/π ratio decreases slightly with multiplicity.

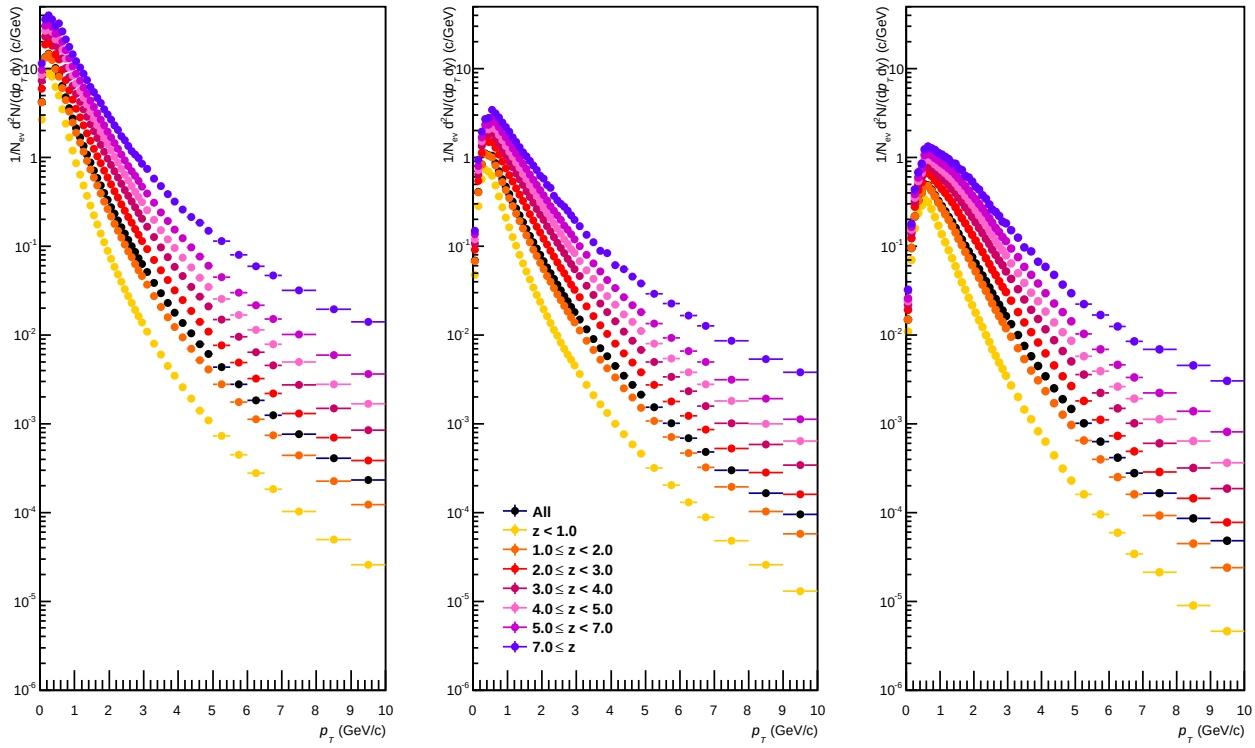

Fig. 6.5: p_{T} spectra of pions (left), kaons (middle) and protons (right) in pp collisions at $\sqrt{s}$ = 7.0 TeV for different z multiplicity values.

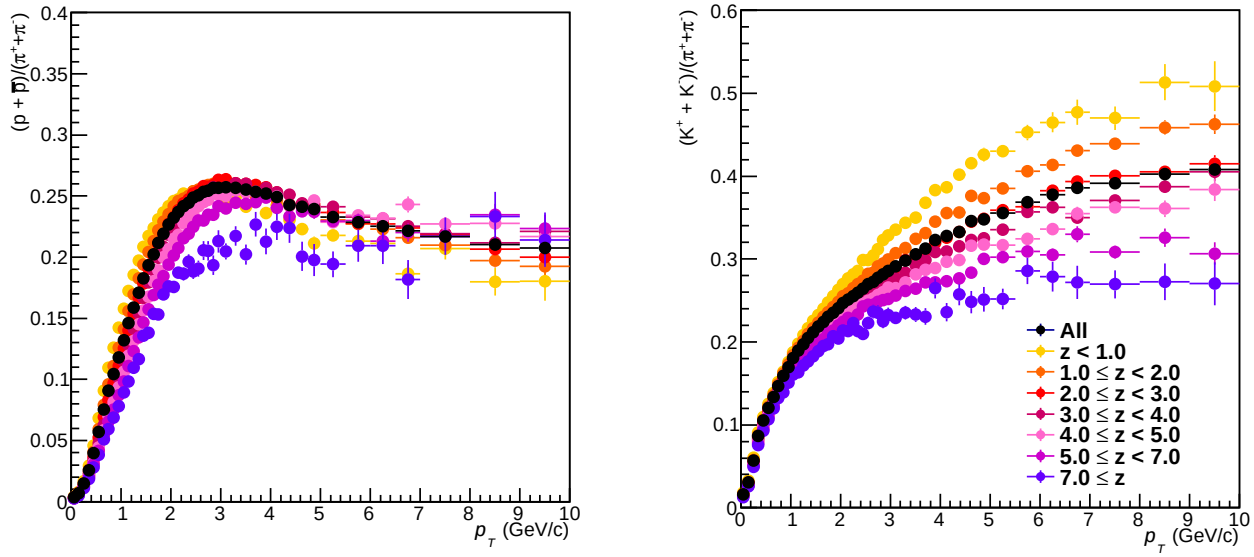

Fig. 6.6: p/π ratio as a function of multiplicity in pp collisions at $\sqrt{s}$ = 7.0 TeV with PYTHIA 8.

The CR mechanism produces the peak in the p/π ratio, so that the peak disappears in the sample without CR shown on Fig. 6.7. but it is important to see that the behavior

of the ratio for different multiplicity bins is qualitatively the same in the CR and noCR sample.

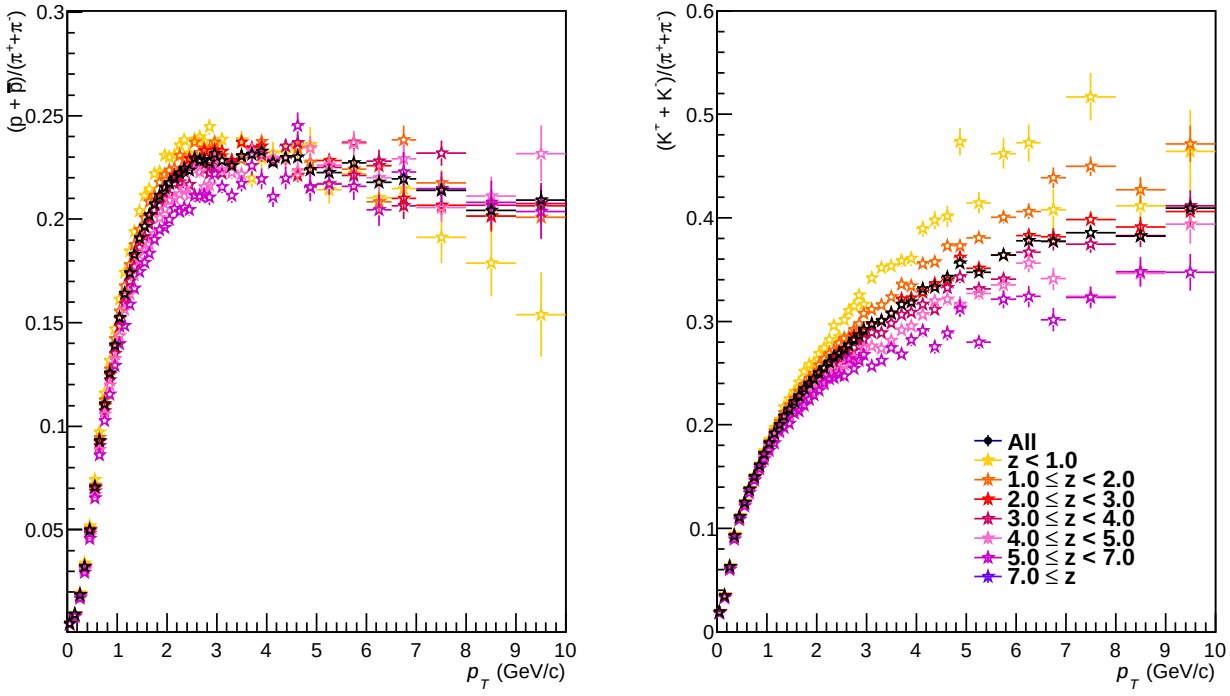

Fig. 6.7: p/π ratio as a function of multiplicity in pp collisions at $\sqrt{s}$ = 7.0 TeV. Obtained with PYTHIA 8 without color reconnection (RR=0).

6.3.2 Sphericity analysis

The total sphericity distribution is divided in 5 sphericity regions as same as data: **jetty events** ($0 < S_{\mathrm{T}} < 0.2$), **isotropic events** ($0.8 < S_{\mathrm{T}} < 1.0$), **no structure events** ($0.2 \leq S_{\mathrm{T}} \leq 0.8$). The spectra for pions, kaons and protons are shown in Fig. 6.8. It is obvious the different behavior between the two limits S_{T} bins. The spectra in the isotropic events dominates in the low p_{T} part of the p_{T} spectra till $\approx$ 3.0 GeV/c, for $p_{\mathrm{T}} >$ 3.0 GeV/c the isotropic spectra are clearly suppressed respect to the jetty spectra. This behavior is in agreement with our expectations due to the properties of the event selection with the S_{T}. We expect most of the isotropic events to have high multiplicity of low p_{T} particles, whereas the jetty events are composed by high p_{T} particles.

Fig. 6.9 shows a difference of up to 15% on the p/π ratio between the two limit S_{T} regions. If we focus in the two limit values: jetty and isotropic it is clear that the enhancement at $\approx$ 3.0 GeV/c in the p/π ratio is not present in the jets, whereas for the isotropic events this enhancement in the p/π ratio is bigger respect to the the MB.

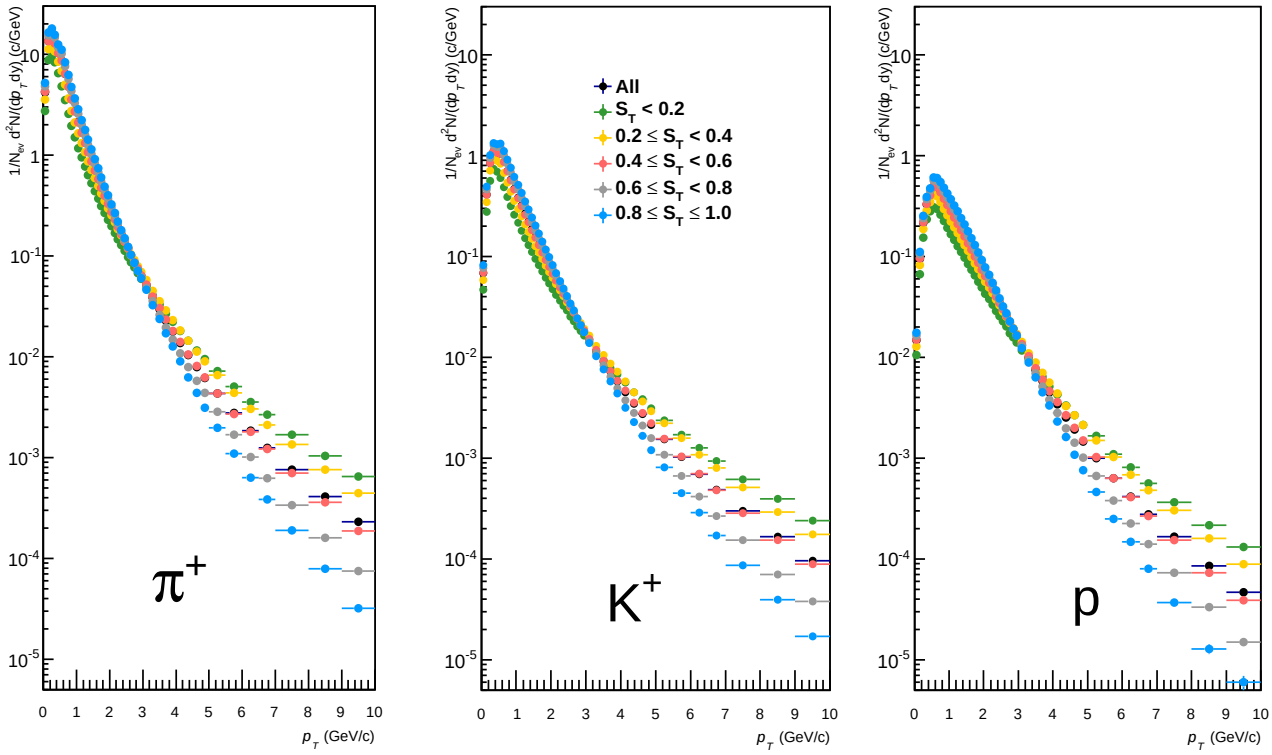

Fig. 6.8: p_{T} spectra of pions (left), kaons (middle) and protons (right) in pp collisions at $\sqrt{s}$ = 7.0 TeV for different sphericity bins. Obtained with PYTHIA 8.

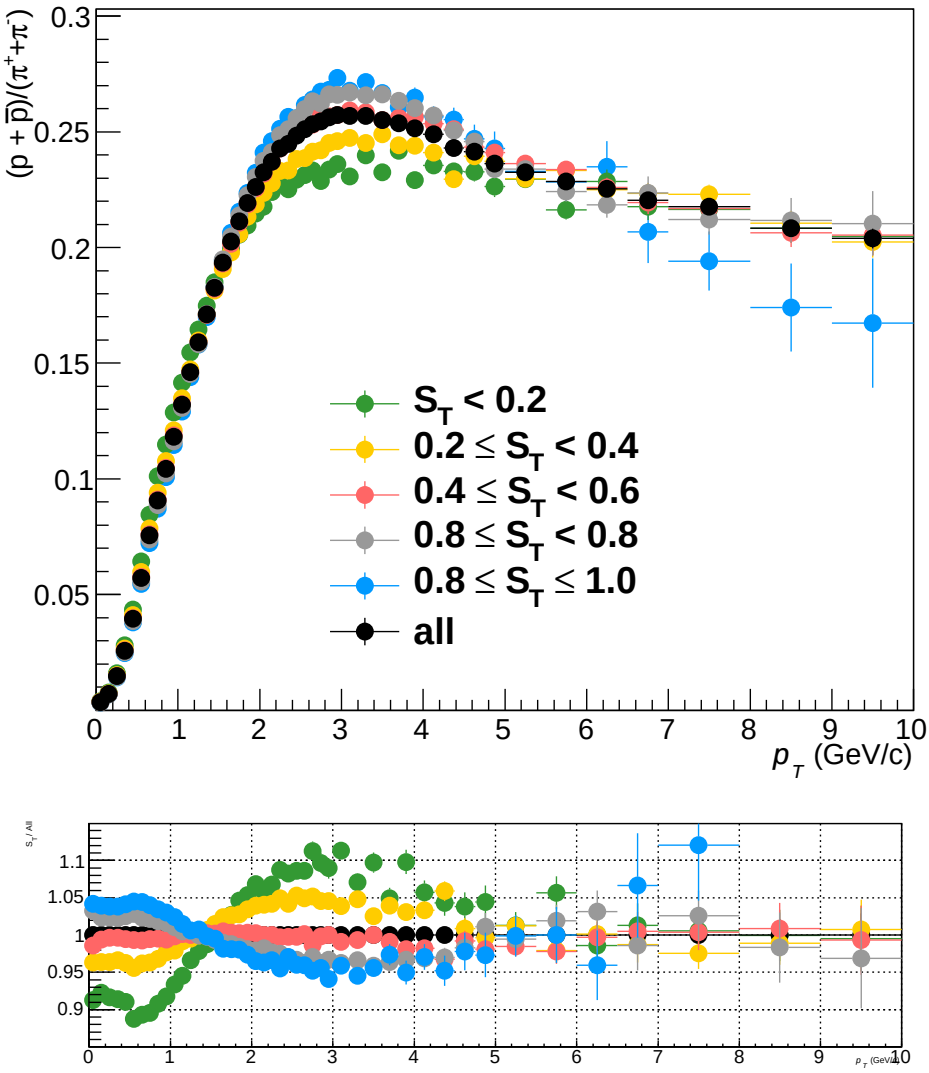

Fig. 6.9: p/π for pp collisions at $\sqrt{s}$ = 7.0 TeV in different S_{T} bins. Obtained with PYTHIA 8

Fig. 6.10 shows the p/π ratio for different S_{T} bins without color reconnection mechanism on PYTHIA, the difference on the p/π ratio shows a difference $\approx$ 7-8 %. If we compare the effect of color reconnection mechanism (Fig. 6.11) in the ratio p/π in the two regions of interest, we observe that the isotropic suffers some effect while the jets are practically unaffected. This is also expected because the jetty events are dominated by low number of MPI, and color reconnection starts to contribute for events with more than 5 MPI, which seems to affect more to the isotropic events that have more quantity of MPI.

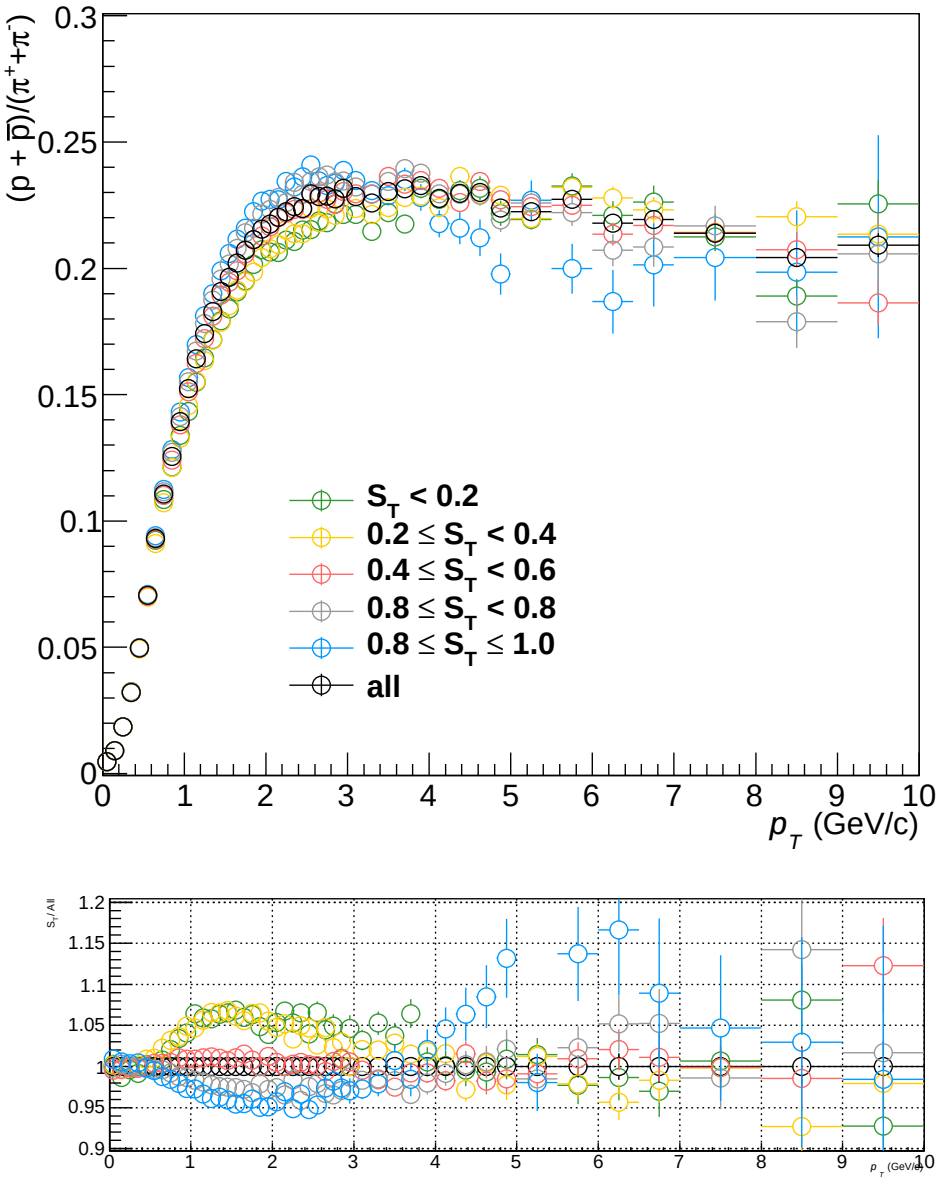

Fig. 6.10: p/π for pp collisions at $\sqrt{s}$ = 7.0 TeV in different S_{T} bins. Obtained with PYTHIA 8 using RR=0.

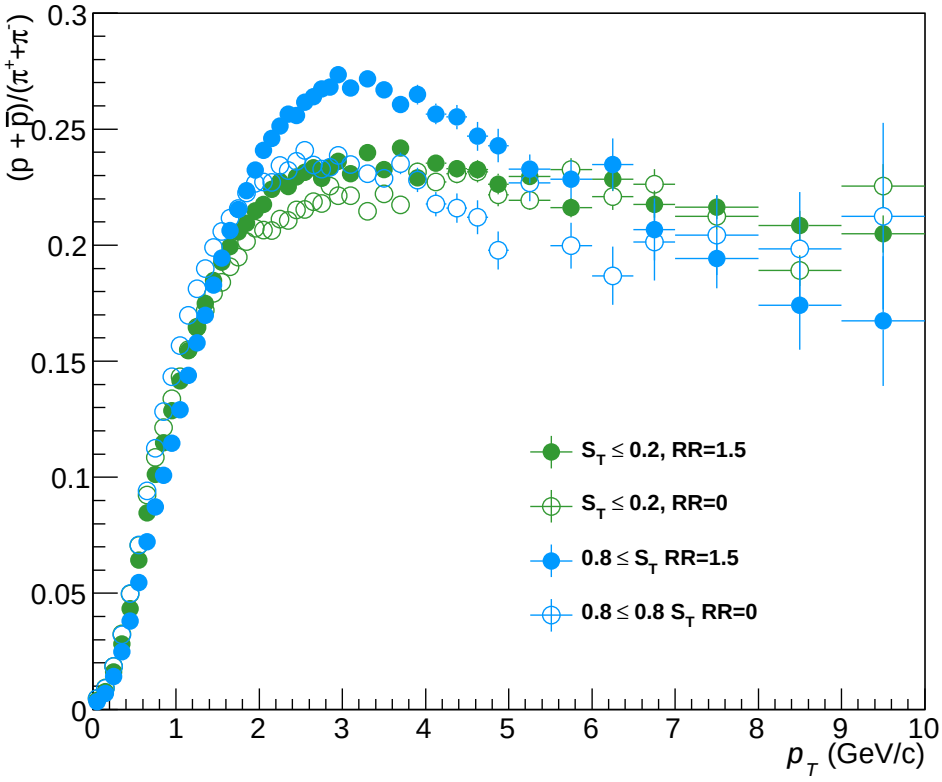

Fig. 6.11: p/π for pp collisions at $\sqrt{s}$ = 7.0 TeV in different S_{T} bins. Obtained with PYTHIA 8 using RR=1.5 and RR=0.

6.3.3 Combining S_{T} and multiplicity.

After describing the evolution of the p/π ratio with the multiplicity and the sphericity, we can combine them and use the sphericity bins for several z bins at the same time. The ratios p/π are shown in Fig. 6.12.

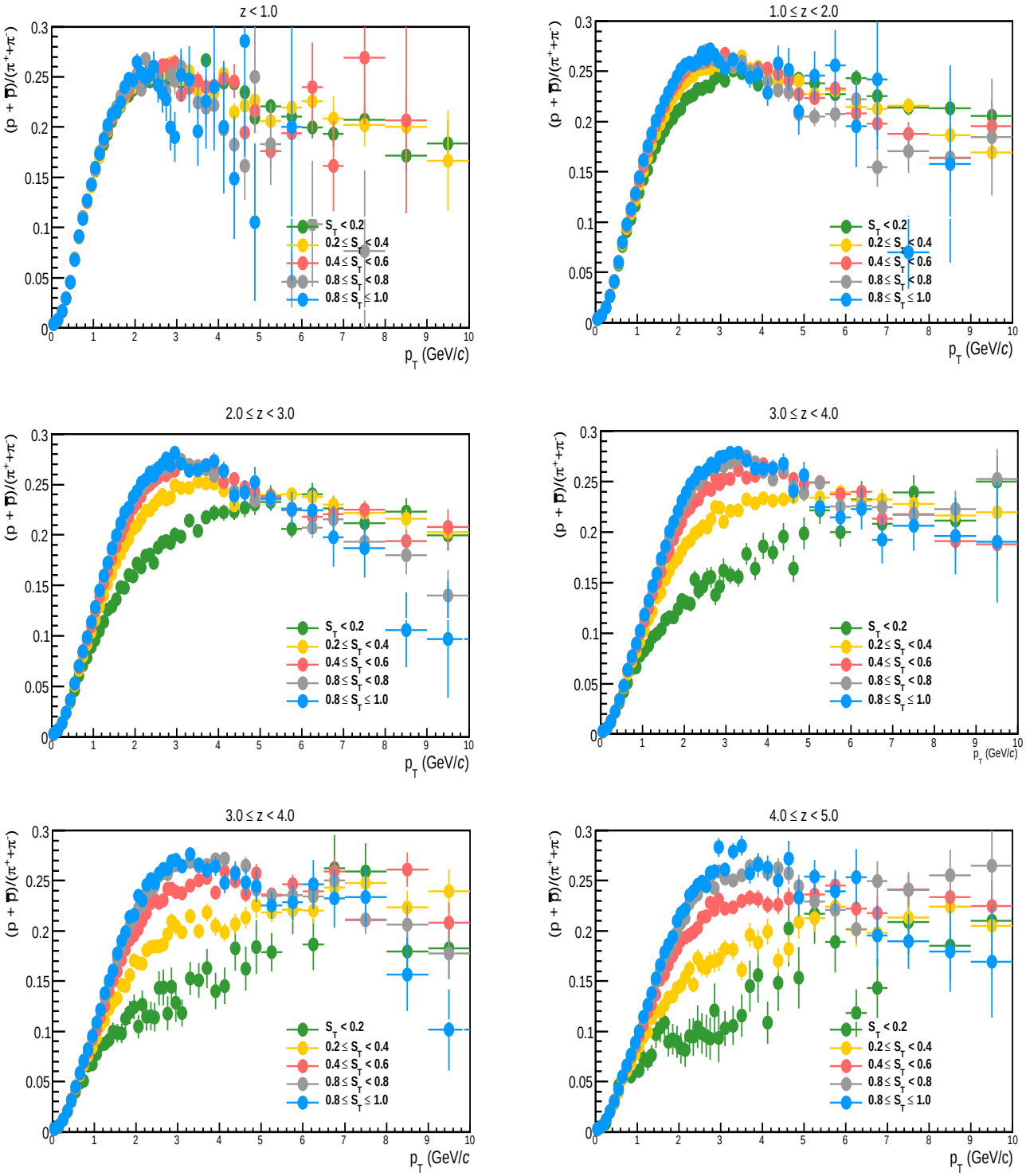

Fig. 6.12: p/π for pp collisions at $\sqrt{s}$ = 7.0 TeV as a function of S_{T} in different multiplicity bins. Obtained with PYTHIA 8.

7

Conclusions

The p_{T} spectra of π^+, π^-, K^+, K^-, p and $\bar{\mathrm{p}}$ at mid-rapidity $\mid y \mid < 0.5$ measured with TOF in pp collisions at 3 different energies: $\sqrt{s}$ = 0.9, 2.76 and 7.0 TeV was reported as the main result of this work. The particle identification method used for the TOF detector was discussed. All the steps to perform the analysis were described, the TOF unfolding procedure allows to obtain the pion and kaon spectra in the p_{T} range 0.5-2.5 GeV/*c* (0.5-2.0 GeV/*c*), and the proton spectra 0.8-4.0 GeV/*c* (0.8-2.4 GeV/*c*) for the 2.76 and 7 TeV (900 GeV) analysis.

The particle ratios p/π and K/π as a function of p_{T} seem to be energy independent within the systematic uncertainties. The ratios also provide very useful information at intermediate p_{T} values where an enhancement on the ratio p/π is present both in heavy ion and, in a lesser extent in pp collisions. This measurement provides constraints to Monte Carlo models, which fail to describe the data.

The comparison between TOF results obtained by the author are comparable with ALICE results. For the 2.76 TeV analysis, the spectra reported here are part of ALICE preliminary results. The 900 GeV analysis reported here represents an improvement over the ALICE published results, which have lower statistics.

I reported also the identified p_{T} spectra at $\sqrt{s}$ = 7.0 TeV as a function of transverse sphericity, showing important differences between the isotropic (high S_{T}) events and the jetty (low S_{T}) events, which are appreciated in the p/π ratio in the p_{T} range 0.5-2.5 GeV/*c*. However, one should bear in mind that the sphericity study presented here, has been limited to the use of MB corrections, and no corrections were applied for a possible selection bias in the sphericity bins. This is due to the complexity of the procedure for this correction in the data.

Moreover, I presented a similar analysis based on PYTHIA, which provides a better un-

derstanding of the mechanisms present in the hadron production and allows to extend the p_{T} range till 10 GeV/*c*. I showed that the hadron production is completely different for each type of events: isotropic (high sphericity) where the enhancement on the p/π ratio at ≈ 3.0 GeV is present; and *jetty* events (low sphericity) where the peak on the p/π ratio is not as pronounced.

One should always bear in mind that the MB pp collisions are a superposition of events with jets, isotropics and multi jets. Contrary to the usual strategy, I used the sphericity as a tool to separate the MB events in isotropic and jetty events, and showed that the hadron production changes for this two different types of events structures. The analysis based on PYTHIA shows that the enhancement present at 3 GeV/*c* in the p/π ratio is due to the isotropic or "bulk". Moreover, I observe that the color reconnection mechanism does not plays an important roll for the events with jets.

References

[1] Brueckner, Keith A. *Phys.Rev.* 86 (1952) 106-109.

[2] J. Beringer et al. (Particle Data Group), Phys. Rev. D86, 010001 (2012).

[3] ALICE Coll, *Eur. Phys. J. C* 72 (2012) 2183.

[4] A. Moraes, C. Buttar, I. Dawson. *Eur. Phys. J. C* 50, (2007), 435-466.

[5] R. Vogt. Ultrarelativistic Heavy-Ion Collisions. Elsevier, (2007).

[6] T. Sjöstrand, L. Lönnblad, S. Mrenna, P. Skands. PYTHIA 6.3 Physics and manual. arXiv:hep-ph/0308153.

[7] B. Anderson. The Lund Model. Cambridge monographs on particle physics, nuclear physics and cosmology. Cambridge University Press (2005).

[8] J. Letessier, J. Rafelski.Hadrons and quark gluon plasma. Cambridge University Press (2002).

[9] GEANT, Detector descriptions and simulation tool, CERN, Geneva 1993. http://wwwasd.web.cern.ch/wwwasd/geant/

[10] J. Ranft, The FLUKA and KASPRO hadronic cascade codes. *Computer Techniques in Radiation Transport and Dosimetry. Plenum Press* (1980)

[11] A. Fasso, et al. *Proc. Computing in High Energy and Nuclear Physics (La Jolla, CA)* http://www.slac.stanford.edu/econf/C0303241/proc/papers/MOMT005.PDF

[12] ALICE Coll, *Phys. Lett. B* 696 (2011) 30-39.

[13] ALICE Coll,Performance of the ALICE VZERO system. arXiv:1306.3130 [nucl-ex].

[14] ALICE Coll, *J. Phys.*, Vol. G32,(2006) 1620-1631.

[15] Performance of the ALICE Experiment at the CERN LHC, ALICE Internal, pre-draft.

[16] ALICE Coll,Technical Design Report of the Inner Tracking System, CERN LHCC, 1999-12.

[17] ALICE Coll, *Eur.Phys.J.C* 71(6): 1655, 2011.

[18] ALICE Coll, *Phys. Rev. C* 88, 044910 (2013)

[19] ALICE-HMPID collaboration. *Nuclear Physics B Proceedings Supplements*, vol 177 (2008)

[20] Root webpage, http://root.cern.ch/drupal/.

[21] Aliroot webpage, http://aliweb.cern.ch/Offline/AliRoot/Manual.html.

[22] Geant webpage, http://wwwasd.web.cern.ch/wwwasd/geant/.

[23] M.Chojnacki, Measurement of pions, kaons and protons with the ALICE detector in pp collisions at the LHC. PhD. thesis, (2012).

[24] A.P. Kalweit, Energy Loss Calibration of the ALICE Time Projection Chamber. Master thesis, (2008).

[25] Rick Field. *AIP Conf. Proc.* 928, pp. 91-98.

[26] F. Barile, M.Chojnacki,Y. Corrales Morales, B.Guerzoni, R.T. Jiménez Bustamante pi, K, p analysis in pp collisions at $\sqrt{s}$ = 2.76 TeV. ALICE Analysis Note. https://aliceinfo.cern.ch/Notes/node/185

[27] ALICE Coll, Production of charged pions, kaons and protons at large transverse momenta in pp and Pb-Pb collisions at $\sqrt{s_{NN}}$ = 2.76 TeV. *arxiv*: 1401.1250.

[28] R. Barlow and C. Beeston, *Comp. Phys. Comm.* 77 (1993) 219-228.

[29] J.Orear, Notes on Statisitics for Physicists, UCRL-8417. http://nedwww.ipac.caltech.edu/level5/Sept01/Orear/frames.html.

[30] R. Barlow, Systematic errors: facts and fictions, Manchester (2008).

[31] ALICE Coll, *Eur. Phys. J. C.* (2013) 73:2456.

[32] M. L. Miller *et. al*. Annu. Rev. Nucl. Part. Sci. 2007. 57:205?43.

[33] S.Sapeta, U.A. Wiedemann, Jet hadrochemistry as a characteristics of jet quenching. *arXiv*:0707.3494

[34] ALICE Coll, *Eur. Phys. J. C*(2011) 71:1655.

[35] ATLAS Coll, *Phys. Rev. D* 88, 032004 (2013).

[36] CMS Coll, emphPhysics Letters B 699 (2011) 48?67.

[37] A.Banfi et al. *J. High Energy Phys*. 08062 (2004).

[38] P. Beccatini et al. Multi-Parton Interactions at the LHC, arXiv:1111.0469v2.

[39] A.Ortiz Velazquez. P. Christiansen, E.Cuautle Flores, I.A. Maldonado Cervantes, G. Paic. *Phys. Rev. Lett.* 111, 042001 (2013).

[40] ALICE Coll, *Phys.Lett. B712* (2012) 165-175.

List of Figures

Index of tables